5-2016

Design and Optimization of Membrane-Type Acoustic Metamaterials

Matthew G. Blevins
University of Nebraska-Lincoln, mattblvns@gmail.com

DESIGN AND OPTIMIZATION OF MEMBRANE-TYPE ACOUSTIC METAMATERIALS

by

Matthew Grant Blevins

A DISSERTATION

Presented to the Faculty of

The Graduate College at the University of Nebraska

In Partial Fulfillment of Requirements

For the Degree of Doctor of Philosophy

Major: Architectural Engineering

Under the Supervision of Professor Lily M. Wang

Lincoln, Nebraska

May, 2016

DESIGN AND OPTIMIZATION OF MEMBRANE-TYPE ACOUSTIC METAMATERIALS

Matthew Grant Blevins, Ph.D.

University of Nebraska, 2016

Advisor: Lily M. Wang

One of the most common problems in noise control is the attenuation of low frequency noise. Typical solutions require barriers with high density and/or thickness. Membrane-type acoustic metamaterials are a novel type of engineered material capable of high low-frequency transmission loss despite their small thickness and light weight. These materials are ideally suited to applications with strict size and weight limitations such as aircraft, automobiles, and buildings. The transmission loss profile can be manipulated by changing the micro-level substructure, stacking multiple unit cells, or by creating multi-celled arrays. To date, analysis has focused primarily on experimental studies in plane-wave tubes and numerical modeling using finite element methods. These methods are inefficient when used for applications that require iterative changes to the

structure of the material. To facilitate design and optimization of membrane-type acoustic metamaterials, computationally efficient dynamic models based on the impedance-mobility approach are proposed. Models of a single unit cell in a waveguide and in a baffle, a double layer of unit cells in a waveguide, and an array of unit cells in a baffle are studied. The accuracy of the models and the validity of assumptions used are verified using a finite element method. The remarkable computational efficiency of the impedance-mobility models compared to finite element methods enables implementation in design tools based on a graphical user interface and in optimization schemes. Genetic algorithms are used to optimize the unit cell design for a variety of noise reduction goals, including maximizing transmission loss for broadband, narrow-band, and tonal noise sources. The tools for design and optimization created in this work will enable rapid implementation of membrane-type acoustic metamaterials to solve real-world noise control problems.

Acknowledgments

I would like to acknowledge several people without whom this research would not be possible. First, I would like to thank Dr. Siu-Kit Lau for his idea of applying the impedance-mobility approach to membrane-type acoustic metamaterials which formed the basis of this research. His kindness as a person and diligence as a researcher have greatly influenced my approach to learning. I would also like to thank Dr. Lily Wang for advising me throughout my graduate career. Her encouragement and support have been tremendously important to me. I would like to thank Dr. Christos Argyropoulos and Dr. Christina Naify for their assistance with finite element modeling. Thanks to Dr. Douglas Keefe and Caleb Sieck for their conversations and pointed questions about my research. I would like to thank the remaining members of my supervisory committee: Dr. Mahboub Baccouch, Dr. Yaoqing Yang, and Dr. Erica Ryherd for their support and valuable feedback. I would like to thank members of the Nebraska Acoustics Group for their friendship and support throughout my career at UNL. Special thanks go to Christopher Ainley, Andrew Hathaway, Ellen Peng, Hyun Hong, Joonhee Lee, and Laura Brill. Lastly, I would like to thank my family; my parents, William and Jane Blevins, my brother, William, and his wife, Sara, for their love, support, and encouragement.

Table of Contents

List of Figures

List of Tables

Chapter 1

Introduction and Literature Review

Membrane-type acoustic metamaterials present a novel solution to one of the most difficult problems in acoustical engineering: controlling low-frequency noise. The benefits of small thickness and light weight make these new materials very desirable for use in buildings and transit vehicles. Previous investigation has shown that these materials are capable of remarkable transmission loss, far above the mass law, at low frequencies. Even though these materials show much promise, little attention has been given to design and optimization for application to noise control problems. Additionally, all possible configurations of these materials have not been fully explored. Analysis has not been extended to higher frequencies or non normally-incident excitation. Only rectangular and circular frames have been considered. Also, absorption due to membrane damping has been neglected. The research presented in this dissertation seeks to bridge those gaps by creating efficient numerical models and tools for design and optimization of membrane-type metamaterial assemblies.

This chapter begins with an in-depth look at the motivating factors for designing new materials to control low-frequency noise. Current methods of passive and active low-frequency noise control are discussed, noting their shortcomings. The research objectives of the project to address the problem are enumerated. Previous works on acoustic metamaterials, the proposed modeling method, and the proposed optimization scheme are reviewed. The chapter ends with a description of the structure of the rest of this dissertation.

1.1 Motivation

Control of airborne noise into buildings, aircraft, and automobiles is conventionally accomplished through techniques combining insulation and absorption of incident sound waves. Controlling low frequency noise is especially challenging because of long wavelengths, necessitating massive barriers or thick layers of absorptive material. Traffic noise from highways near residential areas is typically controlled by erecting heavy masonry walls with surface densities often greater than 20 kg/m^2 [Bies & Hansen 2009]. Noise control treatment in aircraft often consists of one or more layers of porous material such as fiberglass with density approximately 10 kg/m^3 covered with heavy limp material and impervious trim [Wilby 1996]. For a planar, nonporous, homogeneous, flexible partition with thickness much less than a wavelength of incident sound, the sound transmission loss is given by the mass law

[Kinsler et al. 2000]. For normally incident sound, the mass law is given by

$$TL_m = 10 \log_{10} \left[1 + \left(\frac{\omega \rho_s}{2 \rho_0 c_0} \right)^2 \right], \tag{1.1}$$

where ω is the angular frequency in rad/s, ρ_s is the surface density of the panel in kg/m^2, ρ_0 is the density of air in kg/m^3, and c_0 is the speed of sound in air in m/s. This equation gives the practical limitation that increasing the transmission loss of a panel at a particular frequency by 6 dB requires a doubling of surface density.

Absorption of sound by porous materials such as fiberglass and foams is also commonly employed in conjunction with insulative treatments. Absorption is most effective when it encompasses at least one-quarter of a wavelength of the lowest frequency of interest from a reflective surface. This ensures that at some point in the absorptive material the particle velocity is a maximum, increasing the effectiveness of converting vibration to heat via friction [Everest 2001]. Frequencies less than 500 Hz require absorptive treatments with a total thickness of at least six inches ($\sim$ 15 cm) for maximum effectiveness, which is impractical in many situations.

Current passive noise control strategies in buildings implement layers of conventional insulating or absorbing materials such as drywall, masonry, mass-loaded vinyl, and fiberglass. Size and weight restrictions, however, limit the effectiveness of these materials at low frequencies. To be effective at low frequencies, double panels must have a mass-air-mass resonance frequency well below that of incident sound, requiring a large separation [Long 2006]. These solutions may be feasible to control noise in buildings or outdoors, but are ill-suited to applications

where low weight and small size are critical.

Helicopters and other propeller or rotor driven aircraft are capable of producing high sound pressure levels ($>$ 100 dB re 20 μPa) at low frequencies ($<$ 500 Hz) corresponding to the rotor blade passage frequency and its harmonics and the gearbox rotation frequencies [James 2005]. In the aerospace and automotive industries, however, added weight and thickness of wall panels decrease fuel efficiency and usable cabin volume thereby increasing costs to manufacturers and consumers alike.

Wind turbines can produce significant low frequency and infrasonic noise at building façades, which becomes a limiting factor for placement of wind farms [Møller & Pedersen 2011]. Inside buildings, heating ventilation and air-conditioning (HVAC) equipment is a major source of noise and complaints from occupants [ASHRAE 2011; Ryherd & Wang 2008]. In each of the above scenarios, current passive noise control techniques are ineffective.

Active control is another popular technique to reduce low frequency tonal noise in aircraft and buildings. This technique uses one or more secondary acoustic and/or structural vibration sources to produce sound waves that combine destructively with those of the primary noise source, resulting in cancellation of the noise. The output of the secondary source(s) is actively controlled via one or more error sensors and signal processing to minimize an acoustic quantity, typically squared pressure, energy density, or acoustic potential energy, at the sensor [Lau & Tang 2001]. Active control works well in rooms where the sound field is dominated by modes. Since the locations of nodes and anti-nodes in rooms are predictable, the

error sensors can be efficiently placed to produce good results. Active control can also be useful for communication in high background noise environments by incorporating secondary sources and sensors into headsets, such as those worn by pilots and crew members in aircraft [Elliott 1999; Shaw & Thiessen 1962].

Active control, however, has several practical limitations in implementation. The sound field can be reduced dramatically by active noise control near the sensor locations, but elsewhere the noise can actually be increased. The global effectiveness of active reduction of noise increases with the number of error sensors and control sources [Elliott & Nelson 1993]. However, increasing the number of error sensors and control sources increases the amount of necessary infrastructure such as electromechanical transducers, support framework, and wiring, thereby increasing the weight and potential for electrical problems. Active control in headsets may work well when the number of passengers is small, such as in helicopters, but becomes limiting when many headsets are required, along with supporting infrastructure.

In addition to being difficult to control through conventional techniques, low frequency tonal noise in aircraft is also perceived as more annoying than noise due to only boundary layer excitation [Leatherwood 1987]. More & Davies [2010] showed that tonalness of aircraft flyover noise was correlated with annoyance ratings, meaning that stimuli with more prominent low frequency tones were considered more annoying. More generally, Ryherd & Wang [2008] showed that increasing tonal prominence increases the perception of tonality, loudness, annoyance, and distraction, for tones of 120Hz, 235Hz, and 595Hz in a simulated office environment.

Leventhall [2004] reviewed studies on low frequency noise, and pointed out that annoyance of low frequencies increases rapidly with level. He also noted the difficulty of adequately quantifying the annoyance due to low frequency noise and tones.

Control of low frequency noise presents many physical and practical challenges. With traditional passive control methods, the physical necessity of large thicknesses and high mass densities limits the effectiveness at low frequencies where size and weight are critical design parameters. With active control the increased effectiveness at low frequencies is counteracted by the added equipment with several moving parts and power requirements. A method of low frequency control that combines the simplicity of passive materials and the effectiveness of active control is needed. Moreover, a method of designing such materials and optimizing them for rapid application in noise control problems is critical.

1.2 Research Objectives

The objective of the research presented in this dissertation is to formulate computationally efficient dynamic models of a novel type of engineered materials called membrane-type acoustic metamaterials and demonstrate their viability for use in design and optimization of noise-mitigating structures via genetic algorithms. An impedance-mobility technique is used to model the response of membrane-type acoustic metamaterials. The model is validated numerically using finite element models. A genetic algorithm is used to find optimal configurations to meet specific design criteria such as maximum broadband TL, specified frequency of peak TL,

and maximum bandwidth in the stop-band. The objective can be broken into three tasks:

1. Develop impedance-mobility models of membrane-type acoustic metamaterials
   (a) for a single unit cell,
   (b) for an array of cells,
   (c) for layers of unit cells.
2. Implement genetic algorithms to optimize membrane-type acoustic metamaterial structures for noise control applications.
3. Validate the designs numerically using finite element models.

The goal of this research is to introduce novel computational tools for rapid development and implementation of membrane-type acoustic metamaterials to solve engineering noise control problems. These tools, in the hands of competent noise control engineers, will enable the application of thin light-weight low-frequency noise control solutions to real-world problems.

1.3 Background

This section describes the concept of metamaterials from its origin in optics and electromagnetism to applications in acoustics. Impedance-mobility modeling is then introduced beginning with its foundation in circuit analysis and mechanical vibration to its use in modeling structural-acoustic coupled systems. The basic

premise of impedance-mobility modeling is described, and its advantages over other commonly used methods are discussed. Modeshape functions for plates and membranes carrying one or more added masses are examined. Optimization schemes are reviewed with special focus on genetic algorithms and their implementation in engineering problem solving.

1.3.1 Metamaterials

Metamaterials are novel engineered materials in optics, electromagnetism, and acoustics that derive their macro-level properties from their micro-level structure. These materials often exhibit unique properties that are counter-intuitive. Examples include lenses that refract light in the "wrong" direction, lenses that produce images at distances smaller than a wavelength [Pendry 2000], materials that allow sound to propagate in only one direction [Li et al. 2011], and, the case studied in this dissertation, materials that block low frequency sound despite small mass and thickness [Yang et al. 2008]. Potential applications of metamaterials in optics and electromagnetism include artificial magnetism for use in magnetic resonance imaging (MRI) [Freire et al. 2010; Smith et al. 2004], antennas for cellular telephones and communications devices [Das 2009; Wang et al. 2007], and optical focusing up to one-sixth of a wavelength [Fang et al. 2005]. In acoustics, metamaterials can be applied to noise control [e.g. Naify et al. 2010; Yang et al. 2010; Ho et al. 2003], sonic and ultrasonic focusing [Climente et al. 2010; Guenneau et al. 2007; Fang et al. 2006], acoustic cloaking [Cheng et al. 2008; Pendry & Li 2008; Chen & Chan

2007], and many more areas [Craster & Guenneau 2012].

The concept of metamaterials was first introduced in the field of optics when Veselago [1968] proposed materials with negative electric permittivity and magnetic permeability to manipulate electromagnetic waves. For a monochromatic wave in an isotropic substance, the dispersion relation and square of the index of refraction are given by

$$k^2 = \frac{\omega^2}{c^2} n^2, \tag{1.2}$$

$$n^2 = \epsilon\mu, \tag{1.3}$$

where ω is the frequency, c is the speed of light, ϵ is the electric permittivity and μ is the magnetic permeability. It can be seen from Equations (1.2) and (1.3) that a simultaneous change of sign for ϵ and μ will not affect the dispersion relation, and therefore the wave will propagate. The changes of sign, however, give rise to many other unusual characteristics that can be exploited in scientific applications.

Pendry et al. [1996] investigated the concept of a negative electric permittivity by considering an *effective* medium in which a periodic cellular structure can be thought to behave as a homogeneous medium in the long-wavelength limit. This is a key concept that arises often in the study of both electromagnetic and acoustic metamaterials. Pendry [2000] later applied Veselago's proposal to the realization of a "superlens" capable of focusing light onto an area smaller than a square wavelength using a silver lens with parallel sides. This could potentially enable perfect imaging at optical and microwave frequencies.

1.3.1.1 Acoustic Metamaterials

As the volume of work related to electromagnetic metamaterials increased, researchers became interested in applying the theoretical understanding to acoustic waves. Li & Chan [2004] investigated a theoretical acoustic analogue to Veselago's double-negative electromagnetic metamaterial that demonstrates both negative effective bulk modulus and density in a narrow frequency band. The analogue is made possible by considering the acoustic refractive index given by

$$n^2 = \frac{\rho}{\kappa}, \tag{1.4}$$

where ρ is the mass density and κ is the bulk modulus, and comparing it to Equation (1.3). It is evident that a simultaneous change of sign of both mass density and bulk modulus ensures wave propagation. Since negative density and bulk modulus do not appear in nature, Chan et al. [2006] suggested materials with locally resonant building blocks to achieve these properties in certain frequency bands, such as Li & Chan's material which consisted of soft rubber spheres suspended in water. More generally, they showed that negative density and bulk modulus are possible in a one-dimensional structure consisting of springs separating masses with internal resonating structures. A schematic of this type of structure is shown in Figure 1.1. A negative density may seem counterintuitive, but it is important to note that in acoustics density is a dynamic quantity; i.e. it changes over time. Sheng et al. [2007] provided a rigorous derivation of dynamic mass density and showed that it is not necessarily equivalent to volume averaged mass density in the long wavelength limit.

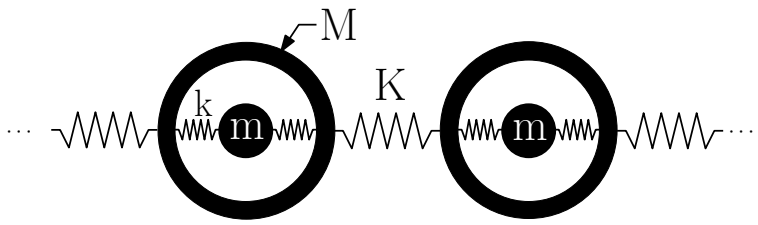

Figure 1.1: Schematic of 1-D metamaterial

The dynamic density of a medium needed for calculating wave speed, for instance, can be quite different from the volume-averaged density. Moreover, they showed that near resonance the dynamic mass density can become negative. A medium with negative bulk modulus and mass density expands upon compression and moves to the left when being pushed to the right. This is apparent in the Poynting vector for a propagating plane wave given by

$$\mathbf{S} = \frac{|p|^2 \mathbf{k}}{2\omega\rho}. \tag{1.5}$$

When the mass density, ρ, is negative, the energy flux $\mathbf{S}$ and the wave vector $\mathbf{k}$ point in opposite directions [Chan et al. 2006]. Li & Chan [2004] showed that double negativity results when the volumetric dilation of a sphere is out of phase with the pressure field, and the motion of the center of mass of the sphere is out of phase with incident directional pressure field.

Among the first to experimentally realize acoustic metamaterials were Liu et al. [2000]. They fabricated what they called "sonic crystals" based on a cellular structure of hard high-density spheres coated with elastically soft material suspended in a rigid epoxy matrix. The structure demonstrated a near-total reflection of incident energy in a narrow frequency band. Wester et al. [2009]

constructed a similar material and compared its experimental transmission loss performance to a 1-D mass-spring-damper model, showing good agreement. Many authors have gone on to study the various acoustic properties based on the same cellular structure [e.g Ding & Zhao 2011; Zhao et al. 2007; Li et al. 2006]. A cross-section of one layer of this metamaterial is shown in Figure 1.2. Multiple layers and different packing structures are, of course, possible.

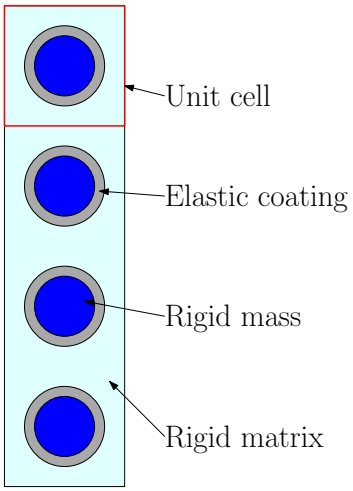

Figure 1.2: Cross-section of "Sonic Crystal" locally resonant acoustic metamaterial

Zhao et al. [2006] considered not only the transmission of sound through acoustic metamaterials, but also the absorption of sound by viscous damping. Using the multiple scattering approach, they found that increasing the viscosity of the elastic coating decreases the sound transmission loss at the peak due to the decrease in the resonant amplitude. The authors also noted that as viscosity increases, absorption becomes the dominant mode of transmission loss.

A defining feature of acoustic metamaterials, which is evident in Figures 1.1 and 1.2, is the periodic arrangement of sub-wavelength elements. Although not

strictly necessary for negative bulk modulus and/or mass density [Sheng et al. 2007; Chan et al. 2006], periodicity makes conditions favorable for homogenization theory to be applied to obtain *effective* quantities (e.g. bulk modulus and mass density) that can be used in treating an array of elements as a single contiguous structure. These effective quantities can be positive, as in the case of conventional materials, or negative within a certain frequency range, as with acoustic metamaterials.

1.3.1.2 Membrane-Type Acoustic Metamaterials

Membrane-type acoustic metamaterials arose as a two-dimensional counterpart to sonic crystals, with a unit cell consisting of a thin elastic membrane carrying an attached mass weakly tensioned over a rigid grid. The unit cells are typically rectangular or circular in shape; see Figures 1.3 and 1.4. These types of metamaterials, also a class of locally resonant sonic (or acoustic) materials, were first explored in detail theoretically and experimentally by Yang et al. [2008]. They found that in a frequency range between two modal resonances, the dynamic mass of the unit cell becomes negative. This is physically explained by an out-of-phase relationship between the incident sound and the vibration of the membrane resulting in zero surface-averaged displacement and near-total reflection, creating a transmission loss peak. In a separate study, Yang et al. [2010] demonstrated that by using multiple masses per unit cell and stacking multiple panels with different effective frequency ranges, broadband attenuation greater than 40 dB can be achieved.

Naify et al. [2010] investigated a circular unit cell of a membrane-type acoustic

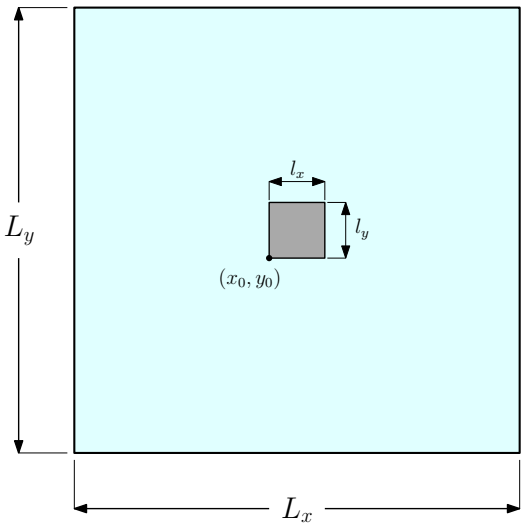

Figure 1.3: Schematic of rectangular unit cell

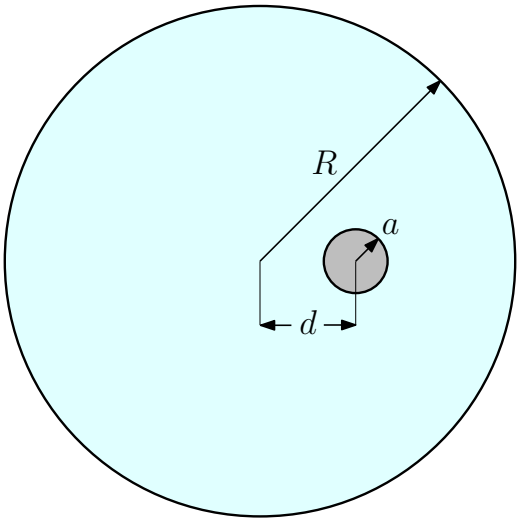

Figure 1.4: Schematic of circular unit cell

metamaterial experimentally as well as numerically using a finite element method (FEM). It was shown that increasing the mass of the attached mass increases the magnitude of the TL peak while decreasing its frequency. Increasing the mass decreases the first resonance frequency while negligibly affecting the second resonance frequency. Increasing the tension on the membrane increases the magnitude of the first resonance, the peak TL frequency, and the second resonance. It was noted that the effect of increasing mass is similar to that of a simple harmonic oscillator for the first resonance frequency, indicating that the resonance of the first mode is dominated by the membrane tension rather than the membrane stiffness. By measuring the membrane displacement, the authors also showed directly that the TL peak occurs at a frequency between the first two resonances where the superposition of the modeshapes creates nearly zero volume displacement. At this frequency the membrane behaves as a rigid wall, resulting in nearly total sound reflection.

Naify et al. [2011b] investigated the scale-up of membrane-type acoustic metamaterials by arranging multiple unit cells into an array using finite element analysis and transmission loss measurements in a plane-wave tube. They showed that varying the mass distribution among the unit cells results in multiple mass-dominated resonances and TL peaks. The second resonance frequency is unaffected by the change in mass because the membrane resonance occurs when the mass is nearly motionless. An increase in resonance frequencies and TL peak frequency also occurs due to pressure coupling between adjacent cells causing a higher effective stiffness experienced by the incident wave. A decrease in the TL peak bandwidth is observed with decreasing frame compliance, which is a potential limiting factor for scale-up to multi-celled arrays.

Naify et al. [2012] then applied their work to scaling of multiple layers of membrane-type acoustic metamaterials. Transmission loss of two identical unit cells stacked in series was measured in a plane-wave tube and modeled numerically using FEM. It was shown that the TL increases by $\sim 10dB$ across a broad range of frequencies, and even higher at the TL peak, with the addition of a second layer. Unit cells carrying different masses were also tested, and shown to exhibit a similar increase in overall TL while also introducing an additional TL peak corresponding to the second unit cell. A third resonance is also introduced corresponding to the spacing between the two cells. A configuration of two stacked four-cell arrays was also tested, and shown to exhibit many of the same properties and trends as its single-celled counterparts. The number of TL peaks corresponds to the number of different mass/cell combinations, with frequencies dependent on the mass

magnitude. The authors found negligible effect of stacking order or distance between panels on TL performance below the membrane resonance. This agrees with the observation by Yang et al. [2008] that the evanescent waves exhibit a very short decay length, meaning that the incident wave has little effect on the far field at the TL peak frequency. The stacked metamaterials then behave independently and the added effect of the double panel structure is noted. The effect of the mass size was also investigated using a single cell. It was shown that increasing the mass radius, thereby decreasing the effective membrane radius, increases the membrane resonance frequencies while having little impact on the TL peak magnitude.

Zhang et al. [2012] used a modal superposition method to calculate the transmission loss of a square membrane carrying a square mass. The modal superposition method employed is an analytical method with accuracy only limited by the number of modes that are considered in the calculation. Their results agree with the results of the finite element method employed by Naify et al. [2011b]. They also analyzed the effect of mass magnitude, membrane density, and tension. Their results agreed with previous research, showing that varying the mass only affected the first resonance, varying the membrane density only affected the second resonance, and varying the tension shifted the frequencies of the TL peak and all resonances. The location of the mass was also studied by varying the mass along one axis and a diagonal. They showed that the first resonance decreases in frequency and the TL peak frequency decreases and then increases as the mass moves away from the center of the cell.

Chen et al. [2014a] used an analytical coupled vibroacoustic model to examine

the effects of micro-structure properties on the acoustic performance of membrane-type acoustic metamaterials. Their model used a circular unit cell, and represented one or more rigid finite masses with point forces at collocation points along the interface between the membrane and mass with an inner continuity condition at each point. This method allows the rigid-body motion and rotational inertia of the mass to be taken into account. The results obtained with the analytical method agree well with those from a FEM model. Their results for a mass located at the center of the membrane agree with the previous results [Zhang et al. 2012; Naify et al. 2011b]. For an eccentric mass, it was found that a third resonance is introduced corresponding to the rotational effects of the finite mass. Likewise, a second transmission dip is found between the second and third resonances. They found that as eccentricity increases, the first and second TL peak frequencies increase, while the third peak decreases. The authors also investigated the effect of two semicircular masses on the unit cell's acoustic performance. They found that the first mode corresponds to in-phase translational and rotational motion of the masses. The second mode is mainly caused by rotational motion of the masses. The third mode is due to strong motion of the membrane between the two masses. This arrangement results in three resonance peaks in the transmission curve. The first and second resonance peaks increase with increasing distance between attached masses, while the third peak decreases as the distance increases.

Attempts have been made at broadening the TL peak by varying the micro-structure parameters of the unit cell. Naify et al. [2011a] experimentally and numerically studied the effects of using coaxial ring masses as opposed to a single

central mass. They found that, depending on the configuration, coaxial ring masses result in broadening of the TL peak or the introduction of multiple TL peaks. Zhang et al. [2013] investigated the performance of membrane-type metamaterials with different masses in adjacent unit cells, similar to work by Naify et al. [2012]. They found the same broadening of the TL peak and introduction of multiple peaks and resonances.

The research discussed above describes the effects of adjusting micro-structure parameters of unit cells and larger assemblies of membrane-type metamaterials on transmission loss. Little attention, however, is given to determining optimal parameters for desired performance. In order to fully utilize these recent advances in low frequency noise control, efficient computational models for design and optimization are necessary.

1.3.2 Impedance-Mobility Modeling

Impedance-mobility modeling is an analytical approach often used to describe electro-mechanical or mechanical-acoustic coupled systems. It has roots in analysis of electrical circuits such as those in early communication devices like the telegraph and telephone and was later adapted for use in vibrating mechanical and acoustical systems [Gardonio & Brennan 2002]. The analysis of purely structural or purely acoustical systems is carried out by writing the analogous electrical circuit, solving the electrical problem using electric network theory, and reworking the problem into structural or acoustical terms [Fahy & Walker 2004]. Kim & Brennan [1999]

extended the classical theory of structural-acoustic interaction developed by Dowell et al. [1977] to analyze general structural-acoustic coupled systems in modal coordinates using the uncoupled forms of structural mobility and acoustic impedance. This extension allows the formulation of structural-acoustic problems in a compact matrix form that is easily solved using a computer. Formulation in terms of uncoupled impedance and mobility also allows the system to be subdivided into structural and acoustic domains. In turn, changes to one domain do not necessitate changes to the mathematical formulation of the other domains in the system. The method also does not have high-frequency limitations that are often encountered with finite element methods since it is not necessary to spatially discretize the system.

The impedance-mobility approach is, essentially, a modal superposition method in which the interaction between uncoupled modes of the structural and acoustic domains is represented by coupled acoustic impedance and structural mobility. The uncoupled acoustic impedance and mobility are written

$$Z_A = \frac{p}{Q}, \qquad Y_A = \frac{Q}{p}, \tag{1.6, 1.7}$$

where p and Q are the acoustic pressure and source strength, respectively. Likewise, the structural mobility and impedance can be written

$$Y_S = \frac{u}{F}, \qquad Z_S = \frac{F}{u}, \tag{1.8, 1.9}$$

where u and F are the resulting velocity and applied force, respectively. An analysis of the dimensions of Equations (1.6)-(1.9) reveals a mismatch, with the units of Z_S being $[Ns/m]$ and those of Z_A being $[Ns/m^5]$. This suggests a need for a coupling factor to analyze structural-acoustic coupled systems. Kim & Brennan [1999] introduced the terms of coupled acoustic impedance and coupled structural mobility,

$$Z_{CA} = \frac{F_A}{u}, \qquad Y_{CS} = -\frac{Q_S}{p}, \tag{1.10, 1.11}$$

where the new terms F_A and Q_S are the acoustic reaction force, and the structural source strength, respectively.

In the general modal superposition scheme, the field variables (displacement, pressure, velocity, etc.) are written as the summation of the products of mode shape functions and modal amplitudes. For the cases of pressure and velocity, the equations are

$$p(\mathbf{x}, \omega) = \sum_{n=1}^{N} \psi_n(\mathbf{x}) a_n(\omega) = \mathbf{\Psi^T a}, \tag{1.12}$$

and

$$u(\mathbf{y}, \omega) = \sum_{m=1}^{M} \phi_m(\mathbf{y}) b_m(\omega) = \mathbf{\Psi^T b}, \tag{1.13}$$

respectively, where $\mathbf{x}$ and $\mathbf{y}$ are the acoustic and structural coordinates, ω is frequency, ψ_n and ϕ_m are acoustic and structural mode shape functions, and a_n and b_m are the modal amplitudes. In matrix form $\mathbf{\Psi}$ and $\mathbf{a}$ are the N length arrays of uncoupled acoustic modeshapes and modal acoustic pressure amplitudes. $\mathbf{\Phi}$ and $\mathbf{b}$ are the M length arrays of uncoupled structural mode shapes and modal structural

vibration amplitudes.

Using the impedance-mobility approach, the modal amplitude vectors can be written in terms of the uncoupled and coupled acoustical impedance and structural mobility matrices. For the example of a rigid-walled cavity with one flexible surface impinged upon by an external mechanical force and internal acoustic source studied by Kim & Brennan [1999], the equations for modal pressure amplitude and structural vibration amplitude can be written

$$\mathbf{a} = (\mathbf{I} + \mathbf{Z_a Y_{cs}})^{-1} \mathbf{Z_a} (\mathbf{q} + \mathbf{C Y_s g}), \tag{1.14}$$

and

$$\mathbf{b} = (\mathbf{I} + \mathbf{Y_s Z_{ca}})^{-1} \mathbf{Y_s} (\mathbf{g} - \mathbf{C Z_a q}), \tag{1.15}$$

where $\mathbf{I}$ is the identity matrix, $\mathbf{q}$ and $\mathbf{g}$ are the modal acoustic source strength and vibration amplitude vectors, respectively. $\mathbf{C}$ is the $(N \times M)$ structural-acoustic modeshape coupling matrix defined by

$$C_{m,n} = \int_{S_f} \psi_n(\mathbf{y}) \phi_m(\mathbf{y}) dS, \tag{1.16}$$

where S_f is the surface of the vibrating structure.

Kim & Brennan [1999] refined the matrix formulation of the impedance-mobility approach described above and applied it to the analysis of the response of a rigid-walled cavity with a flexible panel under acoustic and structural excitation. The acoustic pressure at a point inside the cavity and the structural

vibration velocity on the flexible panel were predicted, and showed good agreement with experimental results. Lau & Tang [2001] used the impedance-mobility approach to study the active control of a sound field in a rectangular enclosure. They highlighted the flexibility of the impedance-mobility approach to analyze structural-acoustic coupled systems.

Ouisse et al. [2005] developed a method based on impedance and mobility concepts called the patch transfer function (PTF) approach which discretizes the coupling surface between sub-domains into elementary surfaces, rather than nodes which are commonly used in finite element methods. This method has been used to study transmission loss of double panels [Chazot & Guyader 2007], the structural and acoustic velocities of micro-perforated panels [Maxit et al. 2012], positioning of absorbing material [Totaro & Guyader 2012], and more.

The research in this dissertation implements the impedance-mobility approach to study membrane-type acoustic metamaterials due to its inherent computational efficiency and flexibility. Optimization requires many iterations to converge on a solution, and inefficient modeling methods become prohibitively time-consuming. The flexibility of the impedance-mobility approach also allows the analysis to be extended to include other structural or acoustic systems.

1.3.3 Genetic Algorithms

Optimization is the process of iteratively improving upon a solution to a given problem by using information gained from previous trials until the most suitable

solution is found, subject to pre-defined criteria. There are many types of algorithms for optimization, each with its own inherent advantages and disadvantages. Evolutionary algorithms (EAs) have become popular in recent decades due to their ability to converge on globally optimal solutions as opposed to converging on locally optimal solutions or failing to converge entirely, which are common problems with mathematical optimization. EAs are also convenient when dealing with problems with many variables and non-linear objective functions [Elbeltagi et al. 2005]. In addition EAs usually do not require derivatives, unlike gradient-based methods, and therefore can be applied to non-differentiable functions.

Several types of EAs exist today that draw influence from the natural world. Genetic algorithms (GAs) are based on the process of Darwinian evolution through natural selection, crossover, and mutation [Holland 1975]. Memetic algorithms (MAs) are similar to GAs and incorporate the ability for individuals, or "memes", to gain experience or learn [Merz & Freisleben 1997]. Particle swarm optimization (PSO) is inspired by the social behavior of migrating birds in which each bird tries to find the best position in the flock [Kennedy 1997]. Ant colony optimization (ACO) draws from the social behavior of ants finding the shortest distance between a food source and their nest by tracking pheromone trails [Dorigo et al. 1996].

Due to their inherent ability to handle large numbers of input parameters of various types, GAs are chosen to optimize unit cells of membrane-type acoustic metamaterials. GAs are also well-known for converging on globally optimal solutions, so they are well-suited to design applications.

Genetic algorithms are numerical optimization methods inspired by the

processes of biological evolution and natural selection, in which the most fit individuals survive to pass on their genetic information to the next generation [Haupt 1995]. Figure 1.5 shows the framework of a basic GA.

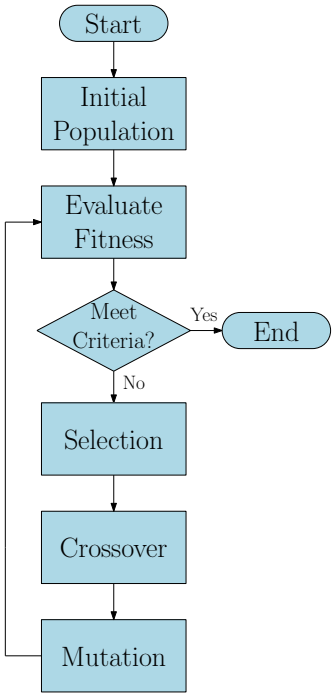

Figure 1.5: Flowchart of a basic genetic algorithm

The first step in the procedure is to randomly generate an initial, or "parent", population of chromosomes. Chromosomes are broken down into individual genes, which are represented by a sequence of binary bits. Genes represent a particular attribute, while chromosomes completely describe the object being optimized. For example, a gene for a unit cell membrane-type acoustic metamaterial might represent the mass location, membrane tension, or membrane shape, etc. The chromosome is the set of all of the genes necessary to uniquely describe the unit cell.

Since the GA operates on binary strings, a method is needed to decode the strings into values that represent the physical nature of the object. A binary string

of B bits can be converted to an integer via

$$Int = \sum_{i=1}^{B} Bin(B - i + 1) \cdot 2^{i-1}, \tag{1.17}$$

where Bin is the binary string and its argument is the bit location ranging from 1 to B. Once an integer value, Int, is obtained, the result can be scaled to fit the range of values that the parameter, x, can take by specifying a minimum and maximum value, x_{min} and x_{max} respectively, and applying the equation

$$x = x_{min} + \frac{x_{max} - x_{min}}{2^B - 1} Int. \tag{1.18}$$

The next step of the GA is to evaluate the fitness, sometimes termed "cost", of each parent. To do this a fitness or cost function that represents the goals of the optimization procedure is necessary. For example, a fitness function that optimizes broadband transmission loss might be written

$$F_i = \int_{\omega_{min}}^{\omega_{max}} TL(\omega) d\omega \tag{1.19}$$

where F_i is the fitness score from the i^{th} parent where $i = 1 \ldots N$, and ω_{min} and ω_{max} are the lower and upper bounds of the frequency range of interest. Another fitness function that optimizes TL at 500 Hz, for example, might be written

$$F_i = TL(500Hz). \tag{1.20}$$

It is important to note that as the fitness increases, so does the value of the fitness function.

Each parent is then sorted according to its fitness score. At this point if the population meets a specified stopping criterion, the GA is finished and the most fit parent is the optimal solution. Typically, though, the process is not stopped until convergence is reached, where the fitness scores for each parent in the population are very close or identical.

If the stopping criterion is not met, the parents undergo the process of selection, wherein the most fit survive to pass on their genetic information. This step allows for some creativity on the part of the programmer in deciding which parents survive. A typical scheme is to keep the most fit half of the parent population. In this scheme each set of parents creates two new offspring, therefore the total population size remains constant. It is helpful in this scheme if the population size is divisible by four. Another scheme, known as proportional crossover, uses the fitness score to assign a probability of survival S_i to each parent, such as

$$S_i = \frac{F_i}{\sum_{j=1}^{N} F_j} \tag{1.21}$$

Goldberg & Deb 1991. This, of course, necessitates that the fitness scores be positive values. This scheme introduces some randomness, where even less fit parents have some chance of producing offspring.

The next step in the GA is to create the next generation through the process of crossover. Two parents are chosen according to some scheme. One common

selection method is to choose the most and least fit surviving parents, then the second- most and second-least fit, etc. This ensures some degree of genetic diversity. Another method is to choose the most and second-most fit, the third and fourth most fit, etc. This is yet another parameter that gives the programmer some degree of control over the convergence of the algorithm. After selection of the parents, crossover occurs to create the next generation. The most commonly employed crossover scheme is single-point crossover, where a point in the chromosome is chosen to break and swap the bits to the right [Mitchell 1998]. This results in a new chromosome with some number of bits from each parent. In Figure 1.6 a crossover point of three is used to create the new chromosome. Notice that the first three bits of the first parent, in red, and the remaining seven from the second, in blue, are chosen to create the new chromosome. Multi-point crossover is another technique where multiple crossover points are chosen and the bits between two points are swapped between parents [De Jong & Spears 1992]. Multi-point crossover is most effective when the number of bits per chromosome is high.

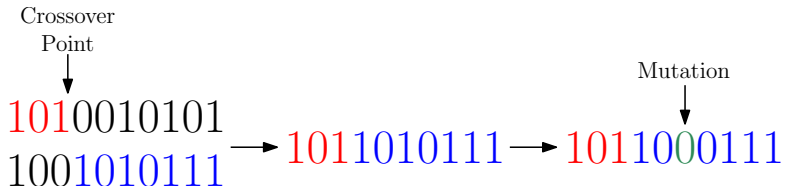

Figure 1.6: Example of single point crossover and mutation

Mutation introduces some degree of randomness to the GA to help ensure genetic diversity and convergence on a globally optimal solution. In mutation a random bit in a chromosome is altered, from zero to one or vice versa, according to some rate defined by the programmer. A higher mutation rate generally means more

genetic diversity in later stages of the algorithm, leading to a more thorough sampling of the search space. The process of mutation is shown in Figure 1.6 where the sixth bit of the chromosome is changed from a one to a zero, shown in green.

GAs have many lucrative benefits over non-evolutionary optimization techniques, such as direct search and gradient-based methods. Direct search relies solely upon the objective function and its constraints, requiring many function evaluations resulting in slow convergence. Gradient-based methods are not efficient when applied to non-differentiable or discontinuous problems. Both methods tend to be inefficient when handling discrete variables, and converge on local rather than global optimums [Deb 1999]. These limitations are overcome by GAs.

GAs are well matched to optimize unit cells of metamaterials due to their unit cell substructure, and have recently gained the attention of metamaterials researchers. Li et al. [2012] applied GAs to design unit cells for gradient refractive index (GRIN) lenses by optimizing the refractive index and impedance mismatch. Since a relatively inefficient finite element method was used, the genetic algorithm took approximately one week to converge upon an optimal solution. Silva et al. [2014] used GAs to control the radiation patterns of phased-array radar systems. They implemented maximum-minimum crossover, meaning that the most fit and least fit solutions were mated through crossover to produce the next generation. This ensures high genetic diversity and promotes convergence on a globally optimal solution. Jiang et al. [2011] implemented a GA to design infrared zero-index-metamaterials consisting of a dielectric layer sandwiched between two metallic screens by optimizing impedance and refractive index. Meng et al. [2012]

optimized the underwater sound absorption of locally resonant acoustic metamaterials based on the sonic crystal structure.

This dissertation addresses the problem of designing optimal unit cell configurations of membrane-type acoustic metamaterials to attenuate airborne sound. The response of a unit cell is modeled using a computationally efficient impedance-mobility approach, and optimized using a genetic algorithm.

1.4 Dissertation Structure

To address the limitations caused by computationally inefficient models on design and optimization applications, impedance-mobility modeling of membrane-type acoustic metamaterials is described in Chapter 2. The model is first formulated for a single unit cell, and then extended to multiple layers, arrays, and layers of arrays. The modeshape of a membrane carrying a concentrated mass is rigorously investigated to determine any potential limitations.

Chapter 3 verifies the accuracy of the impedance-mobility models using a finite element method. The assumptions in the model are also investigated and validated using the same method. The generalization of rectangular unit cell shapes to unit cells of other geometries is explored.

The application of genetic algorithms to optimize the transmission loss characteristics of membrane-type metamaterial structures is discussed in Chapter 4. The formulation of fitness functions to meet specific design criteria is discussed in detail.

Chapter 5 presents the results of the impedance-mobility models with parameters optimized using genetic algorithms. Case studies of specific noise control criteria and structures optimized to meet those criteria are presented.

Chapter 6 discusses the work done, its contributions to the field, and concludes with recommendations for future work.

Chapter 2

Impedance-Mobility Modeling

This chapter describes the formulation of efficient dynamic models for membrane-type acoustic metamaterials using the impedance-mobility approach. Models for a single unit cell, unit cells arrayed in parallel, and unit cells stacked in series are presented here. Quantities derived from the impedance-mobility approach that are useful for design and optimization are also discussed.

A single unit cell of a membrane-type acoustic metamaterial consists of a tensioned membrane carrying an attached mass supported by a rigid grid as seen in Figure 2.1. To model the transmission loss (TL) of a unit cell of a membrane-type acoustic metamaterial, the dynamic response of a membrane carrying an attached mass must be analyzed with consideration given to coupling of the surrounding fluid. The model can then be extended to examine the response of many unit cells arrayed in parallel, stacked in series, or both. This chapter begins with the formulation of a dynamic model for a single unit cell in a waveguide and expands the analysis to larger systems.

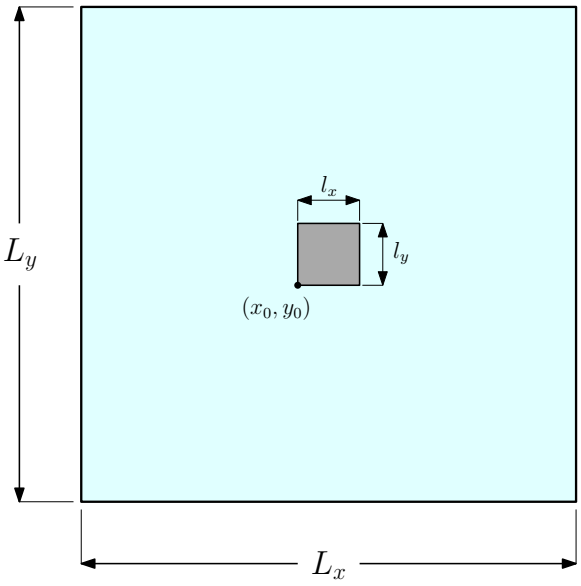

Figure 2.1: Schematic of rectangular unit cell

2.1 Unit Cell

The equation of motion for a membrane carrying an attached mass can be written as

$$\rho_s \frac{\partial^2 w}{\partial t^2} + \rho_{mass} \hbar(x, y, x_0, y_0, l_x, l_y) \frac{\partial^2 w}{\partial t^2} - T\nabla^2 w = 2\tilde{p}_{inc} e^{j\omega t} - 2\rho_0 c_0 \frac{\partial w}{\partial t}, \qquad (2.1)$$

where w is the transverse deflection of the membrane, ρ_s and T are the surface density and applied tension of the membrane, respectively, and ρ_{mass} is the surface density of the attached mass [Kopmaz & Telli 2002]. The amplitude of the incident plane wave is $\tilde{p}_{inc}$. The characteristic impedance of the fluid medium is given by $\rho_0 c_0$, and angular frequency is given by ω. A combination of four Heaviside unit-step

functions, denoted $\mathscr{H}$, is used to characterize the finite attached mass as follows

$$\begin{aligned}\hbar(x, y, x_0, y_0, l_x, l_y) = &[\mathscr{H}(x - x_0) - \mathscr{H}(x - x_0 - l_x)] \\ &\cdot [\mathscr{H}(y - y_0) - \mathscr{H}(y - y_0 - l_y)] .\end{aligned} \tag{2.2}$$

This function takes a value of 1 on the surface of the attached mass and 0 elsewhere on the membrane.

The formulation in Equation (2.1) assumes that the attached mass does not impede bending in the membrane, and that its rotational inertia is negligible. These assumptions are validated using finite element models in Chapter 3. A further assumption is that the membrane is limp and that its stiffness does not contribute significantly to the restoring force relative to the applied tension. The effect of membrane stiffness is explored in Section 2.1.2.

The transverse deflection of the membrane can be written using mode superposition as

$$w(x, y, t) = \sum_{m=1}^{M} \phi_m(x, y) q_m(t), \tag{2.3}$$

where $\phi_m(x, y)$ is the mode function which satisfies the boundary conditions, and $q_m(t)$ is the time-dependent modal amplitude $q_m(t) = \tilde{q}_m e^{j\omega t}$. Substituting Equation (2.3) into Equation (2.1), multiplying by an orthogonal mode function $\phi_n(x, y)$ and integrating over the surface of the membrane, the following equation is obtained

$$-\omega^2 M_m \tilde{q}_m - \omega^2 \sum_{n=1}^{N} Q_{m,n} \tilde{q}_n + K_m \tilde{q}_m = 2\tilde{p}_{inc} H_m - j\omega D_m \tilde{q}_m. \tag{2.4}$$

Equation (2.4) can be written in matrix-vector form as

$$-\omega^2 \left\{[\boldsymbol{M}] + [\boldsymbol{Q}]\right\} \tilde{\boldsymbol{q}} + j\omega \left\{\boldsymbol{D}\right\} \tilde{\boldsymbol{q}} + [\boldsymbol{K}] \tilde{\boldsymbol{q}} = 2\tilde{p}_{inc}\boldsymbol{H}. \tag{2.5}$$

The elements of the diagonal modal mass matrix, $\boldsymbol{M}$, are given by

$$M_m = \rho_s \int_0^{L_x} \int_0^{L_y} \phi_m \sum_{n=1}^{N} \phi_n \mathrm{d}y\mathrm{d}x. \tag{2.6}$$

The elements of the matrix $\boldsymbol{Q}$ corresponding to the attached mass are given by

$$Q_{m,n} = \rho_{mass} \int_{x_0}^{x_0+l_x} \int_{y_0}^{y_0+l_y} \phi_m \phi_n \mathrm{d}y\mathrm{d}x. \tag{2.7}$$

The damping due to air loading is given by $\boldsymbol{D}$ with elements

$$D_m = 2\rho_0 c_0 \int_0^{L_x} \int_0^{L_y} \phi_m \sum_{n=1}^{N} \phi_n \mathrm{d}y\mathrm{d}x \tag{2.8}$$

The stiffness matrix $\boldsymbol{K}$ is the diagonal matrix of elements given by

$$K_m = -T \int_0^{L_x} \int_0^{L_y} \phi_m \nabla^2 \sum_{n=1}^{N} \phi_n \mathrm{d}y\mathrm{d}x. \tag{2.9}$$

The modal volume displacement vector, $\boldsymbol{H}$, is given by

$$H_m = \int_0^{L_x} \int_0^{L_y} \phi_m \mathrm{d}y\mathrm{d}x. \tag{2.10}$$

The modal mobility matrix can be derived from Equation (2.5) as

$$\boldsymbol{Y} = \frac{j\omega}{-\omega^2 \{[\boldsymbol{M}] + [\boldsymbol{Q}]\} + j\omega[\boldsymbol{D}] + [\boldsymbol{K}]}, \tag{2.11}$$

and the modal vibration velocity amplitude is given by

$$\boldsymbol{V} = \boldsymbol{Y}\tilde{\boldsymbol{g}}_{\boldsymbol{p}}, \tag{2.12}$$

where $\tilde{\boldsymbol{g}}_{\boldsymbol{p}}$ is the generalized modal force vector due to the incident plane wave given by

$$\tilde{g}_{p,m} = 2\int_0^{L_x}\int_0^{L_y} \tilde{p}_{inc}\phi_m \mathrm{d}y\mathrm{d}x. \tag{2.13}$$

For frequencies in the plane wave regime of the waveguide, the sound pressure transmission coefficient can be written

$$t_p = \left| \frac{\rho_0 c_0 \langle v \rangle}{p_{inc}} \right|, \tag{2.14}$$

where $\langle v \rangle$ is the average velocity of the vibrating structure on the receiving side, and p_{inc} is the incident pressure amplitude [Chen et al. 2014a; Zhang et al. 2012]. The displacement of a vibrating structure can be written in terms of normal modes as

$$v(x,y) = \sum_{m=1}^{M} \phi_m(x,y)V_m = \boldsymbol{\Phi}^{\boldsymbol{T}}\boldsymbol{V}, \tag{2.15}$$

where $\boldsymbol{\Phi}$ is the column vector of area-normalized structural modeshapes, ϕ_m. The

average velocity can then be written

$$\langle v \rangle = \frac{1}{L_x L_y} \int_0^{L_x} \int_0^{L_y} v(x,y) \mathrm{d}y \mathrm{d}x = \frac{1}{L_x L_y} \boldsymbol{H^T V}. \tag{2.16}$$

The transmission coefficient is then written

$$t_p = \left| \frac{\rho_0 c_0 \boldsymbol{H^T V}}{L_x L_y \tilde{p}_{inc}} \right|, \tag{2.17}$$

where superscript T denotes vector transpose. The transmission loss can then be written

$$TL = -20 \log_{10}(t_p). \tag{2.18}$$

2.1.1 Baffled Transmission Loss

The transmitted sound power of a single unit cell in an infinitely extended rigid baffle can be calculated using the power transfer matrix based on modal radiation efficiencies [Fahy & Gardonio 2007; Snyder & Tanaka 1995]. The power transfer matrix, $[\boldsymbol{A}]$, for modes $\alpha = (p_\alpha, q_\alpha)$ and $\beta = (p_\beta, q_\beta)$ is given by

$$A_{\alpha\beta} = \frac{\rho_0 c_0 L_x L_y}{64} \left(1 + (-1)^{p_\alpha + p_\beta}\right) \left(1 + (-1)^{q_\alpha + q_\beta}\right) \left\{ \frac{p_\alpha q_\alpha}{p_\beta q_\beta} \sigma_\alpha + \frac{p_\beta q_\beta}{p_\alpha q_\alpha} \sigma_\beta \right\}, \tag{2.19}$$

where σ_α and σ_β are the radiation efficiencies of modes α and β, respectively, given by Wallace [1972] and in Appendix A. The total radiated sound power is given by

$$\Pi_{rad} = \boldsymbol{V}^H [\boldsymbol{A}] \boldsymbol{V}. \tag{2.20}$$

The sound power of the normally-incident plane wave is given by

$$\Pi_{inc} = \frac{|\tilde{p}_{inc}|^2 L_x L_y}{2\rho_0 c_0}. \tag{2.21}$$

The transmission loss is then

$$TL = -10 \log_{10} \left(\frac{\Pi_{rad}}{\Pi_{inc}} \right). \tag{2.22}$$

2.1.2 Membrane Stiffness

In the study of vibrating panels it is often assumed that the panel behaves either as a membrane or a plate [Kinsler et al. 2000]. The distinction is in the restoring force in the equation of motion. A membrane's restoring force is due to an applied tension, whereas the restoring force of a plate is due to its flexural rigidity. This assumption also holds for the modeling of membrane-type acoustic metamaterials. In most analytical models, a membrane model is used [Langfeldt et al. 2015; Tian et al. 2014; Zhang et al. 2012], while some use a plate model [Lu et al. 2016; Li et al. 2014]. Chen et al. published two papers on the subject, one with a membrane model [Chen et al. 2014a], and one with a plate model [Chen et al. 2014b].

The fact is, however, that the vibratory motion of any real structure is influenced by both its flexural rigidity and any applied tension [Leissa 1969]. In the present research, both are considered. This section and A.1.3 discuss the addition of bending stiffness to a membrane model. Since the degree to which the tension and stiffness affect the TL of the unit cell varies with configuration, in some cases it may

be appropriate to neglect one or the other.

An underlying assumption in the equation of motion given by Equation (2.1) is that the bending stiffness of the membrane is negligible compared to the applied tension. There may exist, however, certain design scenarios in which stiffer materials are more suitable. This section outlines the adaptation of the single unit cell impedance-mobility model to include the effects of membrane bending stiffness.

Generally, the equation of motion for a membrane or thin plate with both in-plane tension and bending stiffness can be written [Leissa 1969]:

$$D\nabla^4 w - T\nabla^2 w = -\rho_s \frac{\partial^2 w}{\partial t^2}, \tag{2.23}$$

where D is the flexural rigidity of the membrane given by

$$D = \frac{Eh^3}{12(1-\nu^2)}, \tag{2.24}$$

which is dependent upon the Young's Modulus, E, Poisson's Ratio, ν, and thickness, h, of the membrane.

Incorporating the additional stiffness term into Equation (2.1) and following the same derivation as above, Equation (2.5) becomes:

$$-\omega^2 \left\{[\boldsymbol{M}] + [\boldsymbol{Q}]\right\} \tilde{\boldsymbol{q}} + j\omega \left\{\boldsymbol{D}\right\} \tilde{\boldsymbol{q}} + [\boldsymbol{K}]\, \tilde{\boldsymbol{q}} + [\boldsymbol{E}]\, \tilde{\boldsymbol{q}} = 2\tilde{p}_{inc}\boldsymbol{H}, \tag{2.25}$$

where $\boldsymbol{E}$ is the diagonal stiffness matrix due to the flexural rigidity of the membrane

defined by

$$E_m = D \int_0^{L_x} \int_0^{L_y} \phi_m \nabla^4 \sum_{n=1}^{N} \phi_n \mathrm{d}y\mathrm{d}x. \tag{2.26}$$

The structural mobility matrix can then be written as

$$\boldsymbol{Y} = \frac{j\omega}{-\omega^2 \left\{[\boldsymbol{M}] + [\boldsymbol{Q}]\right\} + j\omega[\boldsymbol{D}] + [\boldsymbol{K}] + [\boldsymbol{E}]}. \tag{2.27}$$

2.2 Cell Array

For two or more unit cells arrayed in parallel as shown in Figure 2.2, the acoustic pressure radiated from each cell affects the vibration of each surrounding cell to a varying degree that depends on distance and frequency. To account for this interaction effect, Equation (2.1) is modified by adding a term that is proportional to the transfer impedance between each pair of unit cells and each unit cell's vibration velocity.

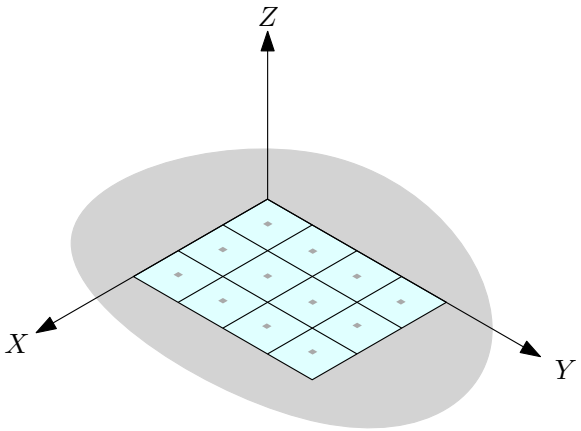

Figure 2.2: 3x4 array of unit cells in a rigid baffle

The equation of motion for a single unit cell in an array of K cells, denoted i

where $i = 1, 2...K$, with general external pressures, $\tilde{p}_{ext,i}$ due to arbitrary sources is written as

$$\rho_s \frac{\partial^2 w_i}{\partial t^2} + \rho_{mass} \hbar(x, y, x_0, y_0, l_x, l_y) \frac{\partial^2 w_i}{\partial t^2} - T\nabla^2 w_i = 2\tilde{p}_{inc} e^{j\omega t} + 2\tilde{p}_{ext,i} e^{j\omega t}. \quad (2.28)$$

$\tilde{p}_{ext,i}$ can be written as a sum of contributions from each unit cell in the array as

$$\tilde{p}_{ext,i} = \sum_{j=1}^{K} \tilde{p}_{ij}. \quad (2.29)$$

The pressure on any individual unit cell due to the vibration of adjacent unit cells can be approximated by assuming that the array behaves as a set of elementary piston-like radiators. This approximation is valid when the characteristic dimension, a, of the unit cell is much less than the acoustic and flexural wavelength, $a = \sqrt{L_x L_y} \ll \lambda$. From Rayleigh's integral the pressure at one unit cell due to the vibration velocity of another can be related through self- and mutual- radiation impedances (see Appendix B of Chazot & Guyader 2007). The radiation impedance is defined as the ratio of pressure at unit cell i due to the average vibration velocity at unit cell j, given by

$$\tilde{Z}_{ij} = \frac{\tilde{p}_i}{\langle V \rangle_j} \quad (2.30)$$

$$\tilde{Z}_{ij} = \begin{cases} \rho_0 c[1 - e^{-jka}] & \text{if } i = j \\ \frac{j\omega\rho_0 L_x L_y}{2\pi} \frac{e^{-jkd_{ij}}}{d_{ij}} & \text{if } i \neq j \end{cases} \quad (2.31)$$

where d_{ij} is the distance between centers of unit cells i and j. Equation (2.29) can

be rewritten as

$$\tilde{p}_{ext,i} = \sum_{j=1}^{K} \tilde{Z}_{ij} \langle V \rangle_j = j\omega \sum_{j=1}^{K} \tilde{Z}_{ij} \langle w \rangle_j, \tag{2.32}$$

where $\langle w \rangle_j$ is the spatially averaged displacement of cell j calculated by

$$\langle w \rangle_j = \frac{1}{L_x L_y} \int_0^{L_x} \int_0^{L_y} w_j \mathrm{d}y \mathrm{d}x. \tag{2.33}$$

The average displacement can be rewritten using the mode superposition in Equation (2.3) and the definition of modal displacement given by Equation (2.10) as

$$\langle w \rangle_j = \frac{1}{L_x L_y} \sum_{m=1}^{M} H_m \tilde{q}_{m,j} e^{j\omega t} = \frac{1}{L_x L_y} \boldsymbol{H}^T \tilde{\boldsymbol{q}}_{\boldsymbol{j}} e^{j\omega t}. \tag{2.34}$$

Substituting Equations (2.34), (2.32) and (2.3) into Equation (2.28) and, without loss of generality, omitting the $e^{j\omega t}$ convention gives

$$\begin{aligned} -\omega^2 \rho_s \sum_{m=1}^{M} \phi_m \tilde{q}_{m,i} - \omega^2 \rho_{mass} \hbar \sum_{m=1}^{M} \phi_m \tilde{q}_{m,i} - T\nabla^2 \sum_{m=1}^{M} \phi_m \tilde{q}_{m,i} \\ = 2\tilde{p}_{inc} + \frac{2j\omega}{L_x L_y} \sum_{j=1}^{K} \tilde{Z}_{ij} \boldsymbol{H}^T \tilde{\boldsymbol{q}}_{\boldsymbol{j}}. \end{aligned} \tag{2.35}$$

Multiplying Equation (2.35) by ϕ_n, integrating over surface of cell i and using orthogonality properties gives

$$\begin{aligned} -\omega^2 M_{m,i} \tilde{q}_{m,i} - \omega^2 \sum_{n=1}^{N} Q_{m,n,i} \tilde{q}_{n,i} + K_{m,i} \tilde{q}_{m,i} \\ = 2\tilde{p}_{inc} H_m + \frac{2j\omega}{L_x L_y} H_m \sum_{j=1}^{K} \tilde{Z}_{ij} \boldsymbol{H}^T \tilde{\boldsymbol{q}}_{\boldsymbol{j}}. \end{aligned} \tag{2.36}$$

In matrix-vector form, Equation (2.36) is

$$-\omega^2 \left\{[\boldsymbol{M_i}] + [\boldsymbol{Q_i}]\right\} \tilde{\boldsymbol{q}}_{\boldsymbol{i}} + [\boldsymbol{K_i}]\, \tilde{\boldsymbol{q}}_{\boldsymbol{i}} = 2\tilde{p}_{inc}\boldsymbol{H} + \frac{2j\omega}{L_x L_y}\boldsymbol{H}^T\, [\tilde{\boldsymbol{q}}]\, \tilde{\boldsymbol{Z}}_{\boldsymbol{i}}\boldsymbol{H}, \tag{2.37}$$

where the bracketed $[\tilde{\boldsymbol{q}}]$ is the matrix formed by modal amplitude vectors for each of K cells

$$[\tilde{\boldsymbol{q}}] = \lfloor \tilde{\boldsymbol{q}}_1, \tilde{\boldsymbol{q}}_2, \ldots, \tilde{\boldsymbol{q}}_{\boldsymbol{K}} \rfloor, \tag{2.38}$$

and $\{\tilde{\boldsymbol{Z}}_{\boldsymbol{i}}\}$ is the vector of transfer impedances

$$\{\tilde{\boldsymbol{Z}}_{\boldsymbol{i}}\} = \lfloor \tilde{Z}_{i,1}, \tilde{Z}_{i,2}, \ldots, \tilde{Z}_{i,K} \rfloor^T. \tag{2.39}$$

To solve for the modal amplitude vector $\tilde{\boldsymbol{q}}_{\boldsymbol{i}}$, the components of $[\tilde{\boldsymbol{q}}]$ and $\{\tilde{\boldsymbol{Z}}_{\boldsymbol{i}}\}$ corresponding to the i^{th} cell are separated, leaving

$$[\tilde{\boldsymbol{q}}'_{\boldsymbol{i}}] = \lfloor \tilde{\boldsymbol{q}}_1, \ldots, \tilde{\boldsymbol{q}}_{i-1}, \tilde{\boldsymbol{q}}_{i+1}, \ldots, \tilde{\boldsymbol{q}}_{\boldsymbol{K}} \rfloor, \tag{2.40}$$

and

$$\{\tilde{\boldsymbol{Z}}'_{\boldsymbol{i}}\} = \lfloor \tilde{Z}_{i,1}, \ldots, \tilde{Z}_{i,i-1}, \tilde{Z}_{i,i+1}, \ldots, \tilde{Z}_{i,K} \rfloor^T. \tag{2.41}$$

The elements of $\{\tilde{\boldsymbol{Z}}'_{\boldsymbol{i}}\}$ are given by Equation (2.31) for $i \neq j$.

Equation (2.37) then becomes

$$-\omega^2\left\{[\boldsymbol{M_i}]+[\boldsymbol{Q_i}]\right\}\tilde{\boldsymbol{q}}_{\boldsymbol{i}}+[\boldsymbol{K_i}]\,\tilde{\boldsymbol{q}}_{\boldsymbol{i}} = 2\tilde{p}_{inc}\boldsymbol{H}+\frac{2j\omega}{L_xL_y}\tilde{Z}_{i,i}\boldsymbol{H}^T\boldsymbol{H}\tilde{\boldsymbol{q}}_{\boldsymbol{i}}+\frac{2j\omega}{L_xL_y}\boldsymbol{H}^T\left[\tilde{\boldsymbol{q}}_{\boldsymbol{i}}'\right]\{\tilde{\boldsymbol{Z}}_{\boldsymbol{i}}'\}\boldsymbol{H}. \quad (2.42)$$

Solving for $\tilde{\boldsymbol{q}}_{\boldsymbol{i}}$ gives

$$\tilde{\boldsymbol{q}}_{\boldsymbol{i}}=\frac{2\tilde{p}_{inc}\boldsymbol{H}+\frac{2j\omega}{L_xL_y}\boldsymbol{H}^T\left[\tilde{\boldsymbol{q}}_{\boldsymbol{i}}'\right]\{\tilde{\boldsymbol{Z}}_{\boldsymbol{i}}'\}\boldsymbol{H}}{-\omega^2\left\{[\boldsymbol{M_i}]+[\boldsymbol{Q_i}]\right\}+[\boldsymbol{K_i}]-\frac{2j\omega}{L_xL_y}\tilde{Z}_{i,i}\boldsymbol{H}^T\boldsymbol{H}}. \quad (2.43)$$

2.2.1 2 x 1 Array

Note that the vibration amplitude vector for each unit cell is a function of the vibration amplitude vectors for all other unit cells in the array. This necessitates solving a system of K equations and K unknown vectors, which can be difficult. In this section the transmission loss of an array consisting of $K = 2$ unit cells is derived to illustrate the process of expanding the analysis to multi-celled arrays.

The modal vibration amplitude vectors for unit cell 1 and 2 are written using Equation (2.43)

$$\tilde{\boldsymbol{q}}_{\boldsymbol{1}}=\frac{2\tilde{p}_{inc}\boldsymbol{H}+\frac{2j\omega}{L_xL_y}\tilde{Z}_{12}\boldsymbol{H}^T\tilde{\boldsymbol{q}}_{\boldsymbol{2}}\boldsymbol{H}}{-\omega^2\left\{[\boldsymbol{M_1}]+[\boldsymbol{Q_1}]\right\}+[\boldsymbol{K_1}]-\frac{2j\omega}{L_xL_y}\tilde{Z}_{11}\boldsymbol{H}^T\boldsymbol{H}}, \quad (2.44)$$

and

$$\tilde{\boldsymbol{q}}_{\boldsymbol{2}}=\frac{2\tilde{p}_{inc}\boldsymbol{H}+\frac{2j\omega}{L_xL_y}\tilde{Z}_{21}\boldsymbol{H}^T\tilde{\boldsymbol{q}}_{\boldsymbol{1}}\boldsymbol{H}}{-\omega^2\left\{[\boldsymbol{M_2}]+[\boldsymbol{Q_2}]\right\}+[\boldsymbol{K_2}]-\frac{2j\omega}{L_xL_y}\tilde{Z}_{22}\boldsymbol{H}^T\boldsymbol{H}}, \quad (2.45)$$

respectively. Note that in the second term in the numerator of each equation $[\tilde{\boldsymbol{q}}_1'] = \tilde{\boldsymbol{q}}_2$ and $[\tilde{\boldsymbol{q}}_2'] = \tilde{\boldsymbol{q}}_1$, respectively, and that $\{\tilde{\boldsymbol{Z}}_1'\}$ and $\{\tilde{\boldsymbol{Z}}_2'\}$ become scalar values $\tilde{Z}_{12}$ and $\tilde{Z}_{21}$.

For convenience in notation, the matrix that corresponds to the equation of motion of the i^{th} unit cell can be defined as

$$[\boldsymbol{\Sigma_i}] = -\omega^2 \{[\boldsymbol{M_i}] + [\boldsymbol{Q_i}]\} + [\boldsymbol{K_i}] - \frac{2j\omega}{L_x L_y} \tilde{Z}_{ii} \boldsymbol{H}^T \boldsymbol{H}. \tag{2.46}$$

Substituting Equation (2.45) into (2.44) and using (2.46), the fully coupled modal vibration amplitude vectors are written

$$\tilde{\boldsymbol{q}}_1 = \frac{2\tilde{p}_{inc}\boldsymbol{H} + \frac{2j\omega}{L_x L_y} 2\tilde{p}_{inc}\tilde{Z}_{12}\boldsymbol{H}^T [\boldsymbol{\Sigma_2}]^{-1} \boldsymbol{H}\boldsymbol{H}}{[\boldsymbol{\Sigma_1}] + \frac{4\omega^2}{(L_x L_y)^2}\tilde{Z}_{12}\tilde{Z}_{21}\boldsymbol{H}^T [\boldsymbol{\Sigma_2}]^{-1} \boldsymbol{H}\boldsymbol{H}\boldsymbol{H}^T}, \tag{2.47}$$

and

$$\tilde{\boldsymbol{q}}_2 = \frac{2\tilde{p}_{inc}\boldsymbol{H} + \frac{2j\omega}{L_x L_y} 2\tilde{p}_{inc}\tilde{Z}_{21}\boldsymbol{H}^T [\boldsymbol{\Sigma_1}]^{-1} \boldsymbol{H}\boldsymbol{H}}{[\boldsymbol{\Sigma_2}] + \frac{4\omega^2}{(L_x L_y)^2}\tilde{Z}_{21}\tilde{Z}_{12}\boldsymbol{H}^T [\boldsymbol{\Sigma_1}]^{-1} \boldsymbol{H}\boldsymbol{H}\boldsymbol{H}^T}. \tag{2.48}$$

The total sound power radiated from the array is calculated by considering each unit cell as a piston radiator in an infinite rigid baffle, with velocity equal to its average value across the unit cell. The average velocity is calculated by

$$\langle V \rangle_j = j\omega \langle w \rangle_j, \tag{2.49}$$

where $\langle w \rangle_j$ is given by dropping the $e^{j\omega t}$ from Equation (2.34). The total radiated

sound power is then given by

$$\Pi_{rad} = \boldsymbol{V_e}^H [\boldsymbol{R}] \boldsymbol{V_e}, \tag{2.50}$$

where $\boldsymbol{V_e}$ is the vector of elementary velocities given by

$$\boldsymbol{V_e} = \begin{Bmatrix} \langle V \rangle_1 \\ \langle V \rangle_2 \end{Bmatrix}, \tag{2.51}$$

and $[\boldsymbol{R}]$ is the radiation resistance matrix [Fahy & Gardonio 2007] defined for $K = 2$ elements by

$$[\boldsymbol{R}] = \frac{\omega^2 \rho_0 A_e^2}{4\pi c} \begin{bmatrix} 1 & \frac{\sin kd_{12}}{kd_{12}} \\ \frac{\sin kd_{21}}{kd_{21}} & 1 \end{bmatrix}, \tag{2.52}$$

where d_{ij} is the distance between unit cells i and j. The transmission loss can then be calculated using the incident sound power,

$$\Pi_{inc} = \frac{|\tilde{p}_{inc}|^2 S}{2\rho_0 c_0}, \tag{2.53}$$

where S is the total area of the array, Equations (2.50), and (2.22).

2.2.2 Negligible Coupling Model

As illustrated in the previous section, expanding the analysis to a large number of unit cells in an array can be challenging. To obtain an estimate of the total TL of

an array consisting of an arbitrary number of elements, while sacrificing some accuracy, the effect of mutual coupling can be neglected. The assumption of negligible coupling between unit cells allows the vibration velocity of each unit cell to be calculated independently and combined to find the total sound power radiated by the array. The velocity of an elementary radiator, $V_{e,i}$, of the i^{th} unit cell is the average velocity over the surface given by

$$V_{e,i} = \frac{1}{L_x L_y} \boldsymbol{H}^T \boldsymbol{Y_i} \boldsymbol{g_p}. \tag{2.54}$$

The elementary velocities can be combined, as in the previous section, for K unit cells in an array by using the radiation resistance matrix

$$[\boldsymbol{R}] = \frac{\omega^2 \rho_0 A_e^2}{4\pi c} \begin{bmatrix} 1 & \frac{\sin kR_{12}}{kR_{12}} & \cdots & \frac{\sin kR_{1K}}{kR_{1K}} \\ \frac{\sin kR_{21}}{kR_{21}} & 1 & & \frac{\sin kR_{2K}}{kR_{2K}} \\ \vdots & & \ddots & \vdots \\ \frac{\sin kR_{K1}}{kR_{K1}} & \frac{\sin kR_{K2}}{kR_{K2}} & \cdots & 1 \end{bmatrix}. \tag{2.55}$$

The total radiated sound power is then calculated using Equation (2.50).

2.3 Two Layers

Consider the cross section of a rigid walled cavity of dimension $(L_x \times L_y \times L_z)$ set in a waveguide with two simply supported membrane-type acoustic metamaterial unit cells located at $z = 0$ and $z = L_z$, shown in Figure 2.3. The vibratory response of

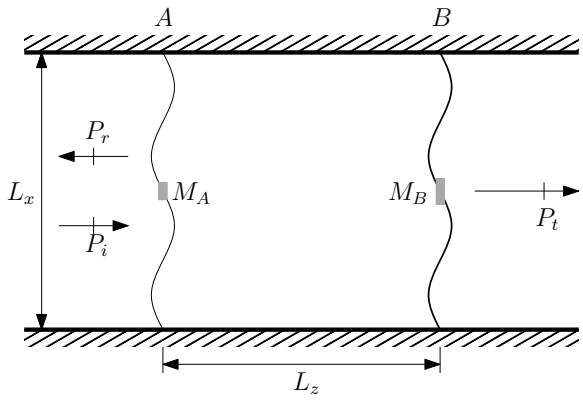

Figure 2.3: Cross-section of two stacked unit cells

each unit cell is affected not only by the incident pressure, but by the pressure in the cavity as well. This creates a coupled system of governing equations that must be solved simultaneously to obtain the steady-state response.

The responses of the panels and cavity can be written as a summation of normal modes. The cavity pressure p and panel velocities v_i, where i is either A or B, are written as

$$p(x,y,z,t) = \sum_{n=1}^{N} \psi_n(x,y,z) P_n(t), \tag{2.56}$$

$$v_i(x,y,t) = \sum_{m=1}^{M} \phi_m(x,y) V_{i,m}(t), \tag{2.57}$$

where ψ_n and ϕ_m are the normalized acoustic and structural modes given by

$$\psi_n(x,y,z) = \sqrt{e_1 e_2 e_3} \cos\left(\frac{n_1 \pi x}{L_x}\right) \cos\left(\frac{n_2 \pi y}{L_y}\right) \cos\left(\frac{n_3 \pi z}{L_z}\right), \tag{2.58}$$

where $e_i = 1$ for $n_i = 0$ and $e_i = 2$ if $n_i > 0$, and

$$\phi_m(x,y) = 2\sin\left(\frac{m_1\pi x}{L_x}\right)\sin\left(\frac{m_2\pi y}{L_y}\right). \tag{2.59}$$

The governing equations for the coupled acoustic cavity pressure P, panel A velocity V_A, and panel B velocity V_B are given in modal terms by [Jin et al. 2009]

$$\ddot{P}_n + 2\xi_n\omega_n\dot{P}_n + \omega_n^2 P_n = \frac{\rho_0 c_0^2}{j\omega V}\sum_{m=1}^{M} C_{m,n}^A \ddot{V}_{Am} - \frac{\rho_0 c_0^2}{j\omega V}\sum_{m=1}^{M} C_{m,n}^B \ddot{V}_{Bm}, \tag{2.60}$$

$$\ddot{V}_{Am} + 2\xi_{Am}\omega_{Am}\dot{V}_{Am} + \omega_{Am}^2 V_{Am} = \frac{j\omega}{M_{Am}}\left(g_{pm} - \sum_{n=1}^{N} C_{m,n}^A P_n\right), \tag{2.61}$$

and

$$\ddot{V}_{Bm} + 2\xi_{Bm}\omega_{Bm}\dot{V}_{Bm} + \omega_{Bm}^2 V_{Bm} = \frac{j\omega}{M_{Bm}}\sum_{n=1}^{N} C_{m,n}^B P_n, \tag{2.62}$$

respectively. The modal coupling coefficient, $C_{m,n}^i$, of the m^{th} structural mode of the i^{th} unit cell to the n^{th} acoustic mode of the cavity is given by

$$C_{m,n}^i = \int_0^{L_x}\int_0^{L_y} \psi_n(x,y,z_i)\phi_m(x,y)\mathrm{d}y\mathrm{d}x, \tag{2.63}$$

where z_i is the z-coordinate of the i^{th} unit cell, either 0 or L_z.

Equations (2.60)-(2.62) can be written in matrix form as

$$\boldsymbol{P} = \boldsymbol{Z_a}(\boldsymbol{C_A}\boldsymbol{V_A} - \boldsymbol{C_B}\boldsymbol{V_B}), \tag{2.64}$$

$$\boldsymbol{V_A} = \boldsymbol{Y_A}(\boldsymbol{g_p} - \boldsymbol{C_A^T}\boldsymbol{P}), \tag{2.65}$$

and

$$\boldsymbol{V_B} = \boldsymbol{Y_B}\boldsymbol{C_B^T}\boldsymbol{P}, \tag{2.66}$$

respectively.

Combining the system of three equations and three unknown variables given by Equations (2.64)-(2.66) and isolating the dependent variables gives

$$\boldsymbol{P} = (\boldsymbol{I} + \boldsymbol{Z_a}\boldsymbol{C_A}\boldsymbol{Y_A}\boldsymbol{C_A^T} + \boldsymbol{Z_a}\boldsymbol{C_B}\boldsymbol{Y_B}\boldsymbol{C_B^T})^{-1}\boldsymbol{Z_a}\boldsymbol{C_A}\boldsymbol{Y_A}\boldsymbol{g_p}, \tag{2.67}$$

$$\boldsymbol{V_A} = \left[\boldsymbol{I} + \boldsymbol{Y_A}\boldsymbol{C_A^T}(\boldsymbol{I} + \boldsymbol{Z_a}\boldsymbol{C_B}\boldsymbol{Y_B}\boldsymbol{C_B^T})^{-1}\boldsymbol{Z_a}\boldsymbol{C_A}\right]^{-1}\boldsymbol{Y_A}\boldsymbol{g_p}, \tag{2.68}$$

and

$$\begin{aligned}\boldsymbol{V_B} = &\left[\boldsymbol{I} + \boldsymbol{Y_B}\boldsymbol{C_B^T}(\boldsymbol{I} + \boldsymbol{Z_a}\boldsymbol{C_A}\boldsymbol{Y_A}\boldsymbol{C_A^T})^{-1}\boldsymbol{Z_a}\boldsymbol{C_B}\right]^{-1}\boldsymbol{Y_B} \\ &\cdot\left[\boldsymbol{C_B^T}(\boldsymbol{I} + \boldsymbol{Z_a}\boldsymbol{C_A}\boldsymbol{Y_A}\boldsymbol{C_A^T})^{-1}\boldsymbol{Z_a}\boldsymbol{C_A}\boldsymbol{Y_A}\boldsymbol{g_p}\right].\end{aligned} \tag{2.69}$$

The uncoupled acoustic impedance [Kim & Brennan 1999; Dowell et al. 1977] of the cavity $\boldsymbol{Z_a}$ is given by

$$\boldsymbol{Z_a} = \frac{\boldsymbol{A}\rho_0 c_0^2}{V}, \tag{2.70}$$

where $\boldsymbol{A}$ is a diagonal matrix with elements given by

$$A_1 = \frac{1}{1/T_a + j\omega}, \tag{2.71}$$

for $n = 1$ and

$$A_n = \frac{j\omega}{\omega_n^2 - \omega^2 + j2\zeta_n\omega_n\omega}, \tag{2.72}$$

for $n \neq 1$.

The uncoupled structural mobility for panels A and B, Y_A and Y_B respectively, can be written [Zhang et al. 2012; Fahy & Gardonio 2007]

$$\boldsymbol{Y_i} = \frac{j\omega}{-\omega^2\{[\boldsymbol{M_i}] + [\boldsymbol{Q_i}]\} + j\omega[\boldsymbol{D_i}] + [\boldsymbol{K_i}]}, \tag{2.73}$$

where i denotes either panel A or B.

The sound pressure transmission coefficient can be written

$$t_p = \left| \frac{\rho_0 c_0 \langle v \rangle}{p_i} \right|, \tag{2.74}$$

where $\langle v \rangle$ is the average velocity of the vibrating structure on the receiving side, and p_i is the incident pressure amplitude. The velocity of a vibrating structure can be written in terms of normal modes as

$$v(x,y) = \sum_{m=1}^{M} \phi_m(x,y) V_{B,m} = \boldsymbol{\Phi^T V_B}, \tag{2.75}$$

where $\mathbf{\Phi}$ is the column vector of area-normalized structural modeshapes, ϕ_m. The average velocity can then be written

$$\langle v \rangle = \frac{1}{L_x L_y} \int_0^{L_x} \int_0^{L_y} v(x,y) \mathrm{d}y \mathrm{d}x = \frac{1}{L_x L_y} \boldsymbol{H^T V_B}. \tag{2.76}$$

The transmission coefficient is then written

$$t_p = \left| \frac{\rho_0 c_0 \boldsymbol{H^T V_B}}{L_x L_y \tilde{p}_{inc}} \right|, \tag{2.77}$$

2.4 Derived Quantities

The flexibility of the impedance-mobility approach allows the derivation of several quantities, in addition to TL, that may be useful to noise control engineers. When discussing metamaterials, the idea of a negative effective dynamic mass often arises. The reflection and absorption coefficients are important when considering the sound field on both sides of the barrier. In active control, panel kinetic energy and cavity potential energy are often used as control variables. The impedance-mobility approach directly calculates modal displacement, velocity, and cavity pressure amplitudes. This section delineates the equations necessary to derive useful quantities from values calculated via the impedance-mobility approach.

2.4.1 Effective Dynamic Mass

The effective dynamic mass can be derived from Newton's second law of motion $F = ma$ [Naify et al. 2010]. Likewise, the effective dynamic density can be found by dividing by the surface area of the membrane [Yang et al. 2008]. The average force due to acoustic excitation acting on the metamaterial unit cell is found using the generalized modal force vector $\tilde{\boldsymbol{g}}_{\boldsymbol{p}}$ and the modal volume displacement vector $\boldsymbol{H}$,

$$\langle F \rangle = \frac{\boldsymbol{H}^{\boldsymbol{T}} \tilde{\boldsymbol{g}}_{\boldsymbol{p}}}{L_x L_y}. \tag{2.78}$$

The average out-of-plane acceleration is found using the modal velocity amplitude vector, $\boldsymbol{V}$, of the radiating unit cell and is given by

$$\langle a_z \rangle = \frac{j\omega \boldsymbol{V}^H \boldsymbol{H}}{L_x L_y}, \tag{2.79}$$

where superscript H denotes Hermitian transpose. Dividing Equation (2.78) by Equation (2.79) gives the effective dynamic mass

$$m_{eff} = \frac{\boldsymbol{H}^{\boldsymbol{T}} \tilde{\boldsymbol{g}}_{\boldsymbol{p}}}{j\omega \boldsymbol{V}^{\boldsymbol{H}} \boldsymbol{H}}. \tag{2.80}$$

2.4.2 Reflection and Absorption Coefficients

The sound pressure reflection coefficient is the ratio of reflected to incident sound pressure. It is defined as

$$r_p = 1 - t_p, \tag{2.81}$$

where t_p is the sound pressure transmission coefficient defined by Equation (2.17) for a single unit cell in a waveguide, or Equation (2.77) for a double layer of unit cells in a waveguide. The sound power transmission and reflection coefficients are given by $T_\Pi = |t_p|^2$, and $R_\Pi = |r_p|^2$, respectively.

The sound absorption coefficient, α, is the fractional portion of the incident energy that is not reflected or transmitted. It is calculated from the sound power transmission and reflection coefficients as

$$\alpha = 1 - T_\Pi - R_\Pi. \tag{2.82}$$

2.4.3 Panel Kinetic Energy

The kinetic energy of a vibrating panel is a useful quantity in active vibration control. Membrane-type acoustic metamaterials are a prime candidate for active structural control, since the vibration patterns directly influence the amount of sound reflection. It is easy to imagine attaching a mechanical actuator to the attached mass or replacing it with a piezoelectric actuator to actively control the resonance frequencies. The kinetic energy of a vibrating surface can be written

$$E_k = \rho_s \int_0^{L_x} \int_0^{L_y} |v(x, y, \omega)|^2 \, \mathrm{d}y\mathrm{d}x. \tag{2.83}$$

Jin et al. [2009] derived the kinetic energy of a panel using the impedance-mobility approach as

$$E_k = \rho_s L_x L_y \boldsymbol{V}^{\boldsymbol{H}} \boldsymbol{V}. \tag{2.84}$$

2.4.4 Cavity Potential Energy

For a membrane-type acoustic metamaterial configuration consisting of two unit cells in series with an acoustic cavity between them, it may be useful to consider the potential energy within the cavity. Once again, the ease of extending a double layer configuration to actively control sound transmission loss is evident. By placing an acoustic control source inside the cavity, the excitation of the radiating unit cell can be minimized, reducing the amount of sound transmitted through the barrier. The impedance-mobility approach greatly simplifies this extension.

The acoustic potential energy inside a rectangular cavity is defined as

$$E_p = \frac{1}{4\rho_0 c_0^2} \int_0^{L_x} \int_0^{L_y} \int_0^{L_z} |p(x,y,z,\omega)|^2 \, \mathrm{d}z\mathrm{d}y\mathrm{d}x. \tag{2.85}$$

Jin et al. [2009] derived the cavity potential energy using the impedance-mobility approach in terms of the cavity modal pressure amplitude, $\boldsymbol{P}$, as

$$E_p = \frac{V}{4\rho_0 c_0^2} \boldsymbol{P}^{\boldsymbol{H}} \boldsymbol{P}. \tag{2.86}$$

2.5 Concluding Remarks

This chapter presents the formulation of impedance-mobility models of membrane-type acoustic metamaterials in various configurations. The models of single unit cells in a waveguide and in a baffle are extended to larger systems comprised of multiple unit cells, either stacked in series in a waveguide, or arrayed

in parallel in a baffle. A fully-coupled formulation for a 2×1 array in a baffle is presented, as well as a model with a negligible coupling assumption for an arbitrary number of unit cells. Useful quantities are derived from the impedance-mobility models, including effective dynamic mass, reflection and absorption coefficients, panel kinetic energy, and cavity potential energy.

Implementing the impedance-mobility models presented in this chapter and expanded upon in Appendices A and E results in computationally efficient dynamic models of membrane-type acoustic metamaterials. These models are useful for creating design tools, and optimization using iterative schemes. The verification of these models is presented in Chapter 3.

Chapter 3

Finite Element Verification

This chapter presents the verification of the accuracy and the validation of assumptions of the impedance-mobility models formulated in Chapter 2 using a finite element method (FEM) [Zienkiewicz et al. 1977]. The assumptions that the bending stiffness and rotary inertia of the attached mass are negligible are tested. The generalization of the impedance-mobility model for rectangular membranes and masses to systems of other shapes is also explored using FEM and presented in this chapter. Circular, hexagonal, and triangular unit cell configurations are compared to results of the impedance-mobility model which assumes a square unit cell of equal area.

The acoustics module of the commercial FEM software package COMSOL Multiphysics version 4.3 is used in this research. Unless otherwise noted, tetrahedral elements are used with a quadratic shape function and a non-linear solver [COMSOL Multiphysics 2012]. The impedance-mobility models are implemented using custom scripts in MathWorks MATLAB 2015a. All FEM computations were

performed on a Windows server with two Intel Xeon E5-2670 2.6 GHz processors and 16 gigabytes of RAM.

3.1 Verification of Accuracy

This section verifies the accuracy of the impedance-mobility approach by comparing transmission loss results to those obtained using FEM models. FEM has been used in previous studies of membrane-type acoustic metamaterials (see, for example, Chen et al. 2014a; Naify et al. 2012; Yang et al. 2008) and compared against experimental results, with good agreement. Naify et al. 2012 reported less than 10 percent difference between FEM and measured transmission loss (TL).

The TL curves of a single unit cell in a waveguide and a baffle, multi-cellular arrays in baffles, and a double layer of unit cells in waveguide are verified using FEM.

3.1.1 Unit Cell in a Waveguide

The FEM model used to verify the accuracy of the impedance-mobility model of a single unit cell set in a rectangular waveguide is a three-dimensional acoustic-structure interaction model. This model is the most realistic configuration, using a finite thickness membrane and mass. Three boxes are used to represent the membrane, mass, and waveguide geometry as shown in Figure 3.1 (A). In the frequency range of interest from 100 Hz to 4000 Hz, only plane wave modes propagate in the waveguide due to its small width and height compared to a

wavelength of sound in air. The infinitely long waveguide is approximated by using a matched boundary condition that matches the plane wave mode at the ends of the waveguide. The walls of the waveguide are sound-hard boundaries that perfectly reflect incident waves. The dimensions and material parameters used in the model are the baseline parameters given in Table B.1.

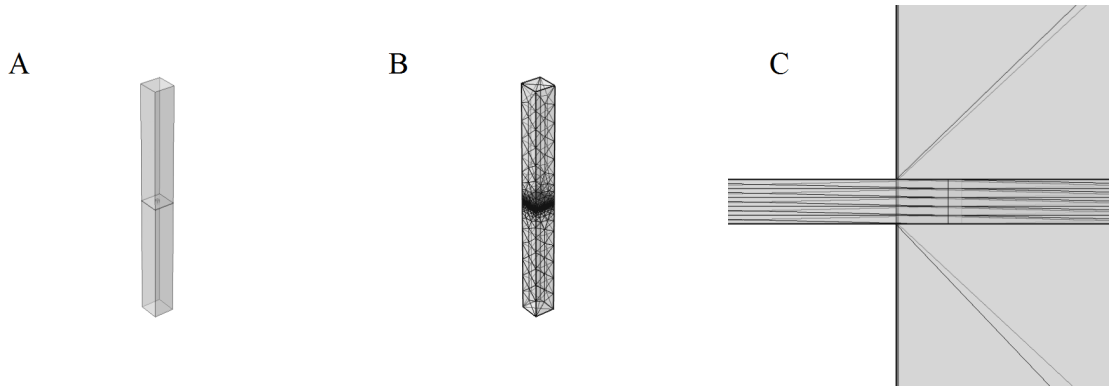

Figure 3.1: Unit cell in a waveguide FEM model A.) geometry, B.) mesh, and C.) closeup of swept mesh

A mesh of 69,178 elements, shown in Figure 3.1 (B), is used to ensure at least four elements per wavelength in the air domain. To adequately resolve membrane deflection, a swept mesh is used across the thin membrane domain to ensure that there are at least five elements across the membrane thickness. The swept mesh takes a two-dimensional mesh on the surface of the membrane and extrudes the polygons, in this case triangles, to create prismatic polyhedrons. Elements in the membrane have a maximum side length of 0.8 millimeters. Figure 3.1 (C) shows a closeup cross-section of the swept mesh at the interface between the membrane and the attached mass.

The sound pressure transmission coefficient, t_p, for the unit cell in a waveguide is the ratio of transmitted to incident pressure, since the cross sectional area and

fluid impedance are the same on both sides. The transmitted and incident pressures are found by integrating over the end and beginning of the waveguide, respectively. The TL is given by $-20\log_{10}(t_p)$.

Figure 3.2 shows the results of the impedance-mobility model (solid) and FEM (dashed). In general, there is good agreement between the two methods. The TL peak at 360 Hz and two resonance frequencies at 230 Hz and 3760 Hz, respectively, are accurately captured with the impedance-mobility model within 2%. The magnitude of the TL is also in good agreement with the FEM model, with a notable exception near the TL peak and resonance frequencies where a lack of damping in the FEM model is evident. This result is consistent with the difference between FEM and TL measured in a plane wave tube by Naify et al. [2011b]. The impedance-mobility model of a unit cell in waveguide accurately predicts TL for the baseline configuration.

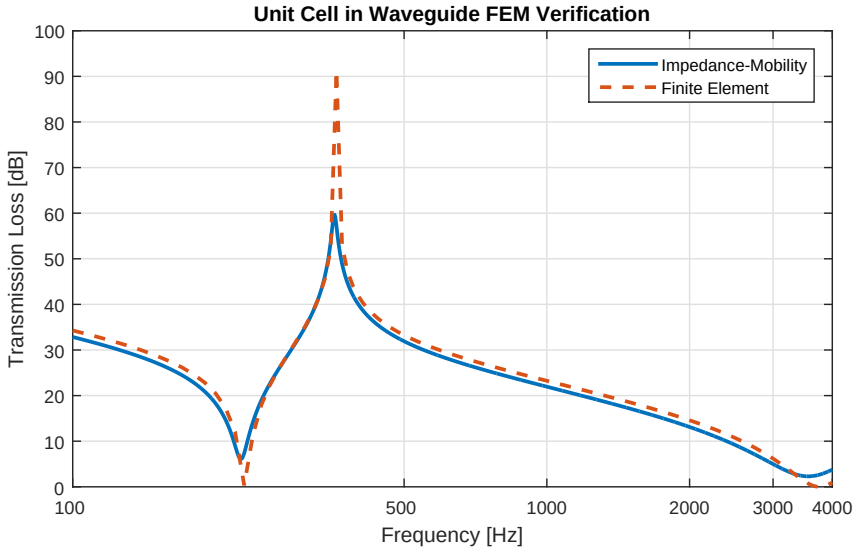

Figure 3.2: FEM verification of a single unit cell in a waveguide. Impedance-mobility (solid), FEM (dashed)

3.1.2 Unit Cell in a Baffle

A second FEM model is used to verify the accuracy of the impedance-mobility model of a single unit cell set in a rigid baffle. Due to computational limitations, a two-dimensional shell model is used for the rigid baffle, membrane, and mass. This reduces the three-dimensional solid structures to two-dimensional surfaces, and equivalent parameters are automatically computed. The appropriateness of using a two-dimensional shell to represent a three-dimensional structure is analyzed for the simple case of a single unit cell in a waveguide in Section 3.2.1.

A rectangular waveguide is used on the incident side of the unit cell to limit the excitation to normally incident plane waves. This ensures that there are no spurious reflections of the plane wave off of the baffle or the air domain boundary. On the transmitted side, a hemispherical air domain is used with a spherical radiation boundary condition. This approximates sound radiating from the unit cell to infinity with no reflections. The model geometry is shown in Figure 3.3 (A).

A two-dimensional mesh is used on the surface of the unit cell and baffle and converted to match the tetrahedral mesh in the air domain, which is shown in Figure 3.3 (B). A total of 68,939 mesh elements is used to maintain at least four elements per wavelength at 4000 Hz.

Figure 3.4 shows a comparison of the results of the TL modeled in FEM and using the impedance-mobility approach. The results are in good agreement, accurately capturing the first and second resonance frequencies at 226 Hz and 3552 Hz, respectively, within 3%. There is a small discrepancy in the magnitude of the

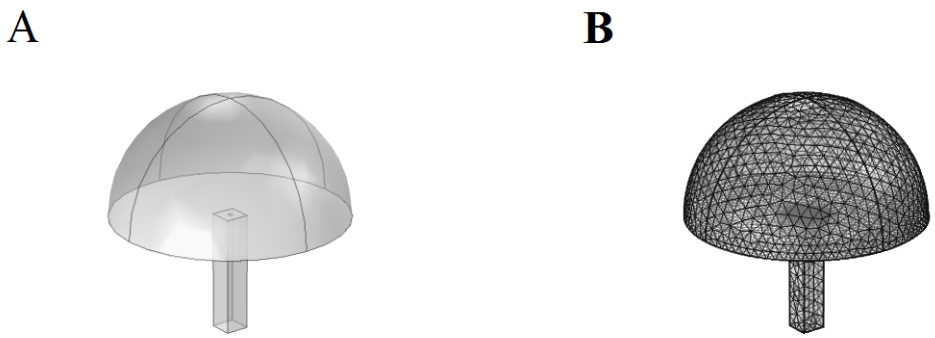

Figure 3.3: Baffled unit cell FEM model A.) geometry, and B.) mesh.

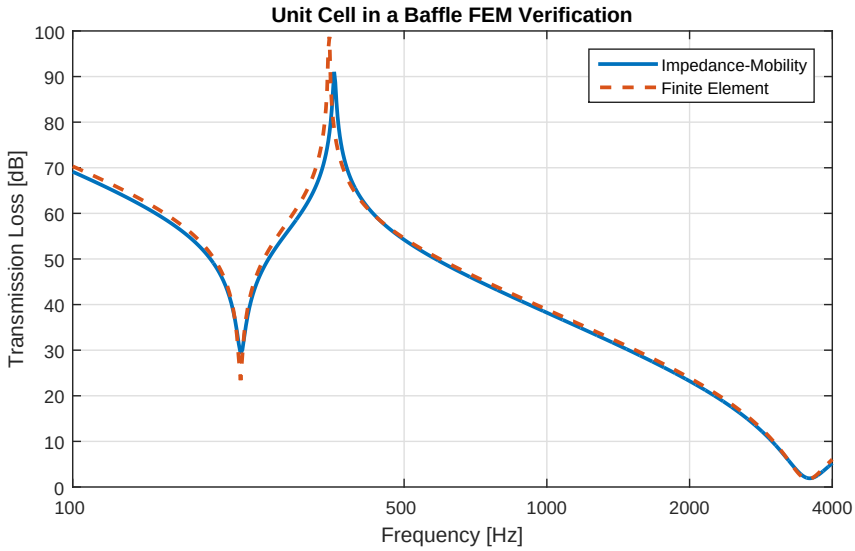

Figure 3.4: FEM verification of a single unit cell in a baffle. Impedance-mobility (solid), FEM (dashed)

first resonance and TL peak that is explained by a lack of damping in the FEM model.

3.1.3 2×1 Array in a Baffle

To extend the model introduced in the previous section to analyze a system consisting of an array of unit cells in a baffle, a second unit cell is placed adjacent to the first sharing a common boundary in the FEM model as shown in Figure 3.5 (A). The meshes in the air domain and membranes are identical to those used for the single unit cell in a baffle. A total of 100,331 elements is used.

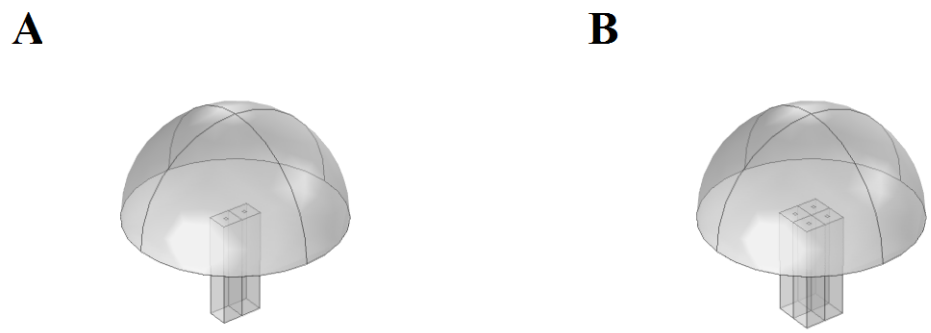

Figure 3.5: FEM geometry of baffled multi-cell arrays A.) 2×1 B.) 2×2

Figure 3.6 compares the TL from the impedance-mobility model with mutual coupling between the two unit cells against FEM results. The impedance-mobility model accurately predicts the TL of the 2×1 array below the second resonance frequency, with less than 2% relative error in the TL peak at 350 Hz. However, there is a discrepancy of about 9% at the second resonance at 3520 Hz where the wavelength of sound in air is on the order of the dimensions of the array.

Due to the complexity of formulating an impedance-mobility model that

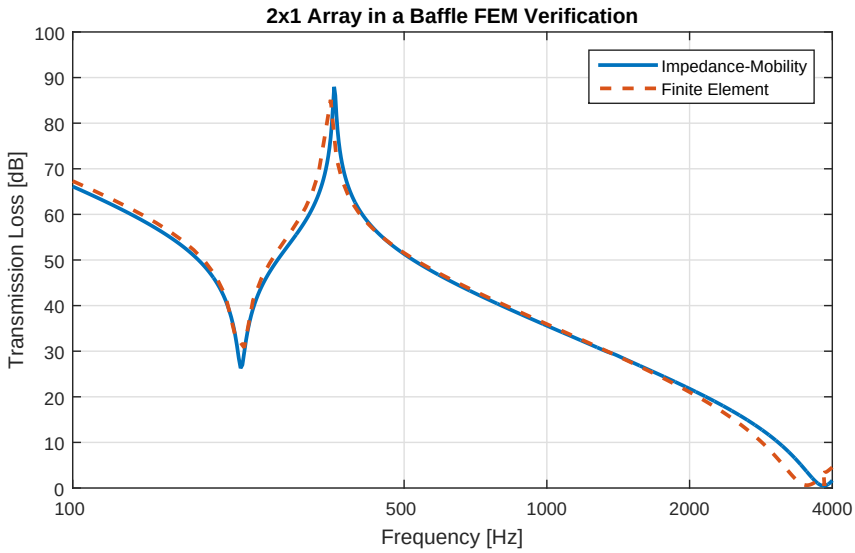

Figure 3.6: FEM verification of a 2×1 array in a baffle. Impedance-mobility (solid), FEM (dashed)

incorporates mutual coupling between an arbitrary number of unit cells, it is also desirable to verify the accuracy of the negligible coupling model formulated in Section 2.2.2. Figure 3.7 shows the results of the impedance-mobility model with negligible coupling compared to FEM. There is very good agreement between the models with less than 2% relative error for each of the first and second resonances and TL peak frequency at 230 Hz, 350 Hz, and 3530 Hz, respectively. This indicates that mutual coupling of vibratory motion between unit cells does not significantly contribute to the radiated sound power.

3.1.4 2×2 Array in a Baffle

Similarly, the model can be expanded to study a 2×2 array of unit cells in a baffle using the geometry shown in Figure 3.5 (B). Comparing the negligible coupling impedance-mobility model to the FEM results in Figure 3.8 again shows excellent

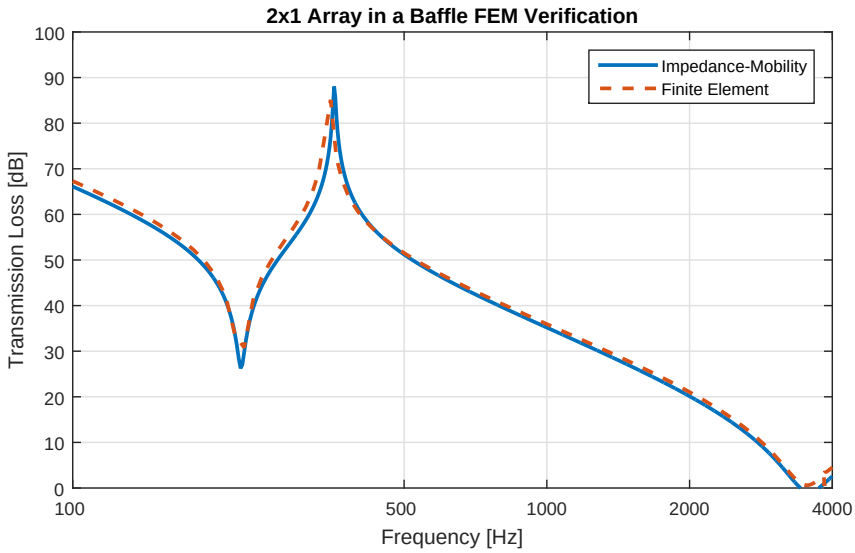

Figure 3.7: FEM verification of a 2×1 array in a baffle. Impedance-mobility with negligible coupling assumption (solid), FEM (dashed)

agreement below the second resonance frequency.

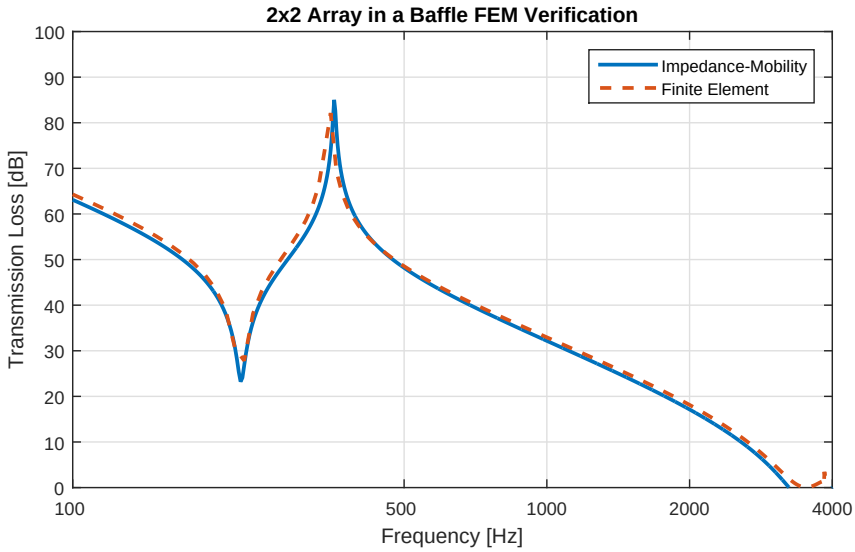

Figure 3.8: FEM verification of a 2×2 array in a baffle using negligible coupling model. Impedance-mobility (solid), FEM (dashed)

The results indicate that the negligible coupling impedance-mobility model maintains accuracy while increasing the number of unit cells in the array. There is less than 2% difference in the TL peak and resonance frequencies at 350 Hz, 230 Hz,

and 3520 Hz, respectively. The vastly simpler derivation of the negligible coupling impedance-mobility model allows expansion to multi-cellular arrays to be explored further in Chapter 5.

3.1.5 Double Layer in a Waveguide

A configuration of two unit cells stacked in series in a waveguide is modeled by introducing a second unit cell to the FEM model described in Section 3.1.1 as shown in Figure 3.9 (A). The second unit cell is placed 8 millimeters above the first so that each unit cell has enough space to freely vibrate. For computational efficiency an acoustic-shell interaction model is used that approximates the membranes as two-dimensional surfaces. The mesh consists of 60,892 elements and is shown in Figure 3.9 (B).

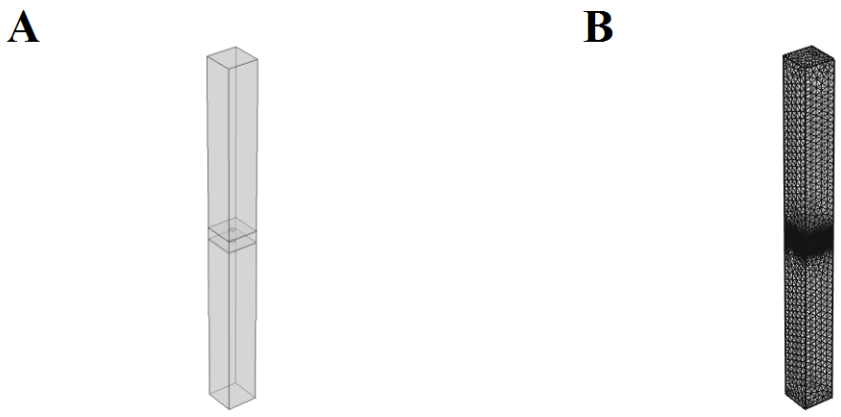

Figure 3.9: Double layer in a waveguide FEM A.) geometry and B.) mesh.

The results in Figure 3.10 show very good agreement of the TL predicted with

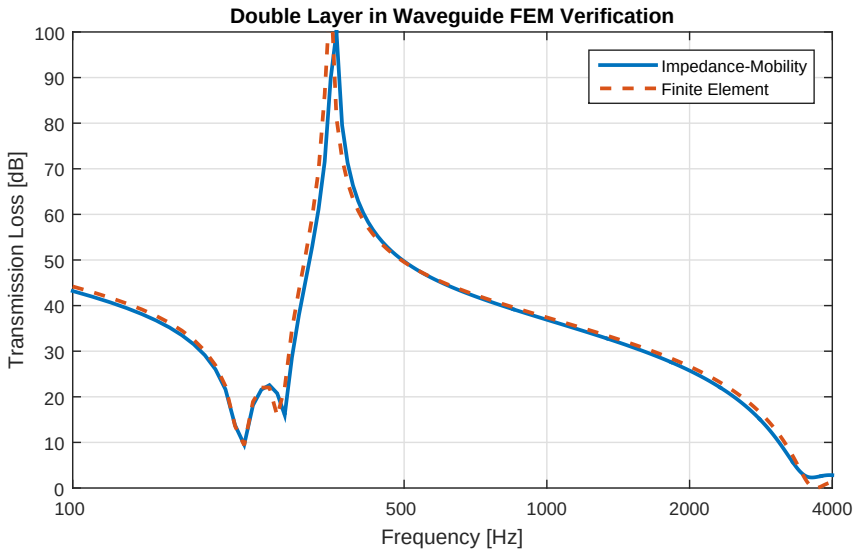

Figure 3.10: FEM verification of a double unit cell in a waveguide. Impedance-mobility (solid), FEM (dashed)

FEM and the impedance-mobility approach. The absolute value of the difference in TL away from the resonances and TL peak is generally less than 1 dB. The uncertainty of the resonance and TL peak frequencies is less than 3% as shown on the plot, but cannot be adequately explored due to the low sampling frequency of the FEM model.

3.2 Validation of Assumptions

Three important assumptions that are made in the impedance-mobility models derived in Chapter 2 are tested in this section. The first assumption is that the attached mass does not prohibit bending of the membrane segment on which it lies. The second assumption is that the rotary inertia of the attached mass does not affect the vibration of the membrane. Effectively, the impedance-mobility model assumes a uniformly thick membrane with discontinuous surface density. These

assumptions are tested using FEM models that manipulate the geometry of the unit cells to match the constraints of the impedance-mobility models. The third assumption is that in an array of multiple unit cells, the mutual pressure between unit cells acts evenly across the surface of each unit cell, and the unit cell behaves as a piston-like radiator. This is tested by examining the surface pressure on the array, and the deflection of the unit cells. The degree to which each of the assumptions is valid is investigated.

3.2.1 Attached Mass Bending Stiffness

It is obvious that a material used for the attached mass is likely to have a much higher bending stiffness than that of the membrane since denser materials are also likely to be stiffer. An assumption made in the impedance mobility model is that the difference in stiffnesses will have a negligible impact on the unit cell vibration and transmission loss. In fact, a discontinuity in bending stiffness would be a violation of the fundamental assumption in Equation (2.3). This is evident in Equation (2.26) where the flexural rigidity, D, which is a measure of bending stiffness, is multiplied by the square of the divergence of the gradient of the membrane deflection.

The bending stiffness of the attached mass is proportional to the cube of the mass thickness, as seen in Equation (2.24). It is evident that the flexural rigidity of the mass depicted in Figure 3.11 (A), will be higher than that depicted in Figure 3.11 (B) or (C) due its increased thickness. To investigate the effects of mass bending stiffness, a FEM model with simplified geometry consisting of an attached

mass that is equal in thickness to that of the membrane is used. This configuration exactly replicates the impedance-mobility model formulated in Chapter 2.

Ideally, in addition to reducing the thickness of the attached mass, the Young's modulus and Poisson's ratio would also be modified to match those of the membrane. However, in doing so the attached mass will deform due to the applied tension on the membrane. The impedance-mobility model assumes that the increased surface density is confined in the specified mass location, thus the effect of mass bending stiffness cannot be thoroughly studied using FEM.

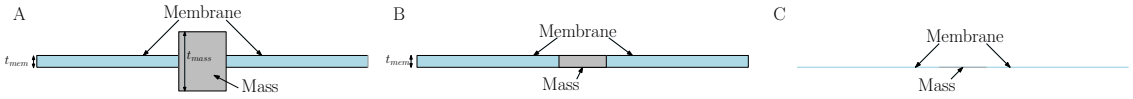

Figure 3.11: Cross-sections of A.) a 3D unit cell, B.) a simplified 3D unit cell and, C.) an idealized 2D shell unit cell for use in FEM studies on the effect of bending stiffness

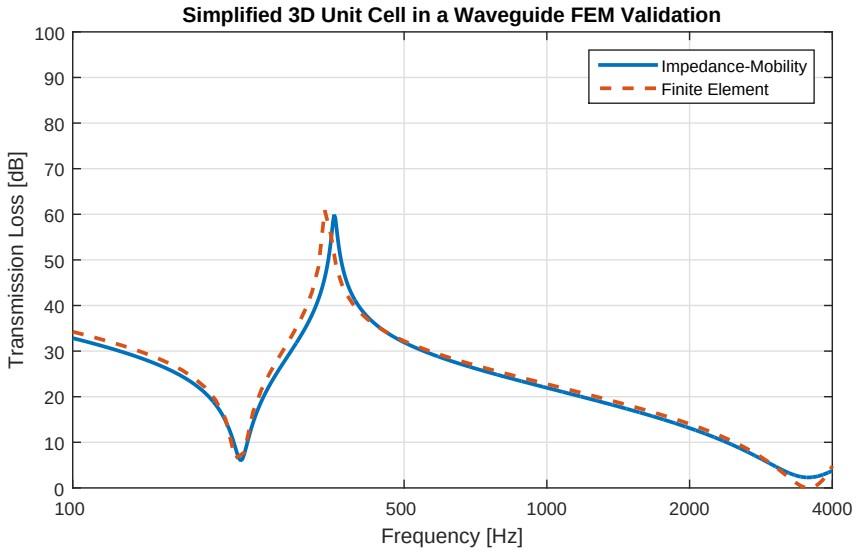

Figure 3.12: FEM verification of a simplified 3D unit cell in a waveguide. Impedance-mobility (solid), FEM (dashed)

Figure 3.12 shows the comparison of a simplified FEM model with reduced

thickness of the attached mass, as shown in Figure 3.11 (B), to the impedance-mobility model. There is good agreement between the two models with less than 1% relative error at the resonances at 220 Hz and 3570 Hz and less than 5% error at the TL peak frequency 340 Hz. By comparing Figure 3.2 to Figure 3.12, it is evident that as the assumptions in the FEM model are manipulated to match those in the impedance-mobility model the level of agreement increases. By again referring to Figure 3.2, it is clear that while the bending stiffness of the attached mass (and its thickness) does affect the TL of the unit cell to a small degree, the impedance-mobility model is still accurate despite the assumption that the effects are completely negligible.

Additionally, the thickness of the unit cell can be neglected entirely in the geometry of the FEM model (see Figure 3.11 (C)). By treating the unit cell as a two-dimensional shell, the appropriateness of neglecting the thickness of the membrane and attached mass in the impedance-mobility model can be further validated.

For the shell model, a triangular mesh was used on the surface of the membrane and attached mass and converted to match the tetrahedral elements in the air domain. This resulted in 49,506 elements and 96,093 degrees of freedom.

Figure 3.13 shows the results of the shell FEM model compared to the impedance-mobility approach. The TL results are nearly identical, with only minor discrepancies of 3 dB in magnitude and 4% relative error at the second resonance at 3690 Hz and less than 5 dB in magnitude and less than 1% at the TL peak frequency of 350 Hz.

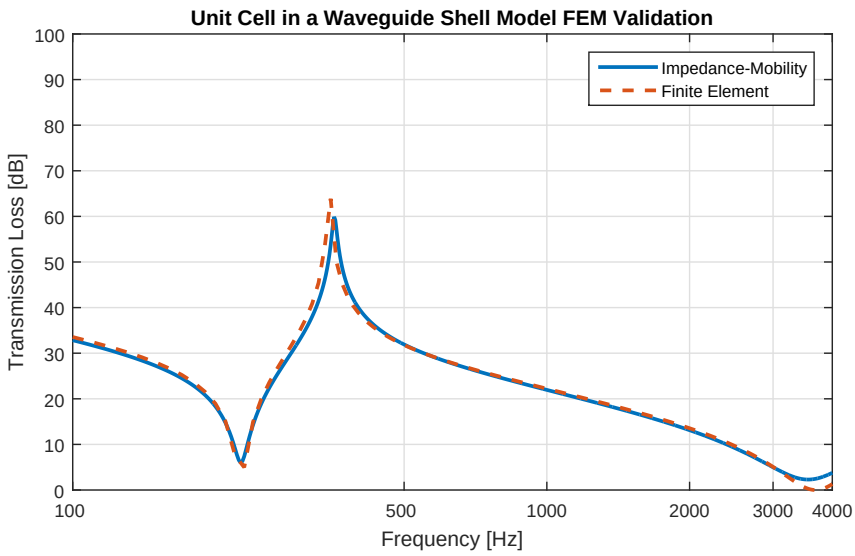

Figure 3.13: FEM shell model verification of a single unit cell in a waveguide. Impedance-mobility (solid), FEM (dashed)

By comparing the TL from FEM models with varying attached mass thicknesses, the assumption made in the impedance-mobility model that the bending stiffness of the attached mass is negligible is tested. In general, the impedance-mobility model accurately predicts TL for unit cells with non-negligible attached mass stiffness.

3.2.2 Attached Mass Rotary Inertia

For attached masses that are relatively thin, the assumption that the rotary inertia of the mass is negligible may be appropriate. However as mass size increases, especially in the z direction, the impedance-mobility model may lose accuracy in prediction. To study the influence of attached mass rotary inertia, a FEM model is used where the thickness of the attached mass is varied, while maintaining the same mass magnitude. Additionally, the location of the mass is varied to increase any

potential effects of attached mass rotation. Since the unit cell is excited by a normally-incident plane wave, only symmetric modes are excited. This will result in purely translational motion in the axial direction of a centrally-located attached mass. An eccentric mass location produces the desired rotational motion that will allow the effects of rotational inertia to be investigated, and the assumption in the impedance-mobility model to be validated.

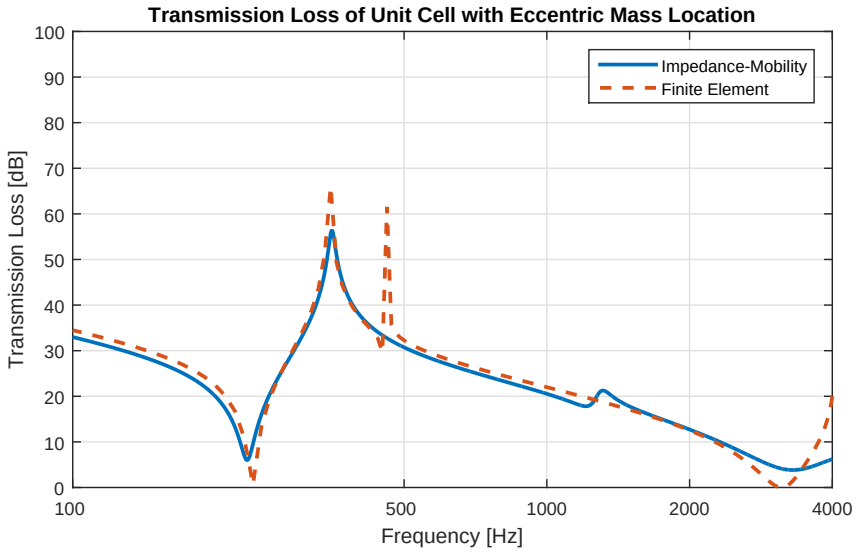

Figure 3.14: Comparison of impedance-mobility (solid) and FEM (dashed) transmission loss of a unit cell with an eccentric mass location

Figure 3.14 shows the results of the FEM model with an eccentrically placed mass, the baseline configuration with $x_0 = 6$ mm as defined in Figure 2.1, compared to the impedance-mobility approach. At an eccentric location, the mass will undergo non-uniform displacement across its area, resulting in out-of-plane mass rotation. The effect of the rotary inertia of the attached mass is seen particularly at 460 Hz, where there is an additional TL peak. At this frequency, the mass undergoes maximum rotation, as shown in Figure 3.15. The energy required to

rotate the attached mass is not radiated downstream of the unit cell, and thus a peak in the TL curve appears.

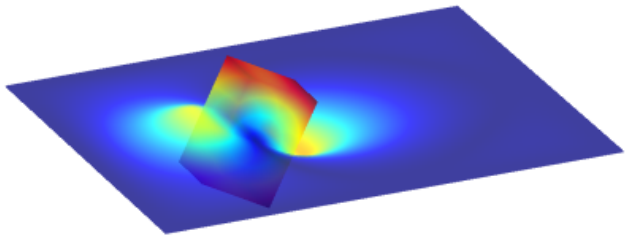

Figure 3.15: Example of rotary inertia of the attached mass at 460 Hz from FEM model

With the exception of the additional TL peak, the impedance-mobility model performs well compared to FEM. The relative error is less than 6% at the resonance at 3120 Hz, and less than 1% at the TL peak at 350 Hz. There is also some discrepancy in the TL at the high end of the frequency range of less than 15 dB near 4000 Hz.

Since the impedance-mobility model treats the attached mass as a discontinuity in the surface density of the unit cell, the effects of attached mass rotation are not adequately captured. This will lead to under-prediction of the TL at the frequencies that excite rotation of the attached mass.

By decreasing the thickness of the attached mass, the effect of rotary inertia can be studied further. A FEM model with eccentric mass location and thickness equal to that of the membrane is used. The results shown in Figure 3.16 indicate that the frequency at which the mass rotation produces a TL peak increases, while decreasing the magnitude of the peak. The deflection of the unit cell at the TL peak frequency is shown in Figure 3.17. The resonance occurs when the mass rotates on

its major axis in the plane and the membrane remains stationary.

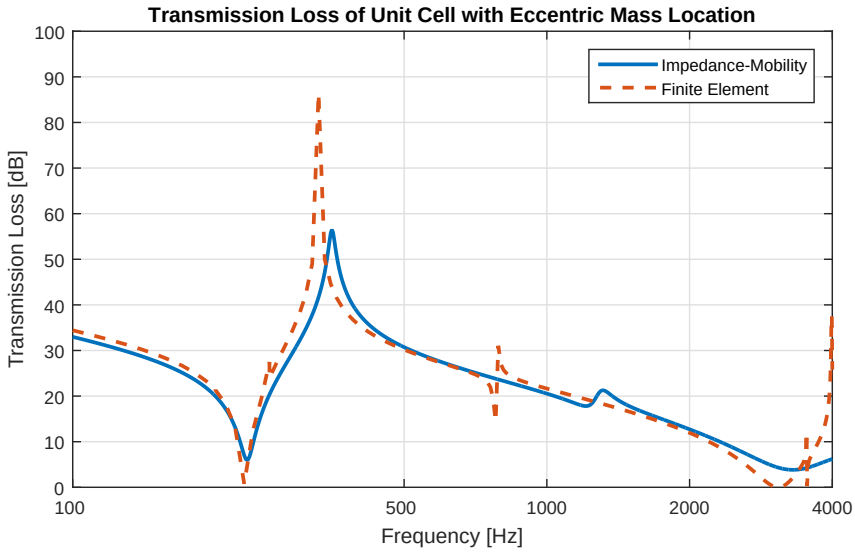

Figure 3.16: Comparison of impedance-mobility (solid) and FEM (dashed) transmission loss of a unit cell with a reduced thickness eccentrically placed attached mass

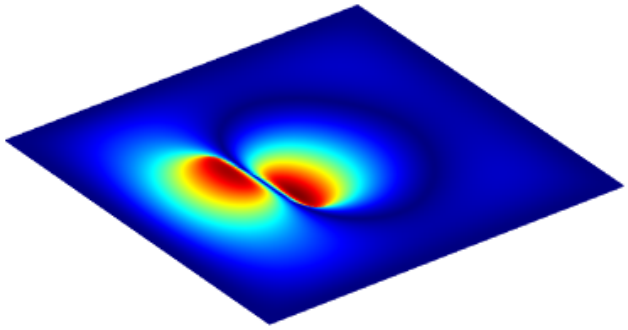

Figure 3.17: Example of rotary inertia of the attached mass at 790 Hz

3.2.3 Coupling Between Unit cells in an Array

In Chapter 2 the formulation of an impedance-mobility model for an array of unit cells in a baffle assumes that the pressure on one unit cell due to another is uniform over its area. This assumption, however, does not hold for values of ka that are not much less than unity (i.e. at high frequencies or large unit cell dimensions).

Figure 3.18 shows the pressure on the surface of two adjacent unit cells in a rigid baffle at 3500 Hz. The pressure distribution on the unit cells is not uniform, with higher pressure toward the center of the array. This causes asymmetric vibration of the unit cells as shown in Figure 3.19.

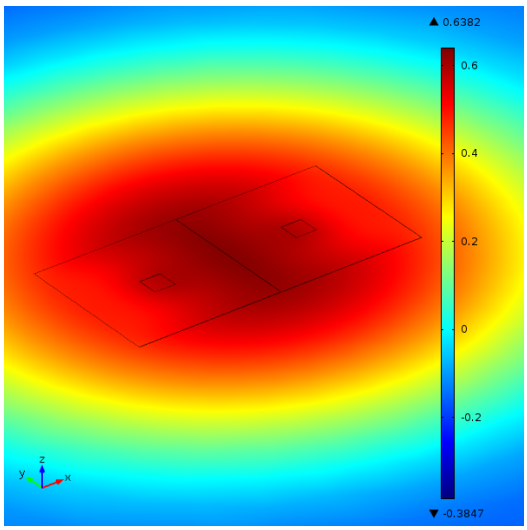

Figure 3.18: Surface pressure of a 2×1 array of unit cells in a baffle

This result agrees with Naify et al. [2011b], who pointed out that pressure coupling of adjacent unit cells causes an increase in the effective stiffness of the membranes. As a result, the second resonance frequency increases. This suggests that the impedance-mobility model of multi-cell arrays is only accurate below approximately 2000 Hz.

3.3 Generalization to Other Unit Cell Geometries

The impedance-mobility formulation described in Chapter 2 is valid for unit cells with rectangular geometry. It may arise, in some situations, that it is advantageous to fabricate noise barriers of membrane-type acoustic metamaterials that do not

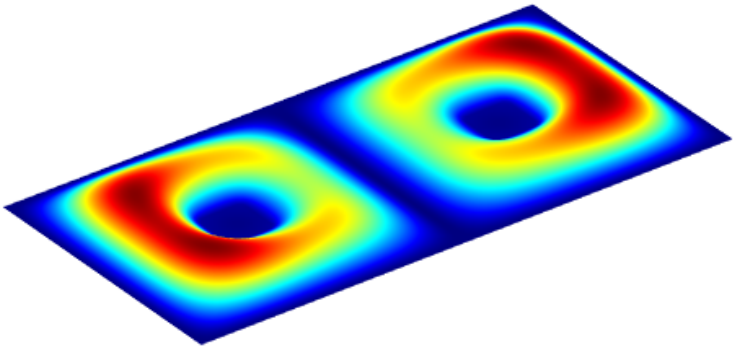

Figure 3.19: Displacement of a 2×1 array of unit cells in a baffle

have rectangular unit cells. For instance, drilling circular holes into a rigid matrix may be more efficient than cutting squares. This section presents the comparison of the transmission loss of membrane-type acoustic metamaterials with circular, hexagonal, and triangular unit cell shapes using FEM. This comparison sheds light on the degree to which the impedance-mobility models can be used to design systems of varying unit cell shapes.

3.3.1 Circular Unit cell

A FEM model consisting of a cylindrical waveguide with a circular unit cell is used to test the ability of the impedance-mobility to predict the TL of a circular, rather than rectangular, unit cell. A three-dimensional acoustic-shell interaction model is used, which approximates the unit cell as a two-dimensional surface.

By setting the radius of the circular unit cell such that the areas of both unit cells are equal, $r_{mem} = \sqrt{L_x L_y/\pi}$, the TL of a circular unit cell can reasonably be approximated using the impedance-mobility approach. A comparison of TLs obtained by FEM and the impedance-mobility approach is shown in Figure 3.20.

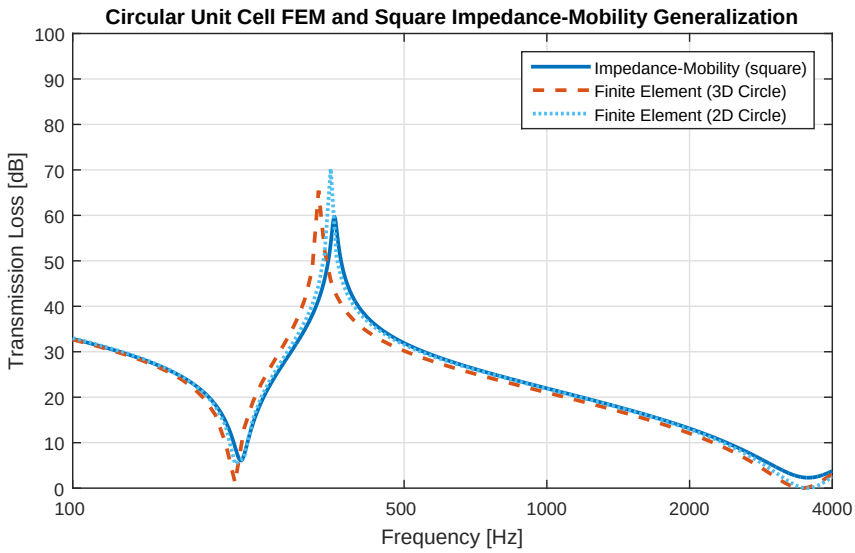

Figure 3.20: Comparison of TL from impedance-mobility model of a square unit cell (solid) and FEM of a 3D circular unit cell (dashed) and 2D circular unit cell (dotted)

There is a less than 8% relative error in the frequency at the TL peak at 330 Hz, and approximately 3% error in the resonances at 220 Hz and 3450 Hz.

While using models that fully account for three-dimensional geometry is most accurate, modeling structures with axial symmetry, such as a circular membrane carrying a centrally-located cylindrical mass, is most efficiently accomplished in FEM using a two-dimensional axial-symmetric model. This type of model takes a 2D geometry and revolves the solution about an axis of symmetry. Figure 3.21 shows the 2D geometry used.

The results in Figure 3.20 show good agreement between the square impedance-mobility model (solid line) and 2D axial-symmetric FEM model of a circular unit cell of equal area (dotted line). There is less than 2% error at the TL peak frequency of 350 Hz, and less than 1% error at the two resonances at 220 Hz and 3540 Hz. Since the FEM model used is axi-symmetric, the attached mass is

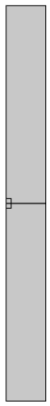

Figure 3.21: Geometry of 2D axial-symmetric FEM model

constrained to be centrally located and can only move along the axis, without rotation. This results in greater agreement when compared against the impedance-mobility model because of its implicit assumption that no mass rotation occurs.

As shown in Section 3.2.2, an eccentric mass location can reduce the accuracy of the impedance-mobility models due to rotary inertia of the attached mass. The appropriateness of generalizing the impedance-mobility model of a rectangular unit cell to a circular unit cell is also affected by mass location. To study this effect, the two models are compared with the attached mass located a distance l_y from the center of the unit cell.

Like with the rectangular unit cell, an eccentric mass location on a circular unit cell produces an additional resonance and TL peak. This is seen at 410 Hz in Figure 3.22. The corresponding vibration pattern is shown in Figure 3.23. The resonance occurs when the attached mass rotates out-of-plane centered between the

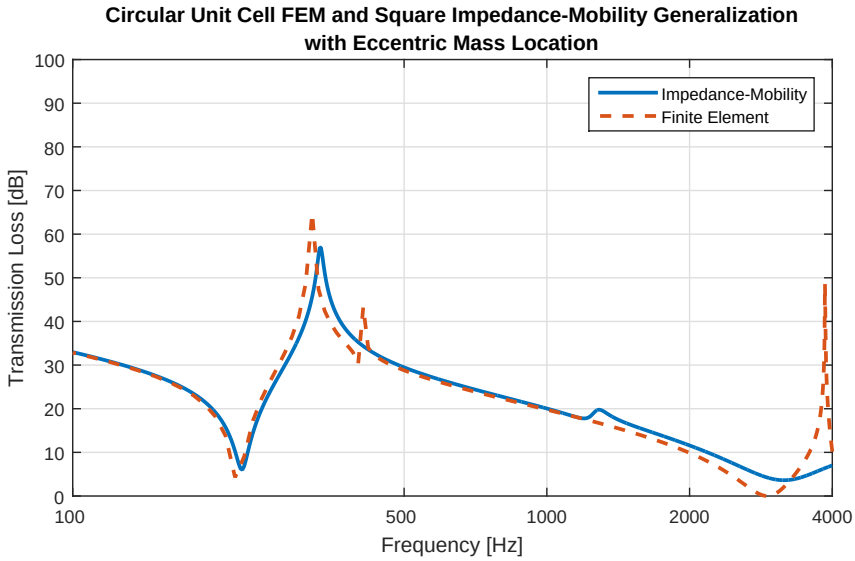

Figure 3.22: Comparison of TL from impedance-mobility of a square unit cell (solid) and FEM model of a circular unit cell (dashed) with an eccentric mass location

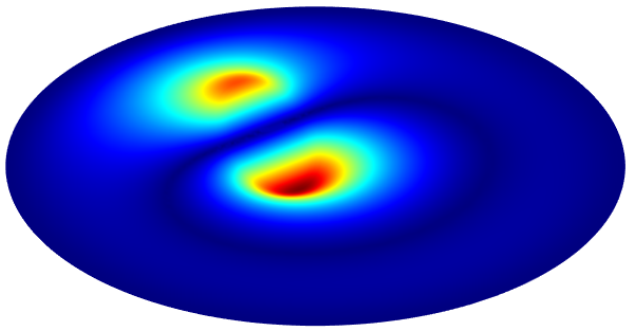

Figure 3.23: Deflection of circular unit cell at 410 Hz

two bright spots in the figure, and the rest of the membrane remains stationary.

3.3.2 Hexagonal Unit Cell

Hexagonal unit cells are of particular interest since they are widely used in "honeycomb" structures [Lu et al. 2016; Naify et al. 2011c]. Since regular hexagons can be arranged in an array with no gaps, they make ideal candidates for unit cells of membrane-type acoustic metamaterial structures.

To model the waveguide, a hexagonal prism is created by extruding a hexagon into three-dimensions. A two-dimensional shell structure models the membrane and attached mass. To maintain an equal unit cell surface area in comparing the hexagon to a square, the hexagon side length is calculated as

$$a = \sqrt{\frac{2L_x L_y}{3\sqrt{3}}}. \tag{3.1}$$

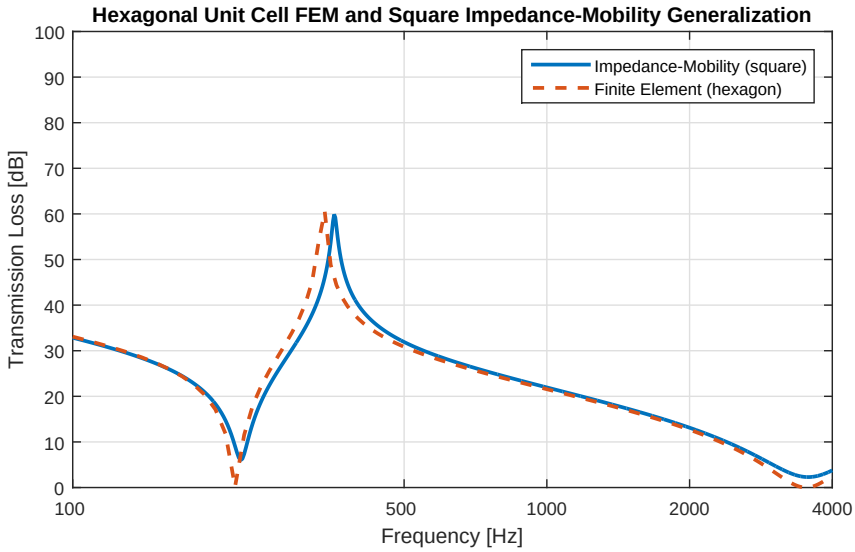

Figure 3.24: Comparison of TL from impedance-mobility of a square unit cell (solid) and FEM model of a hexagonal unit cell (dashed)

The results of the FEM model of a hexagonal unit cell in a waveguide are shown in Figure 3.24. There is good agreement between TL obtained using the impedance-mobility approach for a square unit cell of equal area and with FEM. There is some discrepancy in the frequencies of the first resonance at 220 Hz and TL peak at 340 Hz with relative errors of less than 3% and 5%, respectively. The second resonance at 3510 Hz is more accurately captured with relative error of approximately 1%.

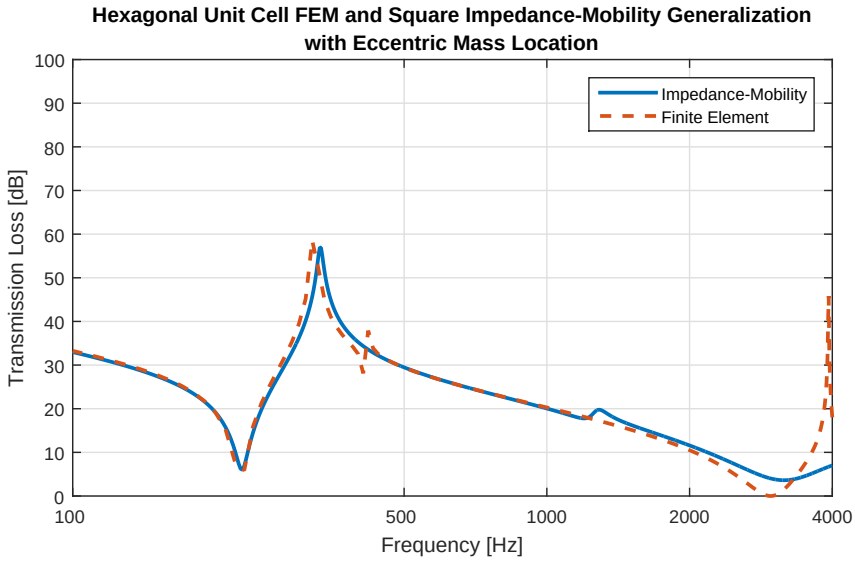

Figure 3.25: Comparison of TL from impedance-mobility of a square unit cell (solid) and FEM model of a hexagonal unit cell (dashed) with an eccentric mass location

Figure 3.25 shows the effect of an eccentric mass location on the hexagonal unit cell, compared to the TL of a square unit cell. The mass is located 3 mm off-center toward the an edge of the hexagon so that it is affected by the symmetric vibration modes of the membrane. There is an additional resonance and TL peak at approximately 420 Hz due to the rotary inertia of the attached mass, as depicted in Figure 3.26. At this frequency the attached mass rotates independently of the membrane. The unit cell as a whole does not couple to the surrounding fluid well since there is no net volume displacement at the 420 Hz resonance.

3.3.3 Triangular Unit Cell

As the number of sides of a regular polygon increases, the shape approaches a circle. Having established that the impedance-mobility model of a square unit cell approximates the TL of a circular unit cell, it follows that it will also approximate

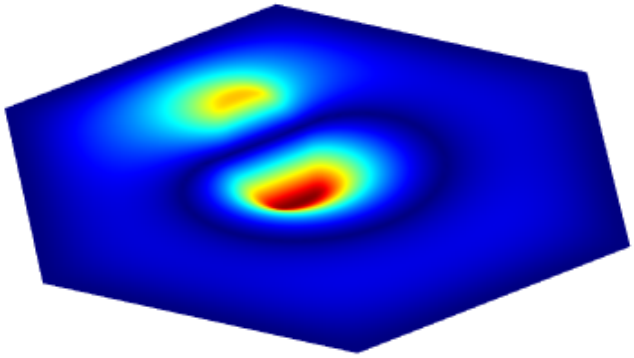

Figure 3.26: Deflection of hexagonal unit cell at 420 Hz

regular polygons with four or more sides. This is proven in the previous section with the study of a hexagonal unit cell. To thoroughly investigate the effect of unit cell shape, decreasing the number of sides to three is also necessary. An equilateral triangular unit cell is modeled using an acoustic-shell interaction FEM model to complete the study of unit cell shape and its effect on TL.

The side length of an equilateral triangle necessary to maintain the same area as the square unit cell is given by

$$a = \sqrt{\frac{4L_x L_y}{\sqrt{3}}}. \tag{3.2}$$

The model of a waveguide is created by extruding an equilateral triangle into the z-direction. The same initial and boundary conditions as the previous cases of rectangular, circular, and hexagonal geometries are used for the triangular configuration.

The results plotted in Figure 3.27 show moderate agreement between the two models. The impedance-mobility model underestimates the TL by approximately 3 dB over the frequency range of interest, with the exception of between the first

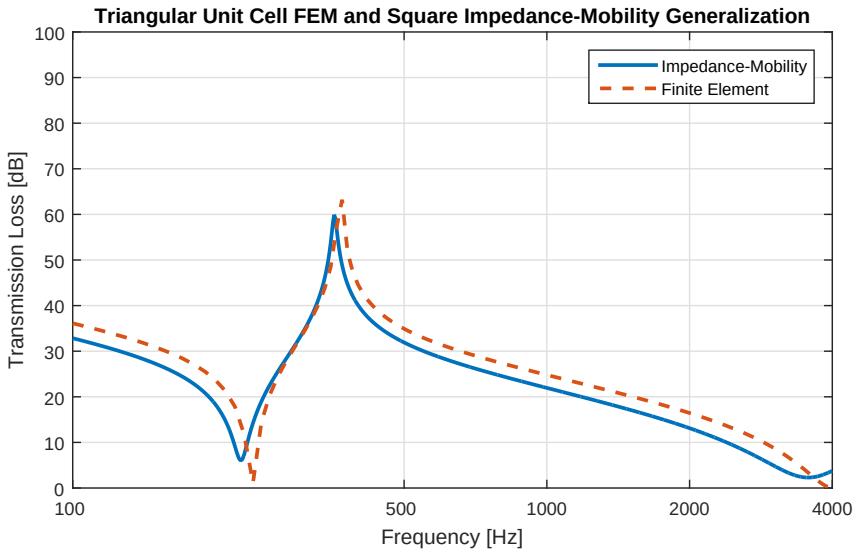

Figure 3.27: Comparison of TL from impedance-mobility of a square unit cell (solid) and FEM model of a triangular unit cell (dashed)

resonance and TL peak. The TL peak at 370 Hz differs by less than 4% between the models. The first and second resonance frequencies have relative errors of approximately 6% at 240 Hz and 11% at 4000 Hz, respectively.

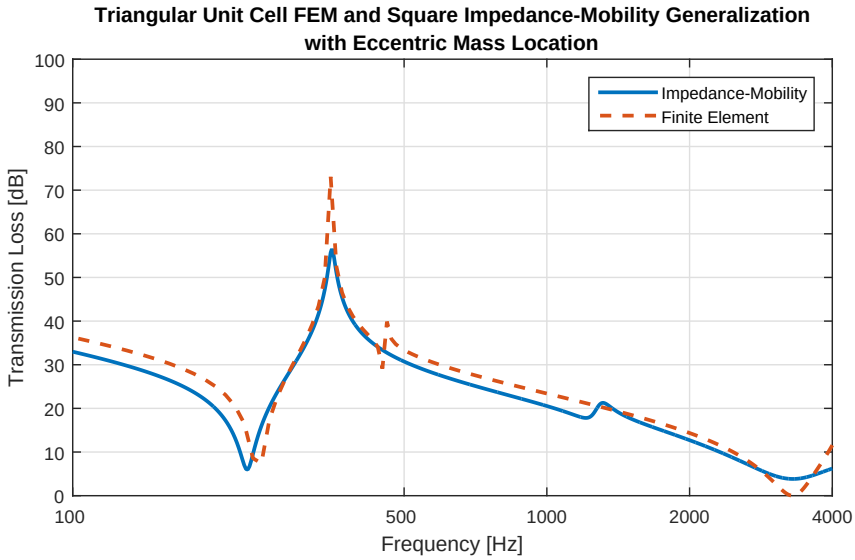

Figure 3.28: Comparison of TL from impedance-mobility of a square unit cell (solid) and FEM model of a triangular unit cell (dashed) with an eccentric mass location

An attached mass located at 3 mm from the center of the triangular unit cell undergoes out-of-plane rotation due to the symmetric vibration modes of the membrane. Figure 3.28 compares the TL of the triangular unit cell using FEM to a square unit cell of equal area with the same eccentric attached mass location. Again, there is a resonance at 460 Hz where most of the unit cell is stationary and the attached mass rotates independently as shown in Figure 3.29.

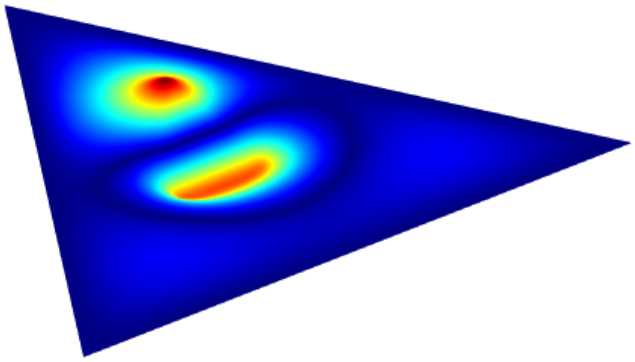

Figure 3.29: Deflection of triangular unit cell at 460 Hz

3.3.4 Remarks on Generalization to Other Unit Cell Geometries

The impedance-mobility approach used in Chapter 2 models a unit cell of a membrane-type acoustic metamaterial as a rectangular membrane carrying a rectangular attached mass. In general, there is good agreement between the models, regardless of unit cell shape, for centrally-located attached masses. Figure 3.30 shows the FEM results of four different unit cell shapes with centrally-located attached masses of the same shape.

For engineering purposes, a model is considered very accurate if the predicted

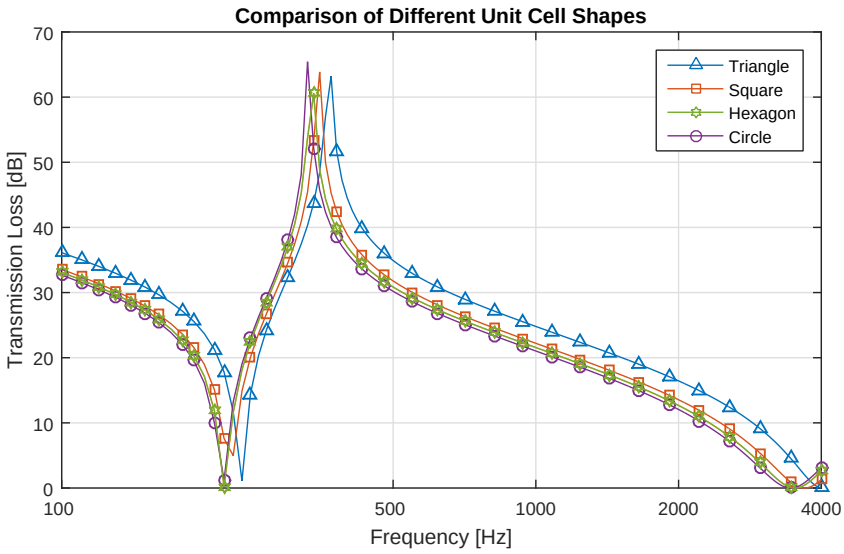

Figure 3.30: Comparison of TLs for different shaped unit cells using FEM

TL of a structure agrees with measurements to within one or two decibels. Thus, the discrepancy caused by the shape of the unit cell is within the margin of error, and is not likely to be a significant inhibitor to the scale-up of membrane-type acoustic metamaterial noise barriers.

3.4 Computational Efficiency

The main benefit of the impedance-mobility approach is that it is computationally efficient while maintaining accuracy. Other common methods, such as FEM, have serious computational limitations that prohibit the application of iterative schemes for optimization. Since FEM is the most common method used to study membrane-type acoustic metamaterials, it is used as a basis for comparison for the currently proposed impedance-mobility method.

Table B.8 shows the computation times for the FEM models used in Chapter 3.

For each model a frequency range of 100 Hz to 4000 Hz is used with a spacing of 10 Hz for a total of 391 frequency points. The fastest run time of 1 minute and 39 seconds is achieved with a 2D axi-symmetric model which only considers a circular unit cell with a centrally-located cylindrical attached mass. In some cases this model can accurately estimate of TL of a square unit cell, as shown in Figure 3.20. The slowest run time of 17 hours and 5 minutes is experienced with the most realistic model which considers the finite thickness of the membrane and attached mass in three dimensions.

The computational efficiency of the impedance-mobility approach arises from its compact matrix formulation, and the opportunistic application of simply-supported boundary conditions and rectangular geometry. Those choices enable the integrals formulated in Chapter 2 to be evaluated explicitly and hard-coded so that no numerical integration is needed within the program. Appendix E shows the evaluation of the integrals.

The impedance-mobility model running on the same machine as the FEM models using the same frequency range and spacing executes in less than 0.1 seconds. This corresponds to an increase in speed of nearly 100,000% over the fastest FEM model.

The exceptional computational efficiency of the impedance-mobility approach for membrane type acoustic metamaterials enables the use of iterative optimization schemes such as genetic algorithms. Additionally, the proposed model is well-suited to implementation in user-friendly tools for design. A graphical user interface (GUI), is used as a front-end to the impedance-mobility model formulated in

Chapter 2 that allows a user to alter the design parameters of a unit cell, and at the click of a button view its TL response.

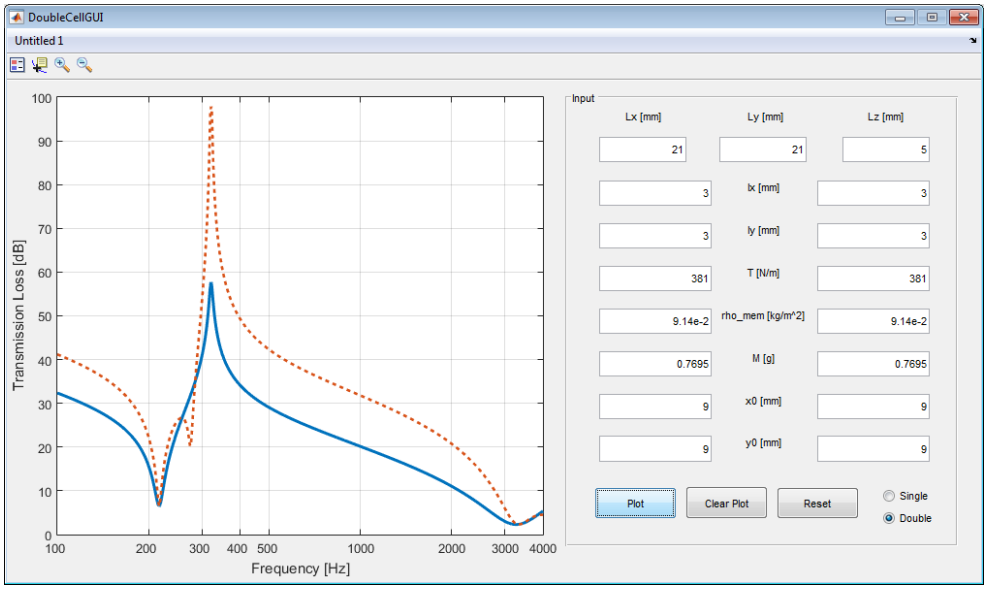

Figure 3.31: Graphical user interface for single and double layer unit cells in a waveguide

Figure 3.31 shows the GUI created in MathWorks MATLAB 2014b. The GUI allows the user to select between a single unit cell and a double layer of unit cells that are defined independently. In addition to being user-friendly, the GUI is also portable since it is compiled as an executable file. The file requires MATLAB Runtime to operate, which is freely available on the MathWorks website [MathWorks 2016].

3.5 Concluding Remarks

This chapter presents the verification of the impedance-mobility models formulated in Chapter 2, the validation of assumptions made in the models, and generalization

of the models of square unit cells to other geometries.

The TL of a single unit cell in a waveguide and a baffle calculated from the impedance-mobility models is compared to the TL from corresponding FEM models, with good agreement. The same is done for double layers of unit cells in a waveguide and 2×1 and 2×2 arrays in a baffle, with the same high degree of accuracy. A decrease in accuracy is noted at high frequencies for arrays of unit cells. This corresponds to the breakdown of the assumption that the unit cells behave as ideal elementary piston-like radiators.

Through manipulation of the FEM models to match the constraints used in the impedance-mobility approach, the assumptions of negligible bending stiffness and rotary inertia in the attached mass are tested. The bending stiffness of the attached mass does not significantly impact the TL of a single unit cell in a waveguide. By moving the attached mass off-center and varying its thickness, the effect of rotary inertia is tested. The out-of-plane rotation of the attached mass results in a resonance and TL peak at a specific frequency corresponding to the thickness of the attached mass and its location. The impedance-mobility approach accurately predicts TL away from this additional resonance.

By comparing the TL of a square unit cell to circular, hexagonal, and triangular unit cells of equivalent area, the degree to which the impedance-mobility approach can be used to predict the TL of different geometries is studied. The impedance-mobility model of a square unit cell of a membrane-type acoustic metamaterial with a centrally-located mass accurately predicts the TL of hexagonal and circular unit cells. Attached mass eccentricity degrades the predictive accuracy

of the model near the resonance corresponding to out-of-plane rotation of the attached mass. The TL of triangular unit cells is predicted substantially less accurately than those of hexagonal or circular geometries. However, for regular-polygonal unit cells with centrally-located attached masses, the impedance-mobility accurately predicts TL.

In designing membrane-type acoustic metamaterial noise barriers, the shape of the unit cell can be determined by external factors, such as ease of fabrication. For regular-polygonal unit cell shapes with centrally-located attached masses, the impedance-mobility model of a square unit cell with an equivalent area can be used to accurately predict the TL response.

In addition to being accurate, the impedance-mobility model is also computationally efficient. This enables optimization using genetic algorithms which is presented in Chapter 4, and the formulation of tools for design such as the GUI shown in this chapter.

Chapter 4

Optimization Using Genetic Algorithms

Determining the transmission loss (TL) of membrane-type acoustic metamaterial noise barriers involves many design parameters that are often inter-connected. In fact, the TL for a single unit cell set in a waveguide formulated in Chapter 2 is a function of thirteen distinct variables. For a configuration of two unit cells arrayed in a baffle or layered in series, that number more than doubles. Additionally, each variable can take any value, which creates an infinite number of possible unit cell configurations. As discussed in the introductory chapter, an exhaustive search for an optimal design is not computationally possible, or practically feasible.

To optimize the performance of a unit cell to meet specific design criteria, a genetic algorithm (GA) is applied. A GA is a global optimization method that iteratively improves each set of candidate solutions, or generation, by using information from past generations. Characteristics of high-performing candidate solutions are passed on to the next generation. GAs are especially well-suited to

problems, such as the one at hand, that contain many variables and/or nonlinear fitness functions. The flowchart in Figure 1.5 describes the basic GA process.

This chapter explores the implementation of GAs to optimize the TL of membrane-type acoustic metamaterial unit cells. Each step of the GA is discussed, focusing on how they are implemented in this research. A variety of noise source spectra and corresponding fitness functions used to design optimal configurations of membrane-type acoustic metamaterial unit cells to control them are presented. Results of a selection of case studies are presented in Chapter 5 to illustrate the usefulness of GAs for design problems.

4.1 Design Variables

The design variables that determine the unique TL response of the unit cell, and the fitness of a candidate solution, can either be continuous or discrete. Continuous variables can take any value inside of a specified range, whereas discrete variables are chosen from a finite set of possibilities. Genetic algorithms are inherently well-suited for optimizing fitness functions that include any combination of continuous or discrete variables. To shed light on the connections between design variables the GA is performed twice, once with the assumption that all design variables are continuous, and again assuming that there is a finite set of materials from which the substructure can be fabricated.

For the specific case of membrane-type acoustic metamaterials, the thirteen design variables are defined in Table 4.1, and are free to take values in the specified

Table 4.1: Design variable ranges

Parameter	Symbol	Units	Minimum	Maximum
Unit cell width	L_x	mm	15	35
Unit cell height	L_y	mm	15	35
Membrane thickness	t_{mem}	mm	0.0125	0.1506
Membrane density	ρ_{mem}	kg/m^3	900	2500
Membrane tension	T	N/m	50	500
Membrane elastic modulus	E	GPa	0.0008	5
Membrane Poisson's ratio	ν	-	0.3	0.5
Mass density	ρ_{mass}	kg/m^3	1000	20000
Mass thickness	t_{mass}	mm	1.5	6
Mass width ratio	$l_{x,r}$	-	0.01	0.25
Mass height ratio	$l_{y,r}$	-	0.01	0.25
Mass x location ratio	$x_{0,r}$	-	0.0625	0.5
Mass y location ratio	$y_{0,r}$	-	0.0625	0.5

ranges. These values are carefully chosen to ensure that randomly generated configurations are physically viable. For example, the membrane thickness is limited to a range in which most commercially available materials lie. The membrane properties are limited to ranges that encompass densities, elastic moduli, and Poisson's ratios of materials that are likely to be used (see Table B.4). The applied tension is limited such that the resultant stress is not likely to cause failure of the material.

It is probable that a manufacturer may only be able to choose from a finite set of materials, unit cell sizes, or mass sizes. In this case the discrete form of the GA or a combination of continuous and discrete can be used to optimally design unit cell configurations. The possible membrane and mass materials used in this research, are listed in Tables B.4 and B.5, respectively. Possible mass sizes are given in Table B.6. Notice that the number of materials and mass sizes in the selected sets are powers of two, which facilitates the conversion of the binary string to represent a

material number or mass size. For numbers that are not powers of two, some other encoding/decoding scheme is necessary to convert between material identifier and binary representation.

4.2 The Population

In GAs the set of candidate solutions to the optimization problem is called the population. The population changes and improves over time with each new generation. The candidate solutions in a population are represented by binary strings called chromosomes, which are subdivided into genes as shown in Figure 4.1. The genes are then decoded into a set of input variables for the fitness function. The initial population is a randomly generated set of chromosomes.

$$\overbrace{\underbrace{1010010}_{Gene1}\underbrace{1010110}_{Gene2}\underbrace{1011101}_{Gene3}\ldots}^{Chromosome}$$

Figure 4.1: Chromosome representation

To assess the performance of a candidate solution, the representative chromosome must first be decoded into a set of input variables. A binary string of B bits can be converted to an integer via the equation

$$Int = \sum_{i=1}^{B} Bin(B - i + 1) \cdot 2^{i-1}, \tag{4.1}$$

where Bin is the binary string corresponding to a gene and its argument is the bit location ranging from 1 to B. Once an integer value, Int, is obtained, the result can

be used directly as a representative for a discrete set of variables, as in the case for selecting one component over another. Alternatively, the integer can be scaled to fit the range of values that a parameter, x, can take by specifying a minimum and maximum value, x_{min} and x_{max} respectively, and applying the equation

$$x = x_{min} + \frac{x_{max} - x_{min}}{2^B - 1} Int. \tag{4.2}$$

In this research seven bits per gene are used to represent the range of possible values for each design variable. This results in 128 different design variable values in the specified ranges, which adequately sample the range of possible values for each parameter. Increasing the number of bits per gene increases the density of variable values and exploration of the search space, while decreasing computational efficiency. Design variables that require a more detailed search can use more bits in the encoding/decoding process resulting in a finer resolution. For the case of optimizing a single unit cell set in a waveguide, the chromosome representing a unique solution is $(13 \times 7 =)$ 91 bits in length.

4.3 Fitness Functions

The fitness score of each candidate solution is a measure of its performance by which it is ranked against other solutions. The GA attempts to maximize this score. It is the job of the noise control engineer to create a fitness function that adequately defines the goal of the noise barrier for a given task.

This section describes several types of scenarios that noise control engineers may encounter, and how GAs can be applied to create treatment using membrane-type acoustic metamaterials. Developing fitness functions for broadband noise, noise focused in a single octave band or one-third octave band, discrete frequency noise, and noise with multiple discrete frequency components is discussed.

This section is not intended to be a panacea for the design of noise control solutions via GAs, but to serve as a guide to address some common scenarios. Each unique situation will require careful thought to fully characterize a successful treatment, and to formulate a metric that quantifies the degree of success. The fitness functions outlined below for common scenarios may serve as a good starting point to create fitness functions for specific cases.

4.3.1 Broadband

In many noise control scenarios, the character of the noise source is unknown or is known to vary greatly in level and/or spectrum. The spectrum of the noise source may also be broadband in nature, such as the one shown in Figure 4.2. In these cases, it is often necessary to design a noise barrier that works well over a wide range of frequencies.

To maximize broadband transmission loss of the unit cell over a finite range, the average transmission loss over that range, given by Equation (4.3), can be used as the fitness function. Here F_j is the fitness score of the j^{th} candidate solution, and

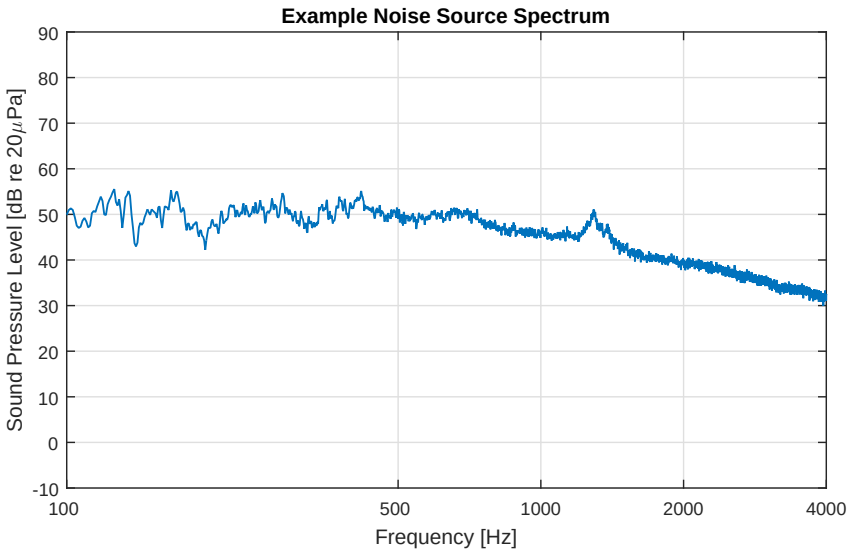

Figure 4.2: Example of predominately broadband sound pressure level spectrum of HVAC equipment

ω_{max} and ω_{min} are the highest and lowest frequencies of interest, respectively.

$$F_j = \frac{\int_{\omega_{min}}^{\omega_{max}} TL(\omega)\mathrm{d}\omega}{\omega_{max} - \omega_{min}} \tag{4.3}$$

In this research, the frequency range of interest is 100 Hz to 4000 Hz.

4.3.2 Narrow Band

Similarly, noise sources with a large portion of their energy in a smaller range of frequencies can be characterized using the fitness function given by Equation 4.3 by altering the maximum and minimum frequencies of interest. An example of this type of noise spectrum is shown in Figure 4.3.

A special case of noise characterization in narrow bands that is particularly interesting to engineers is octave band levels. Some measurement equipment will only report values in octave or third-octave band levels, thus it is useful to design

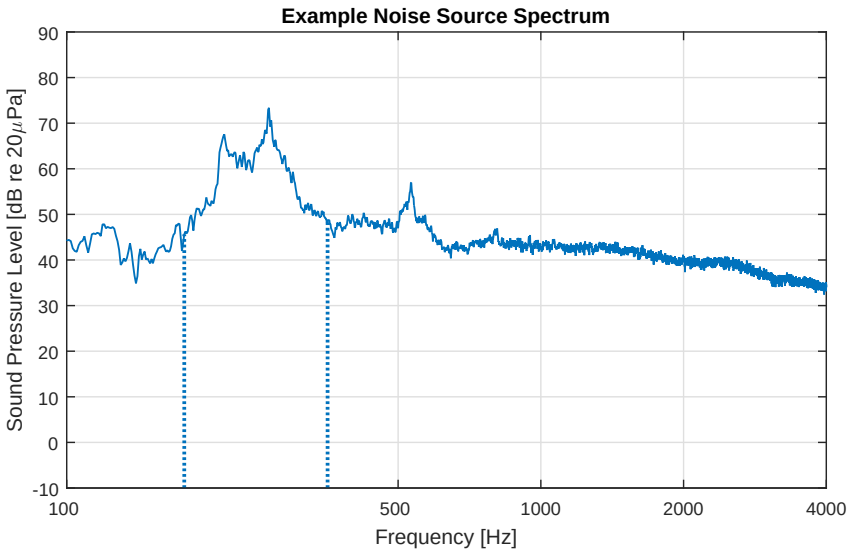

Figure 4.3: Example sound pressure level spectrum of HVAC equipment with high level in the 250 Hz octave band, which is delineated by the dotted lines

noise control solutions using the same bands. The frequency limits for octave and third-octave bands are given in ANSI S1.11 [2004].

In this manner, the TL of a membrane-type acoustic metamaterial unit cell can be maximized in the octave band that contains the most noise energy. For the example in Figure 4.3, the octave band centered around 250 Hz contains the most energy, therefore the upper and lower limits of Equation (4.3) should be set to 355 Hz and 177 Hz, respectively, to maximize TL in that band. These limits are delineated by the vertical dotted lines in the figure.

In the same manner that fitness scores for octave bands can be obtained, one-third octave bands can also be used. If a noise source's spectrum is only known in one-third octave bands, such as the case shown in Figure 4.4, it is appropriate to devise an optimization scheme based on the same band structure.

In this scenario, designing a noise barrier to optimally reduce the sound level in

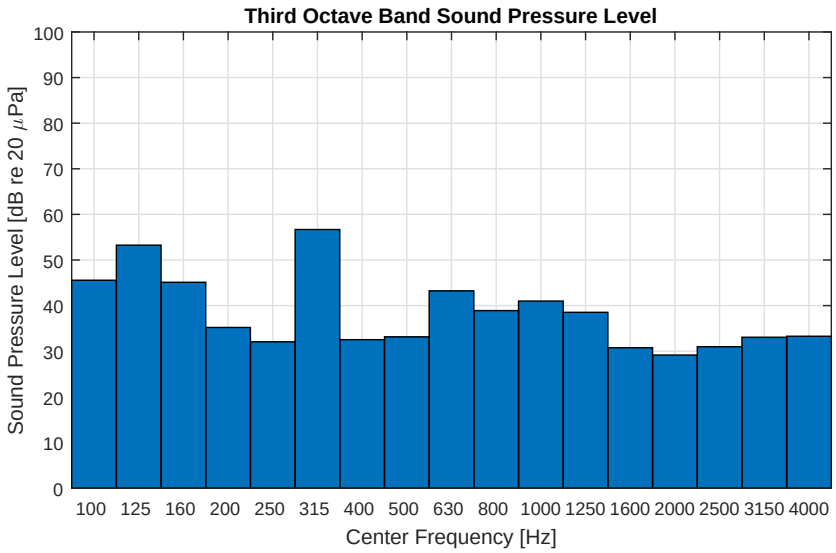

Figure 4.4: Third octave band sound pressure level of water-cooled screw chiller

the 315 Hz one-third octave band can be accomplished by using Equation (4.3) with frequency limits of 282 Hz and 355 Hz as a fitness function.

4.3.3 Discrete Frequency

Equipment with rotating or oscillating elements often emit noise primarily at frequencies determined by the speed of rotation. In this situation, it may be desirable to design a noise barrier that has its maximum transmission loss at the problem frequency. For this specific application, the transmission loss can be used as the fitness score directly. Finding the optimal configuration to attenuate a tone can be accomplished using the fitness function

$$F_j = TL(\omega_0), \tag{4.4}$$

where ω_0 is the frequency of the tone.

Figure 4.5 shows an example of noise with a prominent tone at 613 Hz. To

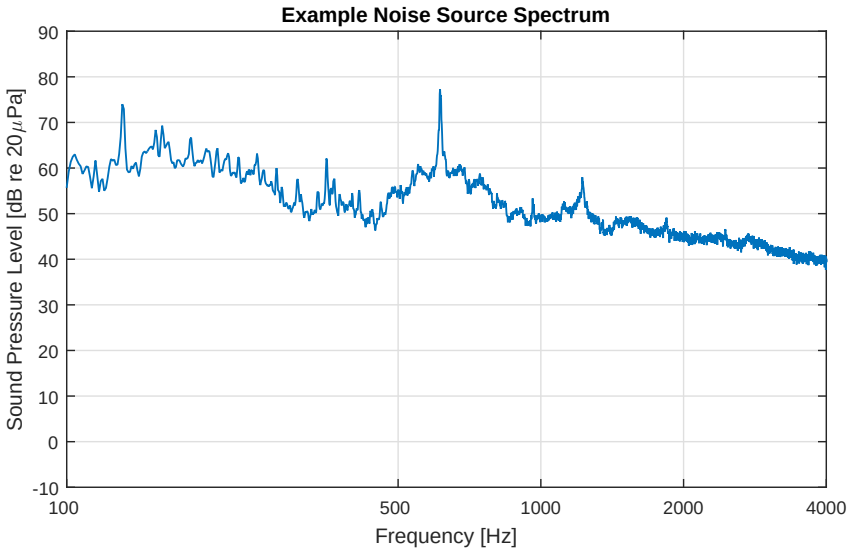

Figure 4.5: Example of a noise source spectrum containing a prominent tone

design a membrane-type acoustic metamaterial unit cell with TL peak frequency coincident with the problematic tone, the fitness function given by Equation (4.4) is used. In the example shown, the argument ω_0 is set to 613 Hz.

4.3.4 Multiple Discrete Frequencies

Similarly, attenuating a noise source comprised of one or more tones can be accomplished using a fitness function that is a linear combination of the transmission loss at the frequencies of interest as follows,

$$F_j = \sum_{n=1}^{N} a_n TL(\omega_n), \tag{4.5}$$

where $TL(\omega_n)$ is the transmission loss at the n^{th} frequency of interest and a_n is its respective (real and positive) weighting factor. Using this fitness function allows the

noise control engineer to assign priority to the most problematic tones, while still addressing tones that may be less troublesome.

For a noise source that contains multiple discrete frequency tones, such as that in Figure 4.6, an engineer may want to design a membrane-type acoustic metamaterial noise barrier that will consider the frequency and relative amplitudes of the tones in the example.

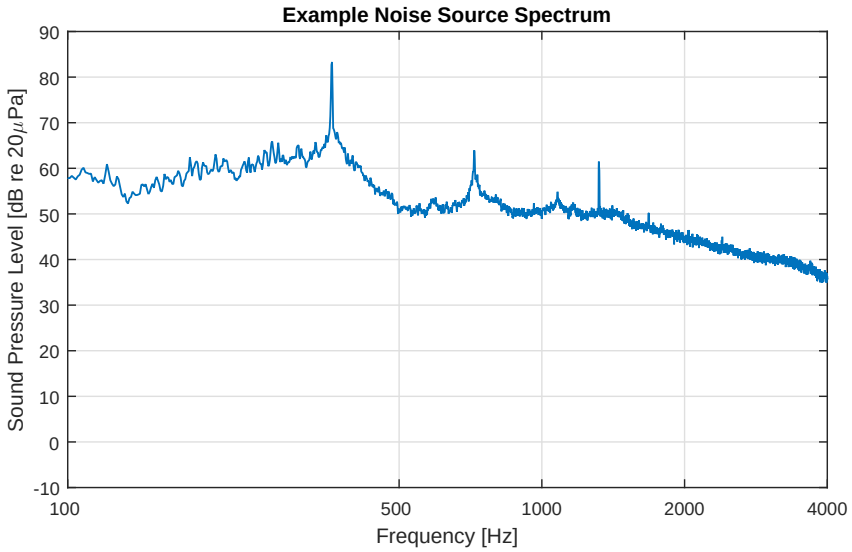

Figure 4.6: Example of a noise source spectrum containing multiple tones

To do this, the fitness function given by Equation (4.5) can be used with component weights shown in Figure 4.7. The most prominent tones are weighted more heavily than the others, resulting in a fitness function that prioritizes design criteria.

4.3.5 Mass Law

In addition to the TL of the unit cell, the total weight may also be an important design criterion. In the analysis of membrane-type acoustic metamaterial noise

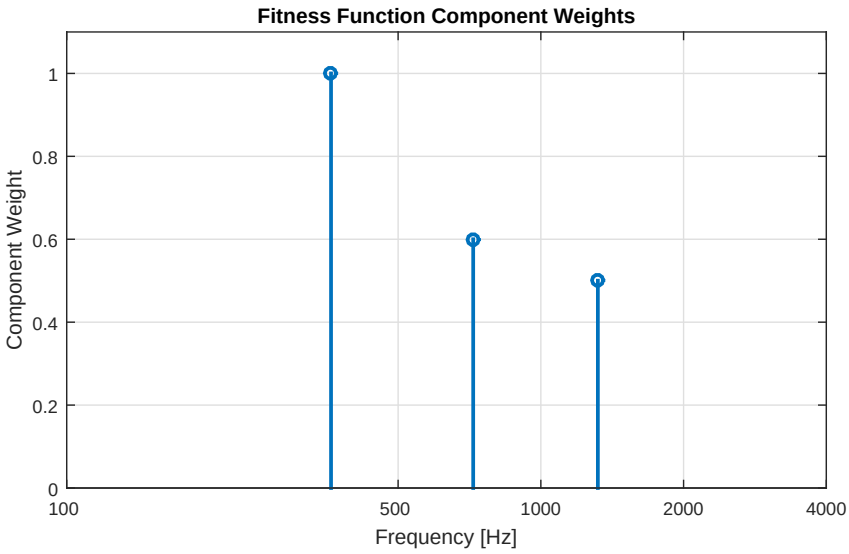

Figure 4.7: Example of component weights for a fitness function

barriers, the mass law is the standard by which performance is often gauged. The mass law, Equation (1.1), gives the TL of a thin limp panel of infinite extent and surface density ρ_s. For every doubling of mass, or surface density, the mass law TL will increase by approximately 6 dB.

The fitness functions derived in the previous sections can be altered so that the increase in TL above the mass law is the quantity considered. This will prevent the GA from simply adding mass to a unit cell to improve its TL. To do this the transmission loss due to the mass law can be subtracted from the TL of the membrane-type acoustic metamaterial unit cell, before being used in the fitness function. Equations (4.3) - (4.5) can be re-written to account for the mass of the unit cell as

$$F_j = \frac{\int_{\omega_{min}}^{\omega_{max}} TL(\omega) - TL_m(\omega) \mathrm{d}\omega}{\omega_{max} - \omega_{min}}, \tag{4.6}$$

$$F_j = TL(\omega_0) - TL_m(\omega_0), \tag{4.7}$$

and

$$F_j = \sum_{n=1}^{N} a_n \left(TL(\omega_n) - TL_m(\omega_n) \right), \tag{4.8}$$

respectively, where TL_m is the mass law transmission loss.

Since fitness-proportionate selection, which is described in the next section, requires fitness function values to be real and positive, negative values of F_j are rounded up to zero. This ensures that the probability at which each candidate solution is selected can be computed. Additionally, it guarantees that candidate solutions with fitness function values of zero or less will not be selected.

4.4 Selection, Crossover, and Mutation

The heart of the GA is the set of processes that mimic natural selection and Darwinian evolution. "Survival of the fittest" dictates that attributes of higher-performing chromosomes will be passed on to future generations due to selection. The combination of these attributes occurs through the process of crossover. Mutation introduces genetic diversity into the population by randomly altering a chromosome. This section details the parameters of each process used in the design of optimal unit cells of membrane-type acoustic metamaterials.

Selection is the process by which candidate solutions are chosen to pass on their characteristics to the next generation. In this research a combination of elite

selection and fitness-proportionate selection is used. In elite selection, a certain number of the top-performing candidate solutions are chosen to proceed. This guarantees that the best-performing candidates in any given generation survive and pass on their genetic material. In addition to ensuring that superior genes are passed on, it also ensures that each subsequent generation's top performing candidate is at least as fit as the previous generation's. In fitness-proportionate selection, chromosomes are selected with a probability based on their fitness scores given by Equation (1.21).

In this research, the two most fit candidate solutions out of a total of 96 per generation are chosen via elite selection. To keep the number of candidate solutions in each generation constant, 94 chromosomes are chosen using fitness-proportionate selection. It is possible that some, most likely higher-performing, candidate solutions are chosen multiple times. The 94 selected chromosomes then move on to swap genetic information via crossover, creating 94 new chromosomes that are added to the two elite chromosomes to create the new generation.

Crossover is the process by which genetic information from two chromosomes is combined to create new chromosomes. The most common form, and what is used in this research, is single-point crossover. In this scheme a random point in the chromosome is chosen and the bits to the left of that point from one chromosome and to the right of that point in another, and vice-versa, are combined to make two new chromosomes. Additionally, maximum-minimum crossover is used which sequentially pairs the most and least fit chromosomes for crossover. This creates more genetic diversity by mixing attributes of high-performing candidates with

those of low-performing ones.

Mutation randomly introduces additional genetic diversity by changing a random bit in a gene from a one to a zero or vice versa. The probability at which mutation occurs is set at $\mu = 0.1$ in this research to introduce more genetic material into the population. To ensure that each generation improves upon the last or at least remains the same, the highest performing solution is immune from mutation.

4.5 Convergence

The stopping criteria of the GA determine when an optimal solution has been reached. Convergence is reached when the best chromosome, and its fitness score, remains unchanged for many generations. For this research, the GA stops when a particular candidate solution has the highest fitness score for ten consecutive generations. Figure 4.8 shows an example of GA convergence. The maximum, average, and minimum fitness scores in each generation are shown. Notice that the maximum fitness score increases or remains constant with each subsequent generation, ensuring convergence. The minimum fitness score, representing the least fit candidate solution, varies wildly due to the introduction of new genetic material through mutation. If the GA fails to converge on an optimal solution, the GA is stopped when the number of generations reaches a predefined limit, set to 200 in this research so that the algorithm is likely to converge.

The GAs were implemented using custom scripts in MathWorks MATLAB 2015a and computed on a Windows PC with an Intel Core-i5 3.4 GHz processor and

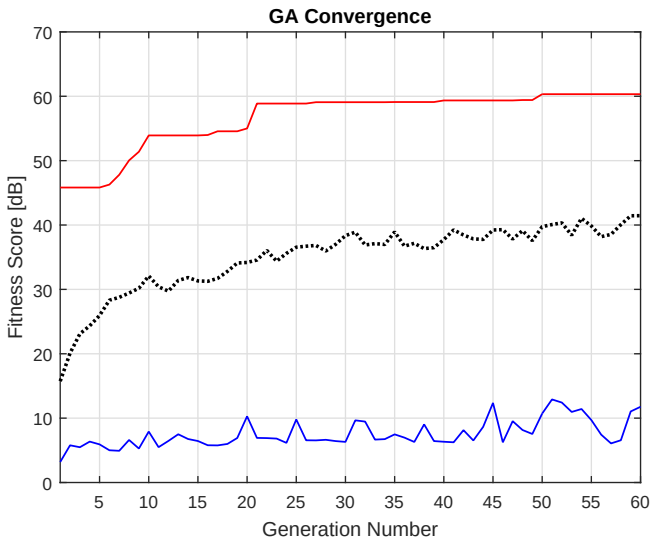

Figure 4.8: Example of GA convergence. Generation maximum (red solid), average (dotted), and minimum (blue solid) fitness score.

16 gigabytes of RAM. In the example shown in Figure 4.8, convergence was reached in 60 generations, resulting in (60×96=) 5760 evaluations of unit cell TL using the impedance-mobility approach. The process took 20 minutes and 17 seconds. The same GA using a FEM model as described in Chapter 3 to evaluate the fitness of each candidate solution would take 592 days to complete. See Table B.8 for further information on the efficiency of FEM models. Implementing a GA would not be feasible without the computationally efficient models developed in Chapter 2.

4.6 Concluding Remarks

This chapter presents the application of genetic algorithms to find optimal configurations of membrane-type acoustic metamaterials. Fitness functions were developed to maximally attenuate broadband, narrow band, discrete frequency, and multiple discrete frequency component noise. Each step in the GA is discussed,

focusing on how they are implemented in this research. The stopping criteria and convergence are noted. Chapter 5 presents the results of the GAs applied to the TL from the impedance-mobility formulation of a unit cell of a membrane-type acoustic metamaterial in a waveguide using each of the fitness functions described in this chapter.

Chapter 5

Results

This chapter is divided into two sections. The first section presents the results of studies conducted using the impedance-mobility models formulated in Chapter 2 and verified in Chapter 3. Design variables are manipulated independently to show their effect on the transmission loss of a unit cell, cell arrays, and double layers of unit cells. This serves to illustrate the myriad possible configurations and resulting TL profiles, and informs the necessity of an optimization scheme.

The second section presents the results of genetic algorithm optimization using the fitness functions developed in Chapter 4. By simultaneously altering each design parameter and iteratively improving the unit cell configuration, the GA eliminates the otherwise arduous process of design. The GAs are applied to each scenario three times, once with each design variable free to take a value within its specified range, again using a fitness function that accounts for the total weight of the unit cell, and yet again with a limited selection of materials available. The design variable ranges are given in Table B.3, and the selected materials are given in Tables B.4 - B.7.

5.1 Impedance-Mobility Model

5.1.1 Single Unit Cell

To understand the impact that each design variable has on the transmission loss of the structure, the impedance-mobility model is used to study its deviation from a baseline configuration of a single unit cell in a waveguide. The parameter values used for the baseline configuration are given in Table B.1, and the corresponding transmission loss is shown in Figure 5.1.

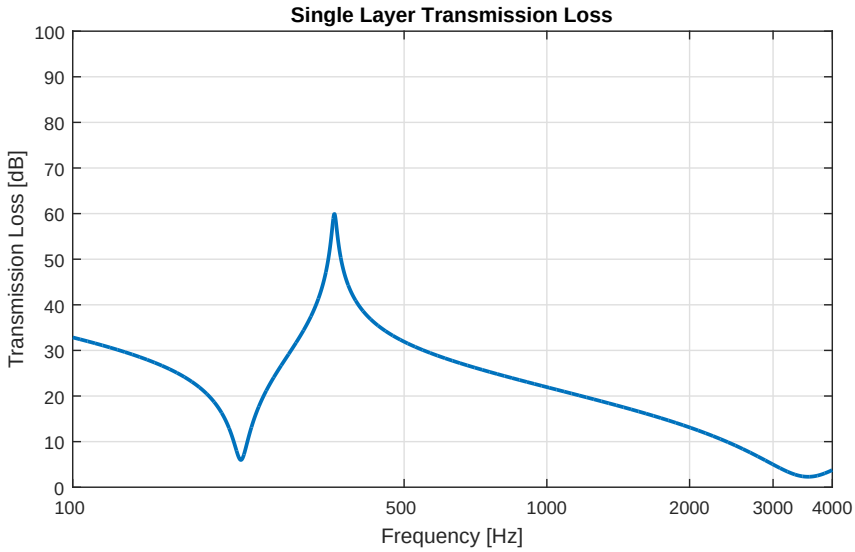

Figure 5.1: TL of unit cell with baseline parameters given in Table B.1

There are three main parts of the TL curve that will be discussed in this Chapter, two resonances and a TL peak. The first resonance for the baseline configuration occurs at 226 Hz corresponding to maximum in-phase vibration of the membrane and attached mass. The second resonance at 3560 Hz occurs when the attached mass remains stationary and the membrane vibrates independently. The TL peak occurs between these two resonances at 356 Hz, where the surface-average

displacement is zero, leading to perfect reflection of the incident wave. Figure D.1 in Appendix D shows the displacement at each of these frequencies.

5.1.1.1 Waveguide vs. Baffle

It is useful from the standpoint of a noise control engineer to examine how sound is reduced by a membrane-type acoustic metamaterial used as a partition or barrier. A first step in doing this is considering the TL of a unit cell which radiates its energy into a hemispherical half-space bounded by a rigid planar baffle. This simulates its response when set in a wall or other approximately rigid surface much larger than a unit cell. The TLs of single unit cells set in a waveguide and in a baffle are shown in Figure 5.2.

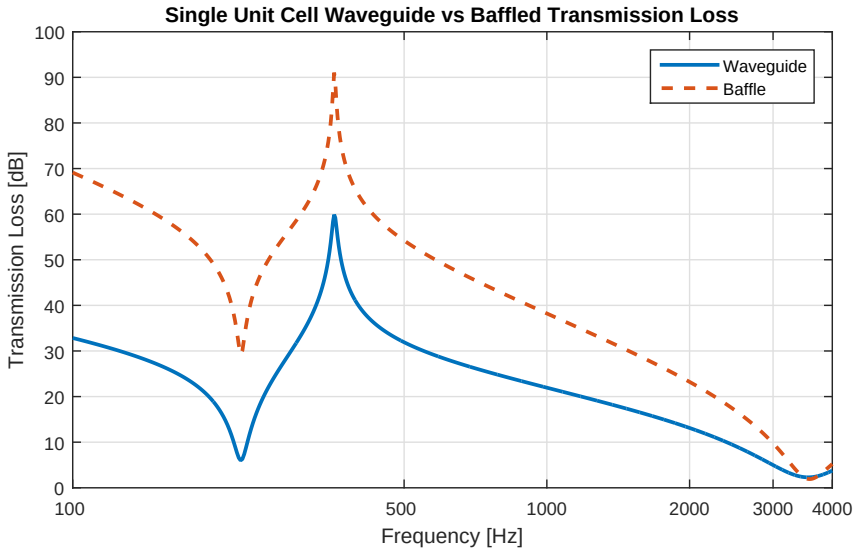

Figure 5.2: Comparison of TL of unit cell in a waveguide (solid) and a baffle (dashed)

The baffled TL is approximately 40 dB greater than that of the waveguide below the first resonance frequency, and 30 dB higher at the TL peak frequency. As

the frequency increases, the TL approaches that of a unit cell in a waveguide.

The higher TL that is seen with an identical unit cell set in a baffle is easily explained by examining the modal radiation efficiency for a simply supported panel. Figure A.3 in Appendix A shows that the radiation efficiency for each mode increases as a function of frequency. This means that at low frequencies, the vibratory motion of the unit cell does not couple well with the surrounding fluid. In a waveguide the radiated sound propagates as a plane wave and the unit cell effectively behaves as a rigid piston, which has unity radiation efficiency, leading to a maximum transmitted sound power and minimum TL. The TL of a unit cell in a waveguide can thus be treated as the lower limit of TL obtainable by an ideal membrane-type acoustic metamaterial unit cell.

5.1.1.2 Angle of Incidence

For a finite plate or membrane in a rigid baffle, the angle of incidence can influence the transmission loss when the trace wavelength of the incident wave matches that of the panel. The angle of incidence is explored using Equation (E.12) for the generalized modal force acting on the unit cell. For a membrane-type acoustic metamaterial, there is little effect of varying incidence angle due to the small dimensions of the unit cell since $ka \ll 1$, where ka is the dimensionless spatial frequency parameter. This is shown in Figure 5.3, where there is less than 1 dB of change between normally and obliquely ($\alpha = 78°, \beta = 78°$) incident excitation from 2000 Hz to 4000 Hz. Here α and β are the angles from the normal vector of the unit cell in the x and y directions, respectively. There is practically no difference in TL

at lower frequencies.

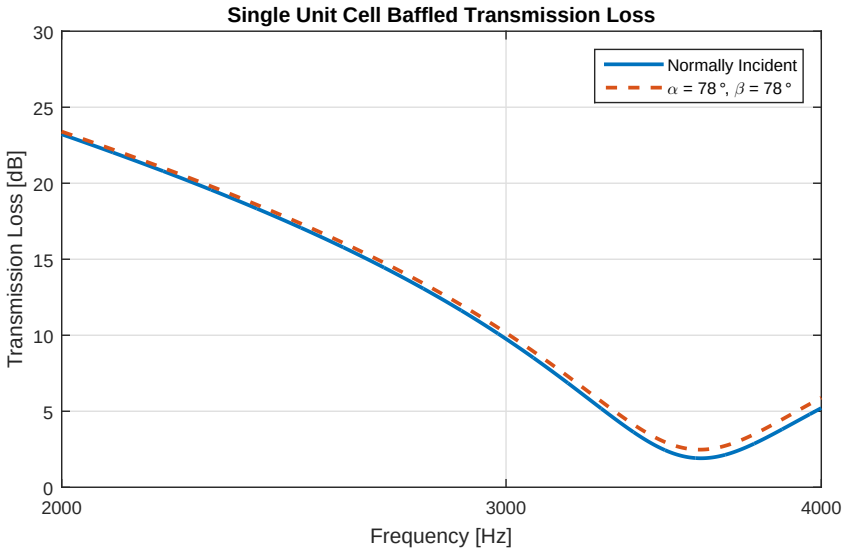

Figure 5.3: Comparison of TL of unit cell in a baffle for normally incident (solid) and obliquely incident (dashed) excitation

5.1.1.3 Membrane Tension

The resonance frequencies of an unloaded membrane of dimensions $(L_x \times L_y)$ are given by the equation

$$\omega_m = \sqrt{\frac{T}{\rho_s}} \sqrt{\left(\frac{m_1 \pi}{L_x}\right)^2 + \left(\frac{m_2 \pi}{L_y}\right)^2}, \tag{5.1}$$

where m_1 and m_2 are the mode numbers in the x and y directions, respectively. It is evident that the resonance frequencies are proportional to the square root of the tension, T, and it follows that the TL peak frequency is also proportional to the square root of the tension. Figure 5.4 shows the effect of increasing the tension applied to the membrane. The first and second resonances as well as the TL peak shift toward higher frequencies with increasing tension.

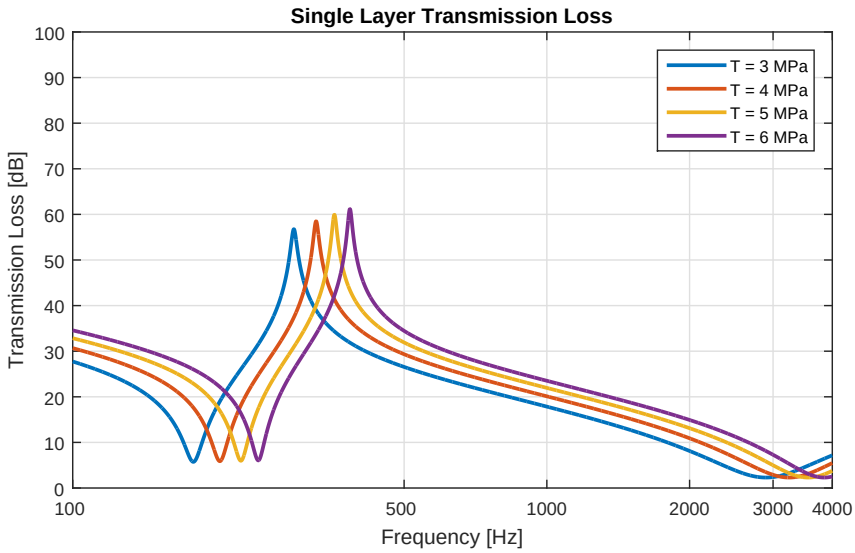

Figure 5.4: TL of unit cell with varied tension

5.1.1.4 Membrane Surface Density

According to Equation (5.1) the unloaded resonance frequencies of the membrane are proportional to $1/\sqrt{\rho_s}$. However, the first resonance frequency of the loaded membrane is negligibly affected by variations in the membrane surface density due to the presence of the attached mass. At the first resonance, the unit cell behaves similarly to a simple harmonic oscillator. At the second resonance frequency, the unit cell is maximally affected by variations in the membrane surface density since at this resonance the attached mass is stationary and does not affect the unit cell vibration. These phenomena are observed in Figure 5.5, where increasing the surface density of the membrane negligibly affects the first resonance and TL peak frequencies while decreasing the second resonance frequency.

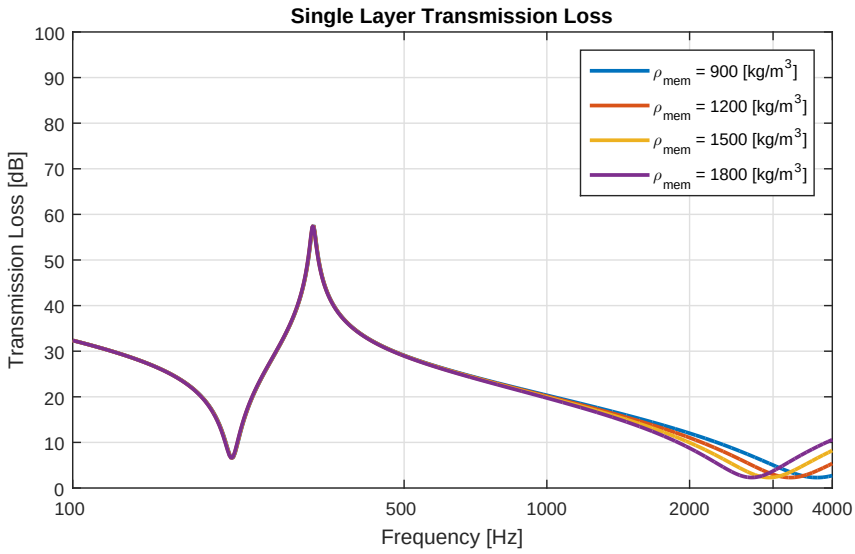

Figure 5.5: TL of the unit cell with varied membrane density

5.1.1.5 Membrane Stiffness

As illustrated in Section 2.1.2, the stiffness of a vibrating membrane is sometimes neglected in analytical models. To illustrate its importance, the impedance-mobility model is used to compare the TL of a unit cell in a waveguide with and without bending stiffness. Figure 5.6 shows the TL of a baseline unit cell with tension and stiffness (solid), tension only (dashed), and stiffness only (dotted).

It is evident that tension plays a much larger role in the TL of the unit cell. However, stiffness does affect the TL peak frequency which is the most important part of the TL profile. In the frequency range near the TL peak, the effective dynamic mass of the unit cell is negative which can be considered the defining characteristic of a metamaterial. It is therefore important to consider both tension and stiffness in models of membrane-type acoustic metamaterials.

It is also necessary to examine the degree to which the membrane stiffness

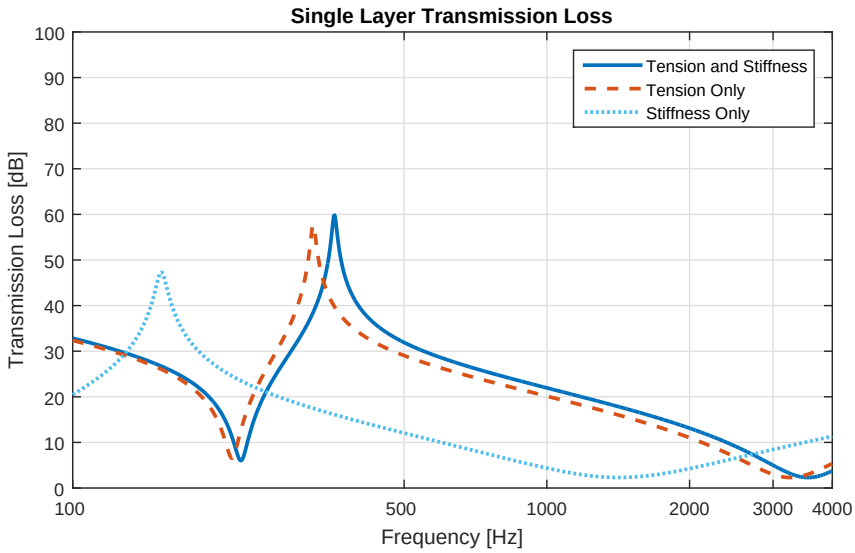

Figure 5.6: Comparison of TL for both tension and stiffness (solid), tension only (dashed), and stiffness only (dotted)

influences the TL of a unit cell. The natural frequencies of an unloaded plate are proportional to the square root of its stiffness, as shown in Equation (A.5). In the same manner as applied tension, as the stiffness increases (i.e. the Young's modulus of the membrane material increases), so do the resonance and TL peak frequencies.

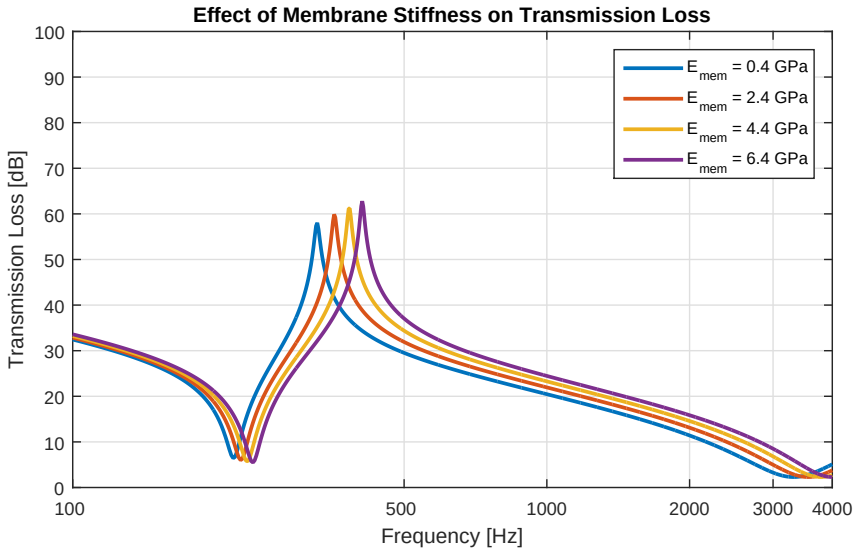

Figure 5.7: TL of unit cell with varied membrane stiffness

The TL is shown in Figure 5.7 with varying degrees of membrane stiffness. As the stiffness increases, the TL profile shifts toward higher frequencies. Increasing stiffness also increases the magnitude of TL at the peak frequency.

5.1.1.6 Attached Mass Density

The density of the attached mass, or more accurately its magnitude, affects the first resonance and TL peak frequency. At the first resonance, the mass and membrane vibrate in unison, and the attached mass experiences its largest displacement. Near this frequency, the unit cell behaves approximately as a simple harmonic oscillator, and the resonance frequency is approximated by $\sqrt{k/m}$ where k is the effective stiffness, and m is the magnitude of the attached mass. By holding the size of the attached mass constant, increasing its density increases the overall TL magnitude and the first resonance frequency of the unit cell decreases.

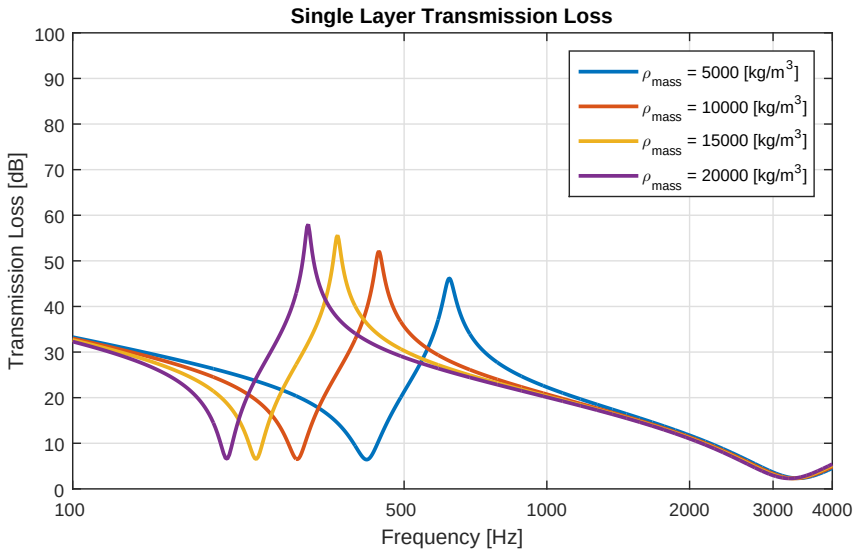

Figure 5.8: TL of unit cell with varied density of attached mass

Figure 5.8 shows the TL for various densities of a centrally-located 3 mm × 3

mm × 4.5 mm attached mass. As the mass density increases, the first resonance and TL peak frequencies decrease proportionally to $\sqrt{\rho_s}$. Since there is no deflection of the attached mass at the second resonance, its frequency does not depend on mass density.

5.1.1.7 Attached Mass Location

The location of the attached mass determines which membrane modes are maximally affected and, in turn, the frequencies at which the TL peak and resonances occur. To study this effect, the location of the mass is systematically moved on a square membrane according to Figure 5.9. Because of the diagonal symmetry of the square unit cell, only mass locations in the lower left octant need to be explored to fully characterize the response with an arbitrary mass location.

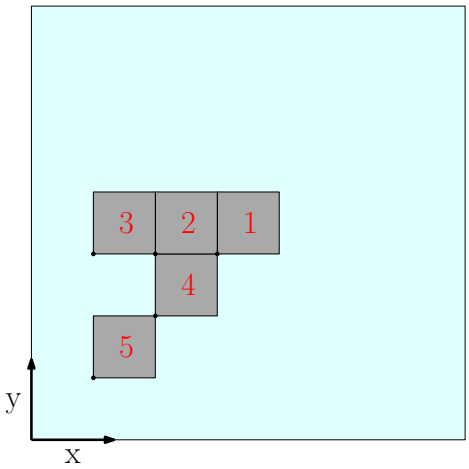

Figure 5.9: Mass locations

Figures 5.10 and 5.11 show the results. As the attached mass is moved farther from the center of the unit cell in the negative x direction, the first resonance frequency increases and the TL peak frequency decreases due to asymmetric

vibration of the unit cell. Additionally, the maximum TL decreases due to the smaller unit cell deflection at eccentric locations. At higher frequencies, addtional resonances occur due to the asymmetric vibration of the unit cell.

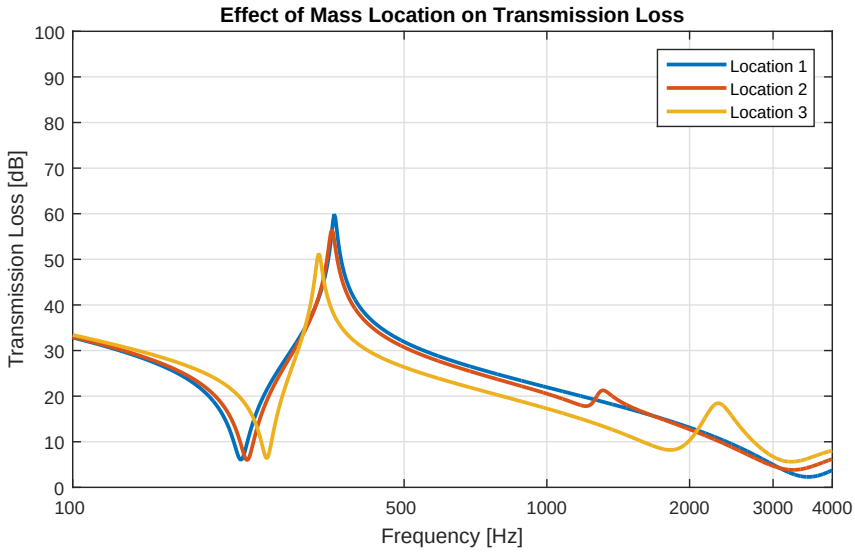

Figure 5.10: TL of unit cell with varied mass location

As the attached mass location moves diagonally from the center of the membrane, the same phenomena occur. At higher frequencies, more resonances and TL peaks occur due to doubly-asymmetric vibration of the unit cell.

5.1.1.8 Attached Mass Size

The primary effect of changing the size of the attached mass has relatively little to do with the mass itself. Increasing the size of the attached mass, as shown in Figure 5.12, decreases the distance between the outer edge of the membrane and the mass, which increases the frequency of the first resonance. This is shown in Figure 5.13. Additionally, increasing the size of the attached mass increases the effective density of the unit cell as a whole, which decreases the frequency of the

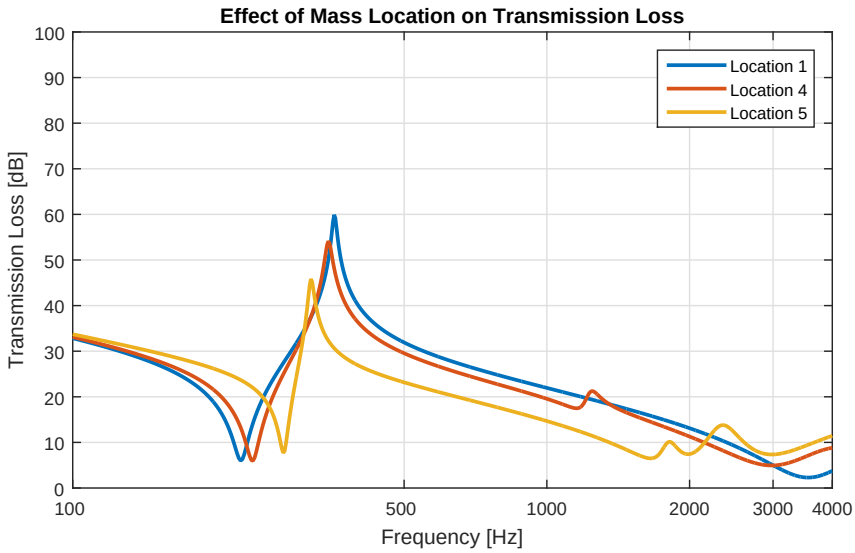

Figure 5.11: TL of unit cell with varied mass location

second resonance. The same phenomenon is seen in Figure 5.5.

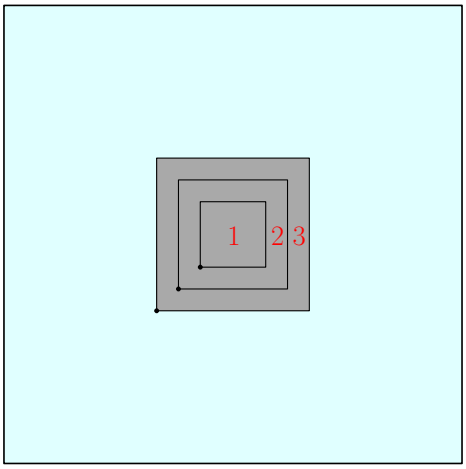

Figure 5.12: Mass sizes

5.1.1.9 Unit Cell Aspect Ratio

The shape of the unit cell affects the spacing between the resonance frequencies of the unloaded membrane. As the aspect ratio $r = L_x/L_y$ increases toward one while maintaining an equal unit cell area, the first resonance frequency associated with

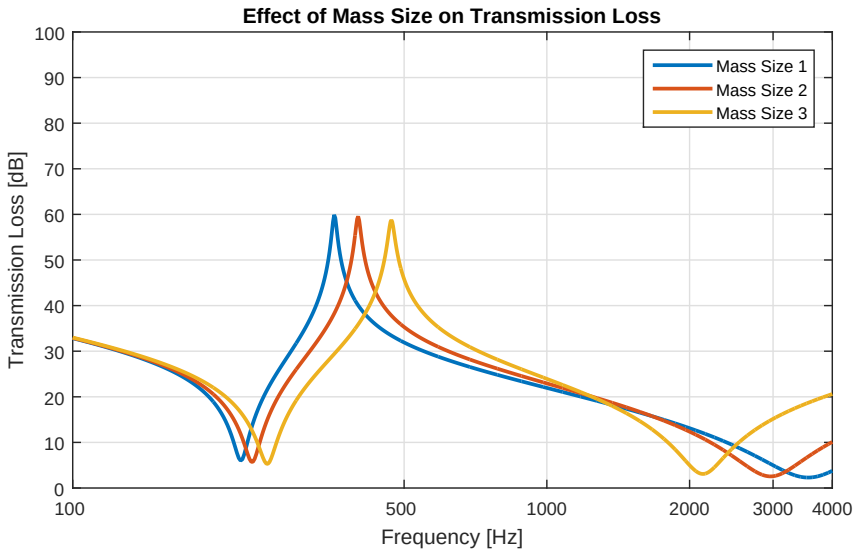

Figure 5.13: TL of unit cell with varied mass size

$m = (1, 1)$ decreases. This is also true for the loaded case, and can be seen in Figure 5.14. The second resonance of the loaded membrane occurs when the attached mass is stationary relative to the membrane. In the unloaded case, this corresponds to the $(2, 1)$ or $(1, 2)$ modes which in the case of a square, $(r = 1)$, have identical resonance frequencies. For aspect ratios other than one, however, the second resonance frequency is determined by the length of the longest side. Because of this, the second resonance frequency increases with increasing aspect ratio.

The TL peak frequency remains relatively unchanged, since the first and second resonances are decreasing and increasing, respectively, as the aspect ratio approaches 1.

5.1.2 Stacked Unit Cells

One method of increasing the overall TL of a membrane-type acoustic metamaterial noise barrier is to add a second layer separated by an acoustic cavity. Using the

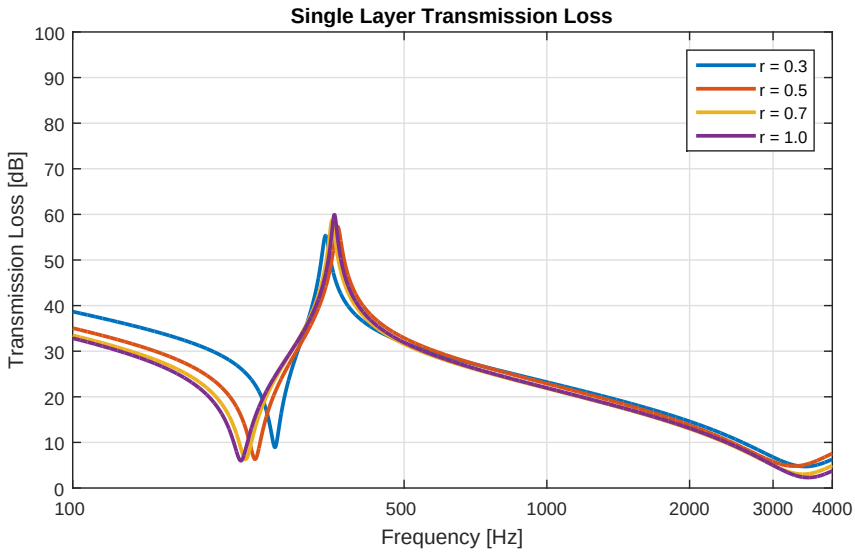

Figure 5.14: TL of unit cell with varied aspect ratio $r = L_x/L_y$

impedance mobility formulation described in Section 2.3, the TL curves of a single layer and a double layer of identical unit cells with an 8 mm air cavity in a waveguide are shown in Figure 5.15.

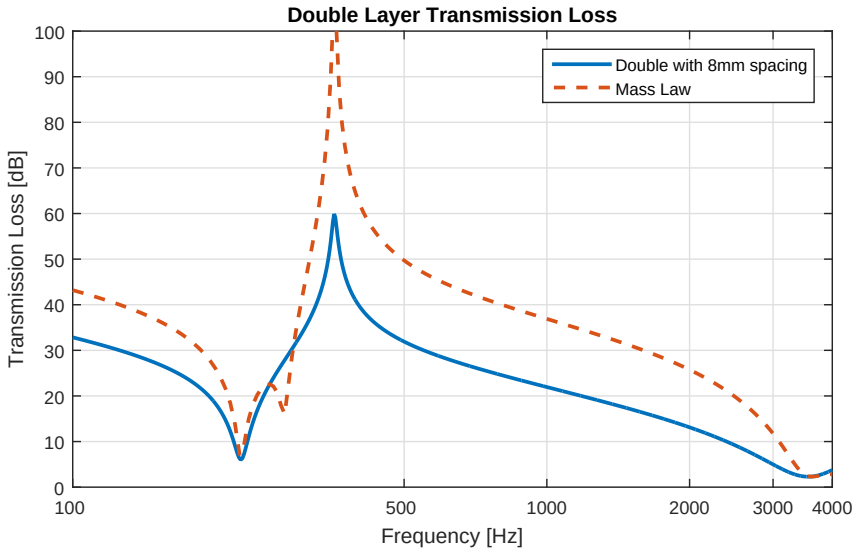

Figure 5.15: TL of a single unit cell in a waveguide (solid), and a double layer of identical unit cells with 8 mm stacking distance (dashed)

The broadband TL increases by about 10 dB, while the TL near the resonance

frequencies remains unchanged. An additional dip in the TL appears just above the first resonance frequency, where the two unit cells vibrate out of phase as shown using FEM in Figure 5.16. This corresponds to the half wavelength mass-air-mass resonance of the effective medium formed by the two unit cells and air cavity.

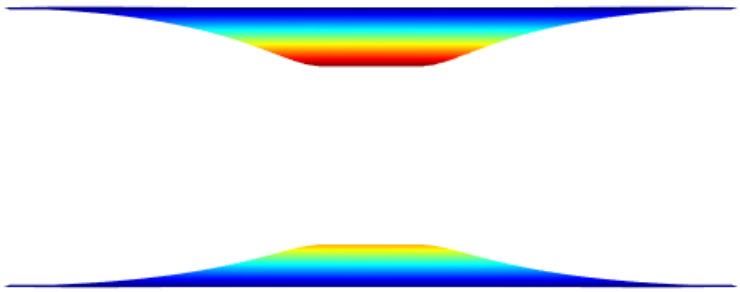

Figure 5.16: Cross-section of double layer unit cell deflection at 270 Hz

5.1.2.1 Stacking Distance

The stacking distance, L_z, between two unit cells in a double layer configuration determines the size of the acoustic cavity. This, in turn, affects the acoustic impedance of the cavity and coupled structural mobilities of each unit cell.

The effect of varying stacking distance on the TL of a double layer of identical unit cells in a waveguide is shown in Figure 5.17. As the stacking distance increases, the broadband TL increases by approximately 3 dB per doubling of stacking distance. The TL near the resonance frequencies remains unchanged.

The additional resonance introduced by the double panel configuration varies as a function of stacking distance. The additional resonance frequency decreases toward the first resonance as the stacking distance increases.

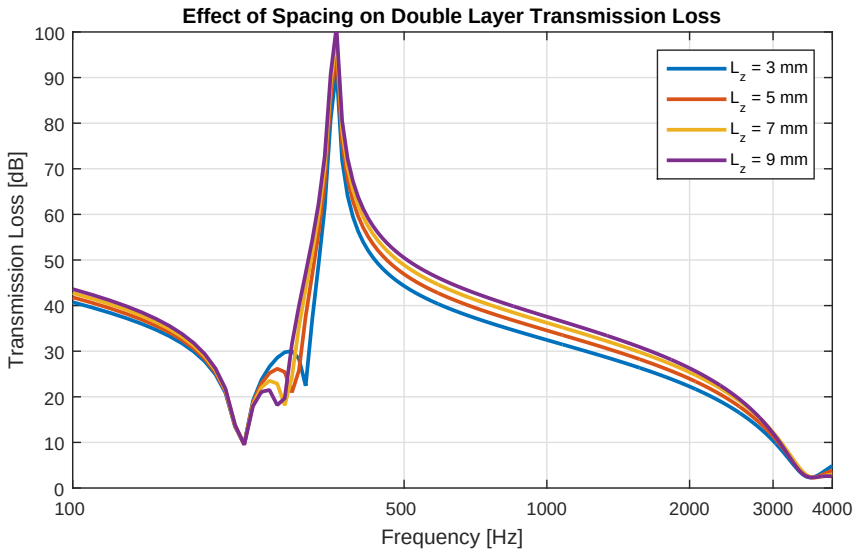

Figure 5.17: TL of double layer with varied stacking distance

5.1.2.2 Different Unit Cells

The TL profile of a double layer can be manipulated by altering one or both of the unit cells [Naify et al. 2012]. To study the effect of two different unit cells stacked in series, an alternate configuration is established with the parameter values given in Table B.2. The TL profiles of the individual unit cells and the double layer system with 5 mm stacking distance are shown in Figure 5.18. As with the double layer of identical unit cells, an approximately 10 dB overall increase in TL occurs with the double layer system of different unit cells. Each unit cell creates a distinct TL peak and first resonance which combine in the double layer system.

5.1.2.3 Stacking Order

Intuitively, the order in which an incident wave encounters a set of barriers could impact the attenuation of the wave. The truth, however, is revealed by examining Equations (2.67) - (2.69) and (2.77). In fact, the transmission coefficient is

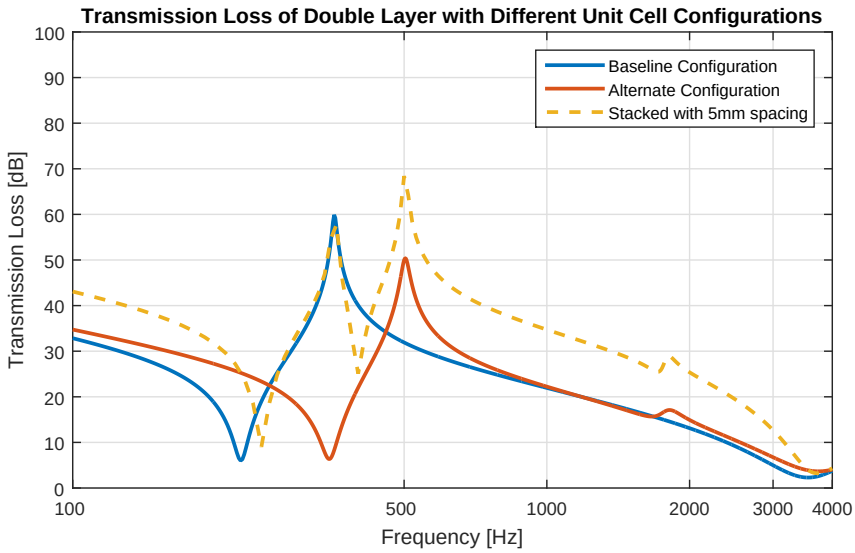

Figure 5.18: TL of double layer with different unit cell configurations. Baseline configuration (blue solid), alternate configuration (red solid), both configurations stacked with 5 mm spacing (dashed)

mathematically identical regardless of stacking order. This is verified in the plot in Figure 5.19, where the TL of two different unit cells is shown in both stacking orders.

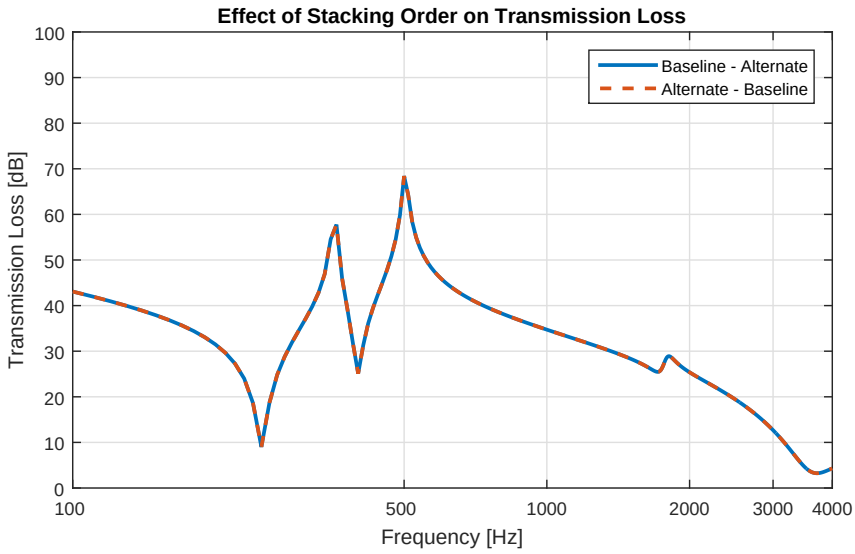

Figure 5.19: TL of double layer with different stacking order. Baseline then alternate configuration (solid), alternate then baseline configuration (dashed)

5.1.3 Multi-Cell Arrays

To study the TL of multi-cell arrays in a rigid planar baffle, the impedance-mobility approach with the negligible coupling assumption is used. In Chapter 3 this assumption was proven to be valid for frequencies below the second unit cell resonance frequency. Additionally, the expansion from a single unit cell to multi-cell array involves reducing the vibration of the unit cell to that of an equivalent elementary radiator. To ensure that this reduction is accurate, the TL of a unit cell in a baffle calculated using modal radiation efficiencies, and by reduction to an elementary piston-like radiator is plotted in Figure 5.20.

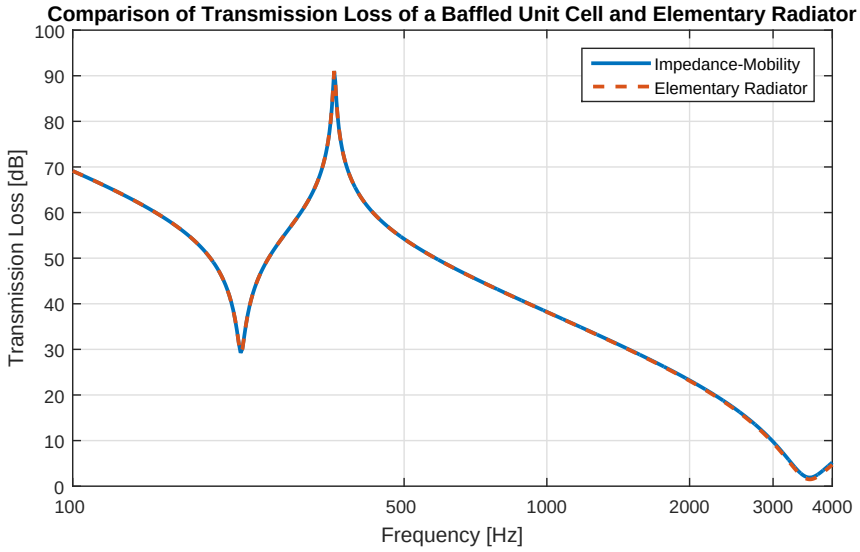

Figure 5.20: TL of a baffled unit cell (solid), and an elementary radiator with equivalent average velocity (dashed)

The TL curves plotted in Figure 5.20 appear to be identical. However, at high frequencies it is expected that there will be a reduction in accuracy due to values of ka increasing toward 1, where ka is the dimensionless spatial frequency parameter. This phenomenon is seen more clearly in Figure 5.21, though the discrepancy is less

than 1 dB at its maximum. This indicates that expansion to a multi-cell array using equivalent elementary radiators to represent unit cells is valid below the second resonance frequency.

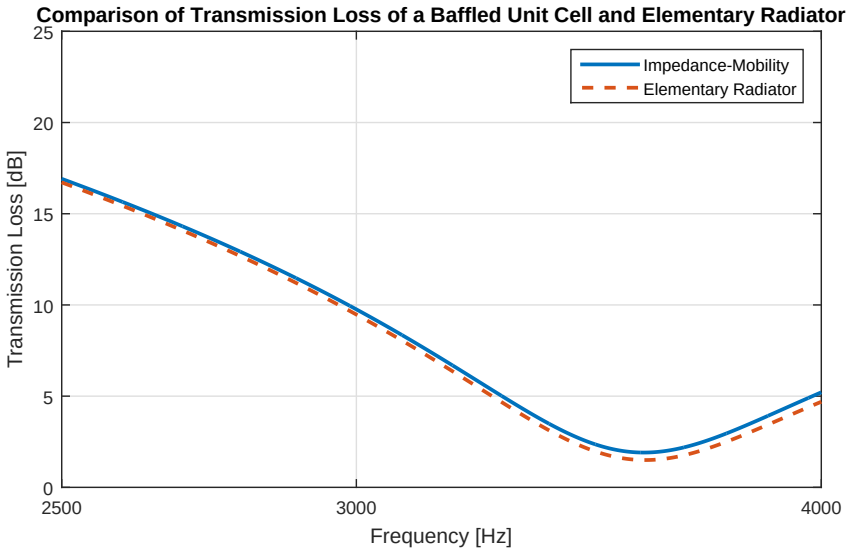

Figure 5.21: High frequency discrepancy between baffled unit cell (solid) and elementary radiator with equivalent average velocity (dashed)

5.1.3.1 Number of Unit Cells

As the number of unit cells in an array increases, so does the incident sound power carried by the plane wave given by $\Pi_{inc} = P^2 S/2\rho_0 c_0$, where P is the pressure amplitude, S is the total surface area, and $\rho_0 c_0$ is the characteristic impedance of the fluid medium. This, however, does not lead to a change in overall TL by itself since the velocity of each unit cell is determined by the pressure acting on it, not the overall incident sound power. The close proximity of adjacent unit cells leads to a doubling of radiated sound power when the number of unit cells is doubled (examine Equation (2.55) for insight). This gives rise to an approximately 3 dB decrease in

TL with each doubling of total unit cells. Figure 5.22 shows the TL for a unit cell, 2×1, 2×2, and 3×3 arrays in an infinite rigid baffle.

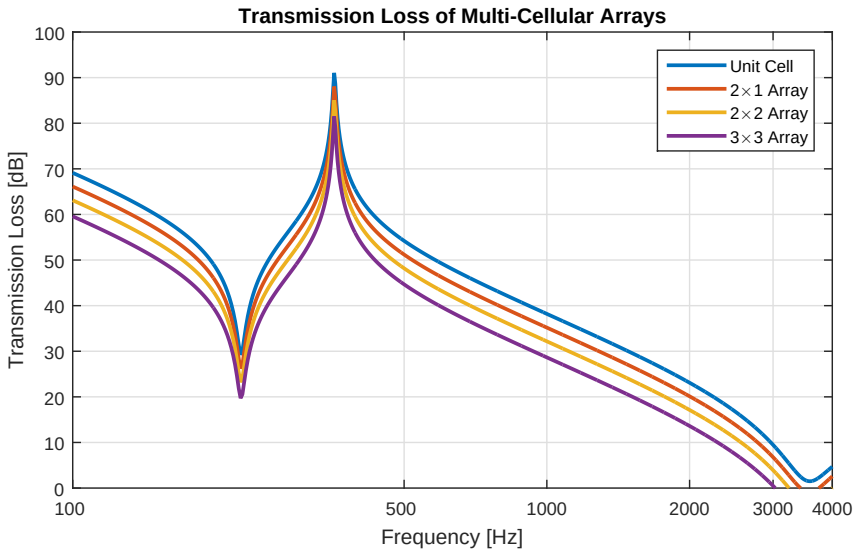

Figure 5.22: Transmission loss of baffled multi-cellular arrays

For larger numbers of unit cell the reduction in TL decreases asymptotically as the distance between adjacent unit cells increases. This is shown in Figure 5.23 for square arrays of 4×4, 5×5, 6×6, and 7×7 identical unit cells. Note that the negative TL at high frequencies (> 3000 Hz) is due to violation of the assumption that the vibration pattern of a unit cell can be approximated by a piston-like elementary radiator. The TL below approximately 2000 Hz is valid.

Because the TL decreases substantially with increasing number of unit cells, the TL of a unit cell in a waveguide is used in Section 5.2 to design optimal membrane-type acoustic metamaterial noise barriers. The TL of a unit cell in a waveguide is shown (dashed) with the TLs of multi-cell arrays with large numbers of elements in Figure 5.23. Designing ideal unit cells based on their TL in a waveguide will give the lower limit of their performance when arrayed in a noise barrier.

5.1.3.2 Different Unit Cells

Another proposed method of increasing the overall TL of an array of unit cells is by using different configurations of unit cells in the same array. Doing so results in a TL profile that contains multiple dips and peaks corresponding to the number of different configurations used in the array.

Figure 5.24 shows the TLs of 2×2 arrays of baseline and an alternate configuration unit cells in a baffle, and the TL of a 2×2 array with two baseline and two alternate configuration unit cells in an alternating arrangement. The TL curve tends to take the minimum value of the two configurations. Near the TL peaks the frequencies are shifted due to the presence of the adjacent unit cells which have different first resonance and TL peak frequencies.

Typically, the TL of composite walls is computed using a spatially-weighted average of the sound transmission coefficient. The dotted line in Figure 5.24,

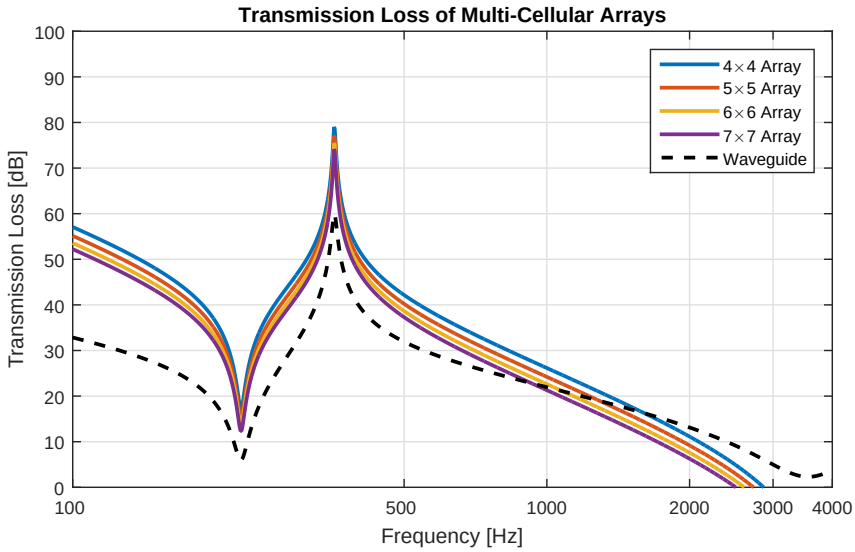

Figure 5.23: Transmission loss of baffled multi-cellular arrays (solid), and a single unit cell in a waveguide (dashed)

Figure 5.24: Transmission loss of baffled multi-cellular arrays with different unit cells. Baseline (blue solid), Alternate (red solid), combined (dashed)

however, shows that it would not be accurate in this situation due to coupling of adjacent unit cells.

5.1.4 Mass Law

Increasing the mass of the attached mass is a good way to improve low-frequency TL, as shown in Figure 5.8. However, doing so also increases the total weight of the unit cell which can be undesirable in situations where weight is a critical design criteria. The TL of the baseline configuration unit cell is plotted along with the mass law TL of a limp panel of equivalent surface density in Figure 5.25. This shows the increase in TL that can be gained by using membrane-type acoustic metamaterial barriers instead of conventional materials. An improvement of more than 40 dB is seen at the TL peak frequency; however, this improvement is confined to a narrow band. In applying the genetic algorithms formulated in Chapter 4, the

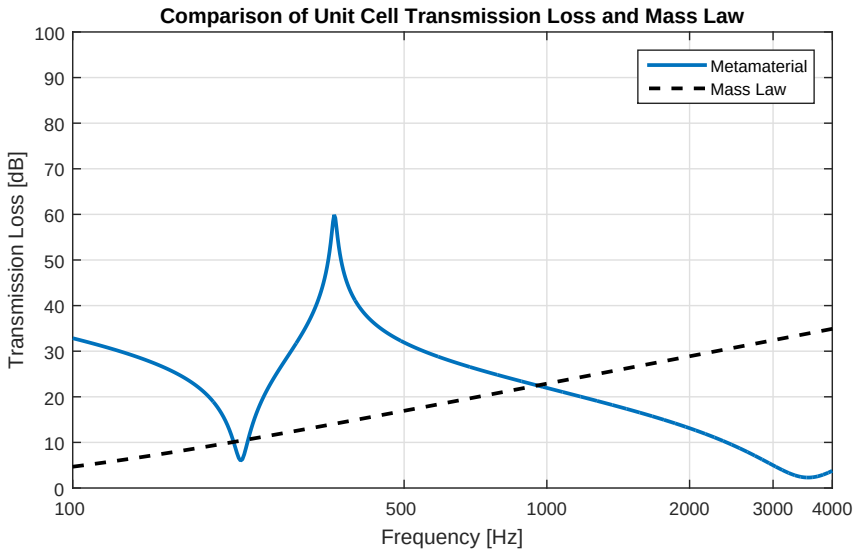

Figure 5.25: Transmission loss of single unit cell in a waveguide (solid) compared to the mass law for a limp panel of equivalent density (dashed)

mass law TL is used as a basis of comparison for designing optimal unit cells while maintaining a light overall weight. The mass law is typically used to characterize the transmission loss of panels above the first panel resonance up to the coincidence frequency, and is therefore an appropriate basis for comparison above the first resonance frequency of a membrane-type acoustic metamaterial unit cell.

5.1.5 Derived Quantities

The quantities derived in Section 2.4 give insight into the physical phenomena that occur when an acoustic wave impinges upon a membrane-type acoustic metamaterial unit cell. These insights can aid the noise control engineer in designing effective noise barriers.

5.1.5.1 Effective Dynamic Mass

The effective dynamic mass is a quantity that defines the operational range of acoustic metamaterials. Anomalous spikes in TL occur when the effective dynamic mass becomes negative, where the membrane average acceleration acts toward the impinging wave. In this frequency range, the unit cell reflects incident energy nearly perfectly.

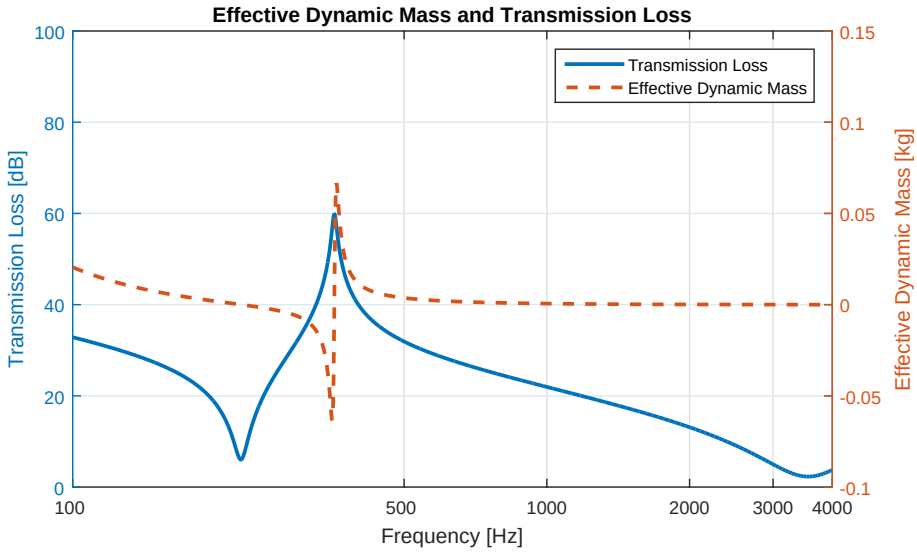

Figure 5.26: TL (solid, left axis) and effective dynamic mass (dashed, right axis) of a single unit cell in a waveguide

Figure 5.26 shows the TL and effective dynamic mass of a membrane-type acoustic metamaterial unit cell in a waveguide calculated using Equation (2.80). The TL peak frequency corresponds to a discontinuity in the effective dynamic mass, where it jumps from negative to positive infinity. The resonance frequencies occur when the effective dynamic mass is zero. As the absolute value of the effective dynamic mass increases, the TL increases proportionally.

Similarly, a double layer of unit cells has a discontinuity in the effective

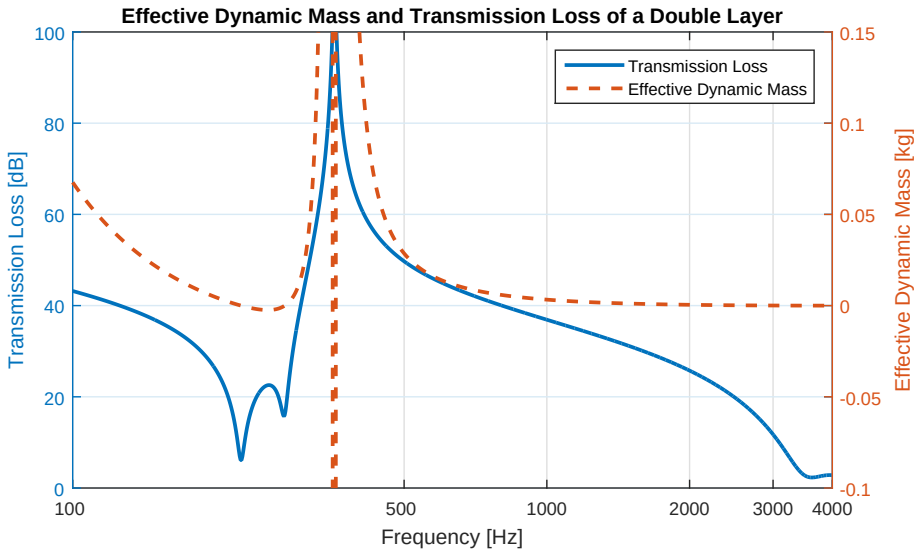

Figure 5.27: TL (solid, left axis) and effective dynamic mass (dashed, right axis) of a double layer of unit cells in a waveguide

dynamic mass at the TL peak frequency, where it jumps from positive to negative and then back to positive, as shown in Figure 5.27. The effective dynamic mass also has a value of zero at an additional frequency just above the first resonance, corresponding to a dip in TL. Zero effective dynamic mass equates to zero net force acting on the membrane, resulting in total reflection of the incident wave.

5.1.5.2 Reflection and Absorption Coefficients

The sound power reflection and absorption coefficients are often used to characterized the influence on the sound field that a material has. For a membrane-type acoustic metamaterial unit cell in a waveguide, the transmission coefficient calculated by Equation (2.17) is used in Equations (2.81) and (2.82) to give the reflection and absorption coefficients, respectively.

Figure 5.28 shows the sound power transmission, reflection, and absorption

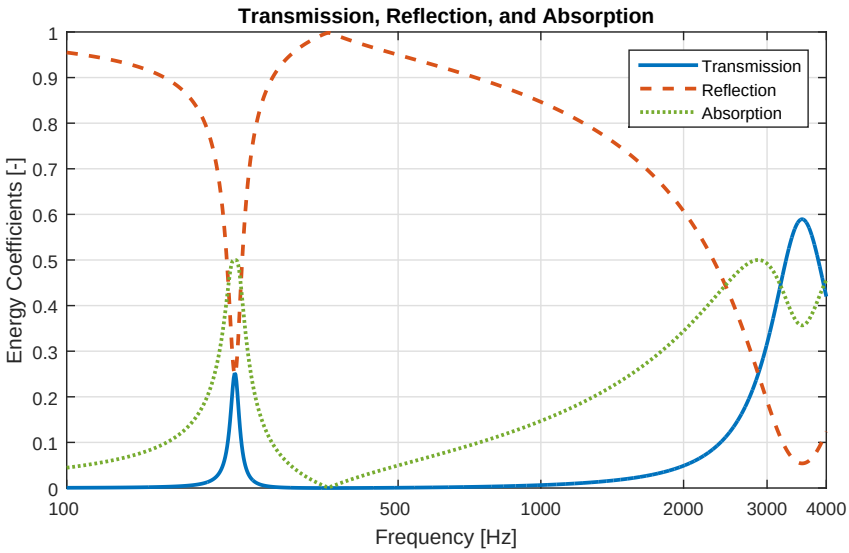

Figure 5.28: Sound power transmission (solid), reflection (dashed), and absorption (dotted) coefficients for a single unit cell in a waveguide

coefficients plotted against frequency. At 356 Hz the reflection coefficient goes to one, while the transmission and absorption coefficients are zero. This corresponds to perfect reflection of the incident wave and the TL peak seen in the transmission loss curves. The resonance at 226 Hz corresponds to maximum displacement of the unit cell leading to peak values of transmission and absorption coefficients of 0.25 and 0.5, respectively. Generally, the absorption coefficient increases with frequency to a maximum value of 0.5. The transmission and reflection coefficients reach local maxima and minima, respectively, at the resonance frequencies of 226 Hz and 3557 Hz.

The transmission, reflection, and absorption coefficients can also be calculated for a double layer of unit cells in a waveguide as shown in Figure 5.29. The results are similar to those of a single unit cell, with the absorption and transmission coefficients peaking near the resonance frequencies of 226 Hz, 279 Hz, and 3622 Hz.

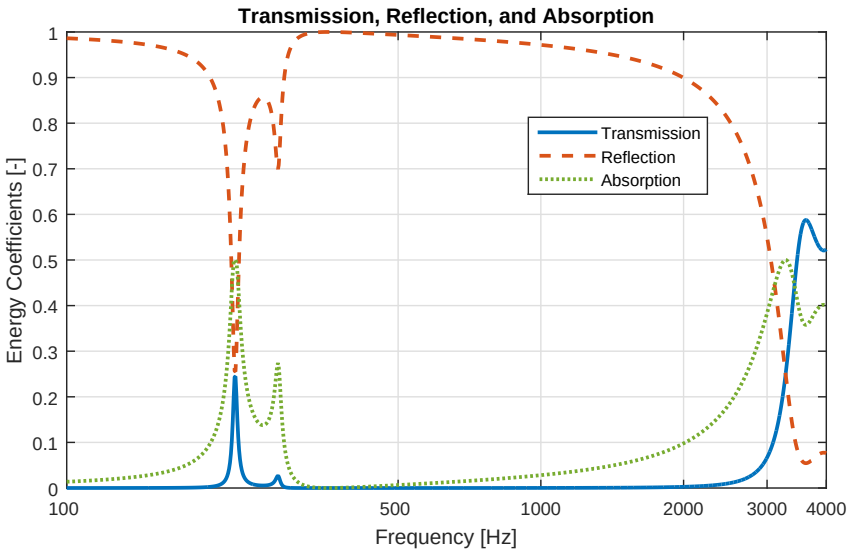

Figure 5.29: Sound power transmission (solid), reflection (dashed), and absorption (dotted) coefficients for a double layer of unit cells in a waveguide

The reflection coefficient is higher over a broad range of frequencies between the first and second resonance.

5.1.5.3 Kinetic and Potential Energy

For active structural vibration control using mechanical or piezoelectric actuators, panel kinetic energy is typically the control quantity [Jin et al. 2009; Kim 1999; Elliott & Nelson 1993]. The TL of a single unit cell in a waveguide is plotted along with its kinetic energy calculated by Equation (2.84) in Figure 5.30. As the panel kinetic energy increases, the TL decreases. The increased vibratory motion couples with the surrounding fluid thereby increasing the transmitted sound power.

Figure 5.31 shows the kinetic energies for both unit cells in a double layer configuration in a waveguide. In general, the kinetic energy of the unit cell on the incident side of the structure is higher. At the resonance frequencies, the kinetic

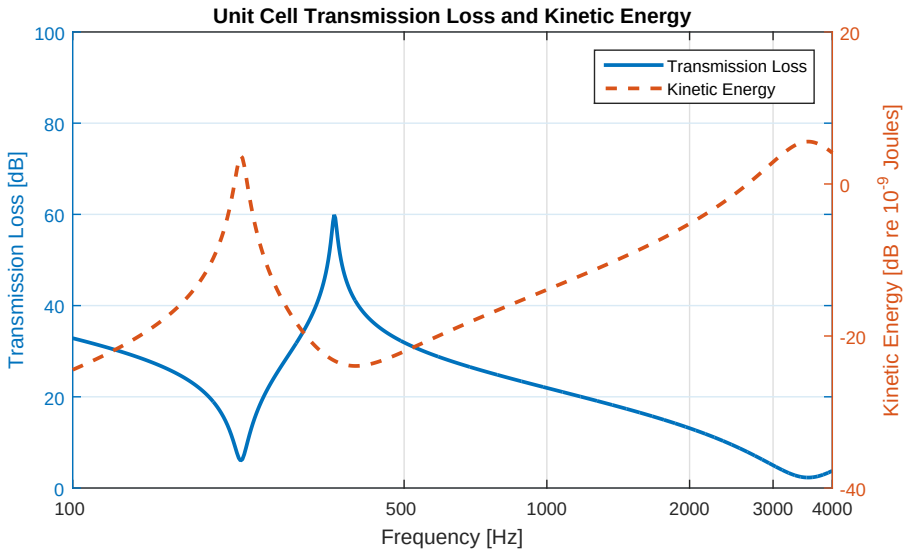

Figure 5.30: Transmission loss (solid) and kinetic energy (dashed) of the baseline configuration unit cell in a waveguide

energies of both unit cells peak, which leads to a low TL.

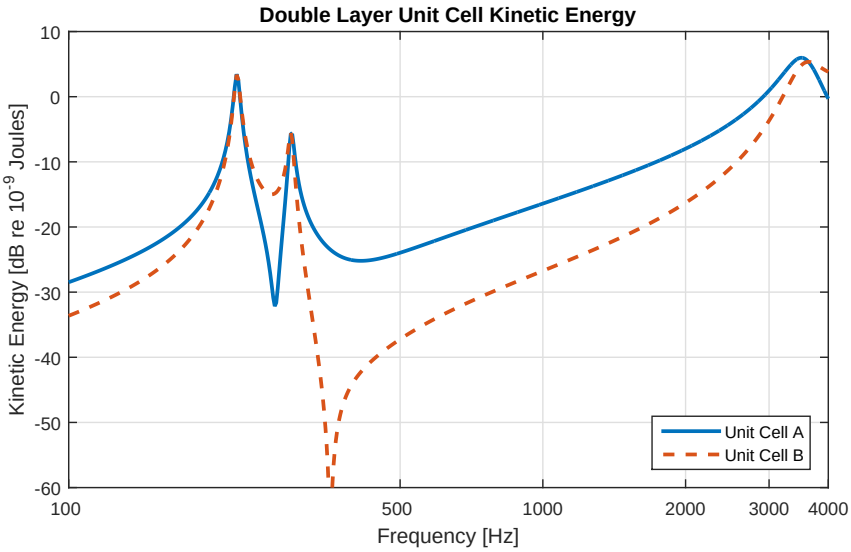

Figure 5.31: Kinetic energy of a double layer of baseline configuration unit cells. Panel A (solid), panel B (dashed)

The acoustic potential energy in the cavity of a double layer of membrane-type acoustic metamaterial unit cells can be a useful quantity in active control using acoustic secondary sources to cancel cavity modes [Jin et al. 2009; Lau & Tang

2006; Kim 1999; Elliott & Nelson 1993]. Figure 5.32 shows the TL of a double layer structure and the cavity potential energy given by Equation (2.86).

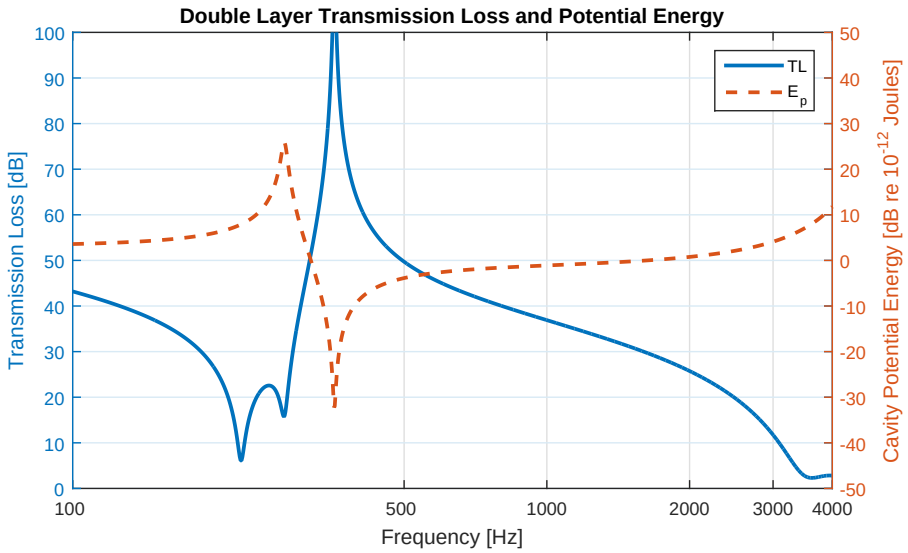

Figure 5.32: Transmission loss (solid) and cavity potential energy (dashed) of a double layer of baseline configuration unit cells

At the TL peak frequency, the acoustic potential energy is a minimum. The additional resonance caused by out-of-phase vibration of the two unit cells causes a peak in potential energy.

5.2 Genetic Algorithm Optimization

By using the computationally efficient dynamic model of a single unit cell in a waveguide formulated using the impedance-mobility approach described in Chapter 2, GAs are applied to find optimal unit cell configurations for a variety of noise control scenarios. Optimal configurations returned from GAs that account for the total mass of the unit cell are presented. Additionally, the GAs are limited such that the optimal designs account for available materials for fabrication.

In the following sections, optimal unit cell configurations for attenuating broadband, octave band, discrete frequency, and multiple discrete frequency noise sources are given. These noise sources correspond to those given in Chapter 4. The optimal configurations returned from GAs when all variables are continuous in the ranges given in Table B.3 and when variables take values of selected materials from Tables B.4 - B.7 are presented. The term "continuous" is used to describe a GA that optimizes values within their respective specified ranges, while "discrete" is used for GAs that select predefined values from a finite set.

5.2.1 Broadband

Using the fitness function given by Equation (4.3) in a continuous GA results in an optimal unit cell configuration for broadband TL from 100 Hz to 4000 Hz that is defined by the parameter values given in Table C.1. This configuration has an overall broadband average TL of 39.0 dB as shown in Figure 5.33.

The layout of the optimal unit cell is given in Figure 5.34, where the gray shaded area is the location of the attached mass, the blue lines indicate the edges of the unit cell, and the limits of the plot area are the maximum allowed unit cell dimensions. By examining Figure 5.34 and Table C.1, some key variables are noted. The GA minimizes the size of the unit cell, which increases the resonance frequencies. The membrane thickness, Young's modulus, and Poisson's ratio are all maximized which maximizes the flexural rigidity of the membrane. This increases the resonance frequencies further. The mass density is nearly maximized while the

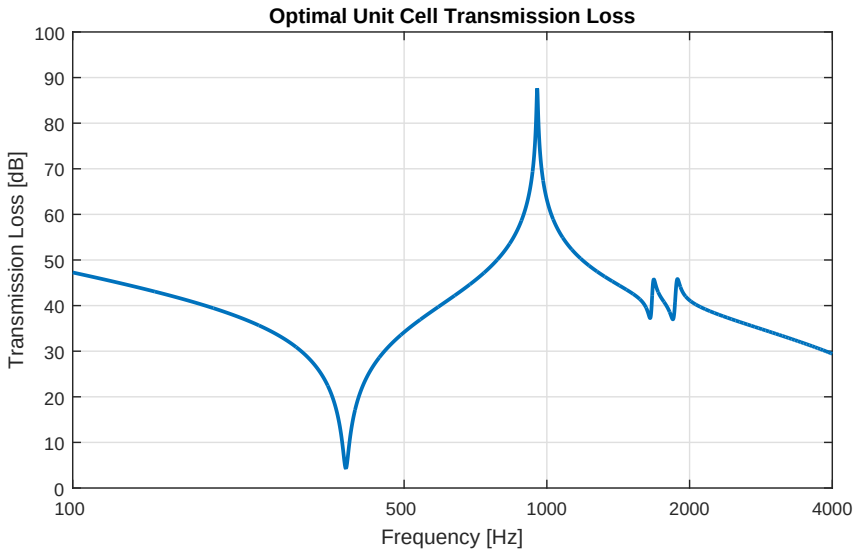

Figure 5.33: TL curve for unit cell optimized for maximum broadband TL using a continuous GA

tension is held at a moderate value to keep the TL peak within the frequency range of interest. The optimal mass location is roughly in the center of the unit cell.

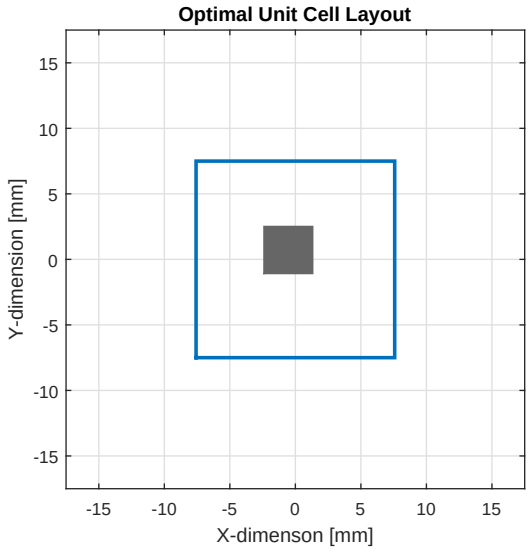

Figure 5.34: Diagram showing unit cell size and mass location of unit cell optimized for maximum broadband TL using a continuous GA

The total weight of the unit cell is considered in the GA by incorporating the mass law TL using the fitness function given by Equation (4.6). The optimal TL is

shown in Figure 5.35 and the design parameter values are given in Table C.2. The fitness score of the optimal unit cell for maximum broadband TL above the mass law is 17.9 dB.

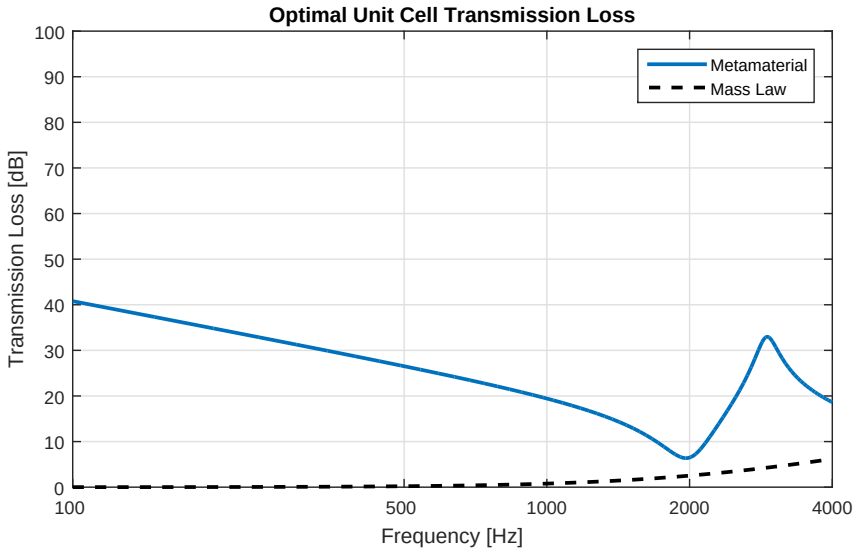

Figure 5.35: TL curve for unit cell optimized for maximum broadband TL above the mass law using a continuous GA

While the TL curve plotted in Figure 5.35 represents the highest TL obtainable using the variable ranges in Table B.3, it should be noted that the majority of the TL curve in the frequency range of interest lies below the first resonance frequency. In this region the TL is dominated by the stiffness of the unit cell mounting structure, which is assumed to be ideally fixed, and is therefore an overestimation of what is feasible in reality [Bies & Hansen 2009].

Figure 5.36 shows the result of the GA optimization scheme operating on a selection of materials shown in Tables B.4 - B.7. The parameter values are shown in Table C.3. The size of the unit cell and the location of the attached mass are free to take any value in the ranges specified in Table B.3. The optimal materials for the

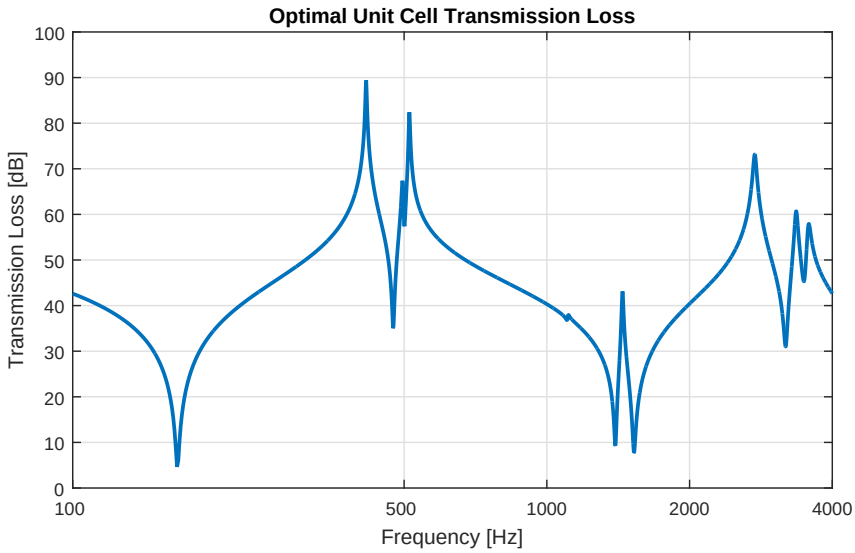

Figure 5.36: TL curve for unit cell optimized for maximum broadband TL using a discrete GA

attached mass and membrane are platinum and PVC, respectively. The size of the unit cell is minimized at 15 mm × 15 mm and the size of the attached mass is maximized at 6 mm × 6 mm × 6 mm. The attached mass is located in the center of the unit cell. The thickest membrane available is chosen. The optimal unit cell configuration has an average TL of 44.8 dB from 100 Hz to 4000 Hz.

5.2.2 Octave Band

For maximum TL in the octave band centered at 250 Hz, a continuous GA with fitness function given by Equation (4.3) with frequency limits of 177 Hz and 355 Hz returns the values given in Table C.4. The optimal TL is plotted in Figure 5.37. The average TL over the 250 Hz octave band is 43.2 dB.

The GA converges on a square unit cell with an attached mass located near the center as shown in Figure 5.38. The combination of the applied tension and size and

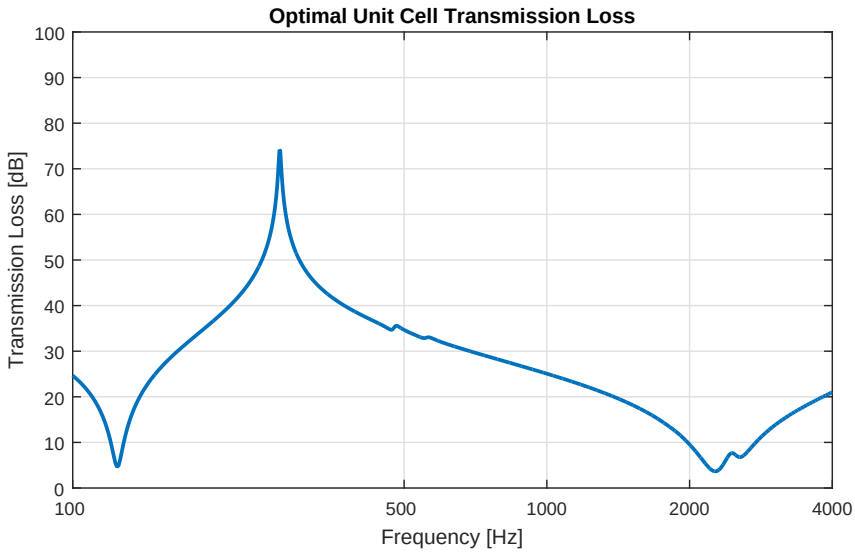

Figure 5.37: TL curve for unit cell optimized for maximum TL in the 250 Hz octave band using a continuous GA

density of the attached mass causes the TL peak to fall in the center of the 250 Hz octave band.

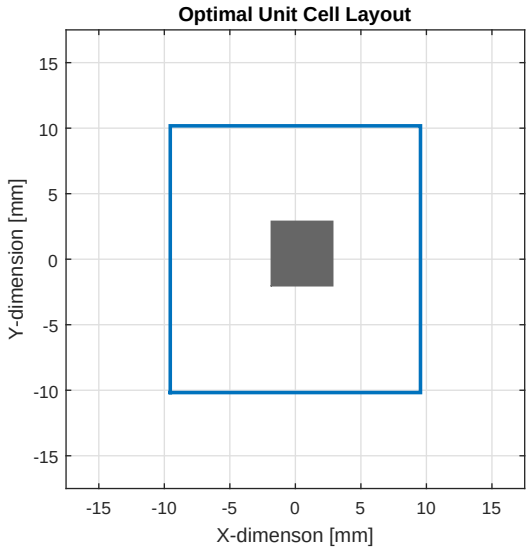

Figure 5.38: Diagram showing unit cell size and mass location of unit cell optimized for maximum TL in the 250 Hz octave band using a continuous GA

A GA with a fitness function that optimizes unit cells for maximum TL above the mass law in the 250 Hz octave band, given by Equation (4.6) with corresponding

limits, generates a set of design parameters that results in a TL of 39.0 dB above the mass law. The TL curve is shown in Figure 5.39 and the parameter values are given in Table C.5. Once again, the GA has maximizes the fitness score by minimizing the mass law TL, rather than maximizing the unit cell TL. The tension and Young's modulus are maximized, pushing the first resonance out of the frequency range of interest.

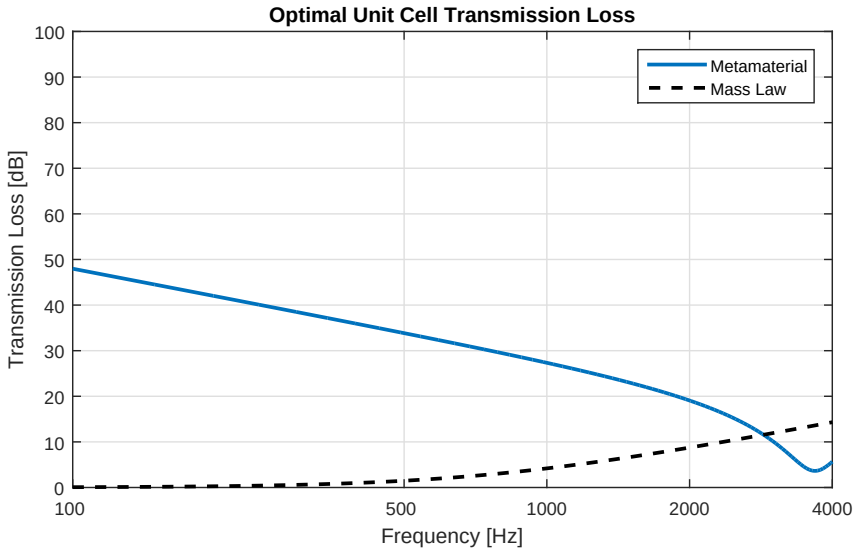

Figure 5.39: TL curve for unit cell optimized for maximum TL above the mass law in the 250 Hz octave band using a continuous GA

The discrete form of the GA returns the values shown in Table C.6 that correspond to an average TL of 50.0 dB in the 250 Hz octave band. The TL is shown in Figure 5.40. The GA chooses polyester and tungsten as the materials for the membrane and mass, respectively. Additionally, the size of the unit cell is minimized and the size of the attached mass is maximized.

Figures D.2 - D.4 in Appendix D show the octave band plots for the three optimal configurations.

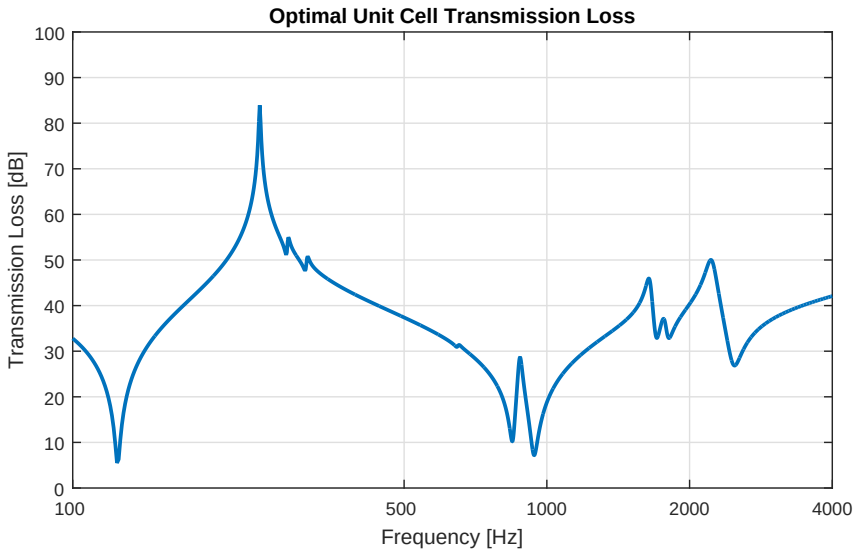

Figure 5.40: TL curve for unit cell optimized for maximum TL in the 250 Hz octave band using a discrete GA

5.2.3 Discrete Frequency

A continuous GA that maximizes the TL at 613 Hz uses the fitness function given by Equation (4.4). The optimal unit cell configuration is defined by the set of parameters in Table C.7. The GA returns a maximum TL at 613 Hz of 70.1 dB. The full TL curve is shown in Figure 5.41.

A diagram of the optimal unit cell configuration is shown in Figure 5.42. The unit cell is roughly square with the attached mass located in the center of the unit cell. The combination of tension, Young's modulus, membrane thickness, and mass density combine to place the TL peak at exactly 613 Hz. It is possible that other combinations of these parameters could result in a TL peak at this frequency; however, this particular combination has the maximum TL amplitude, or very close to it.

The optimal TL above the mass law determined by a GA using the fitness

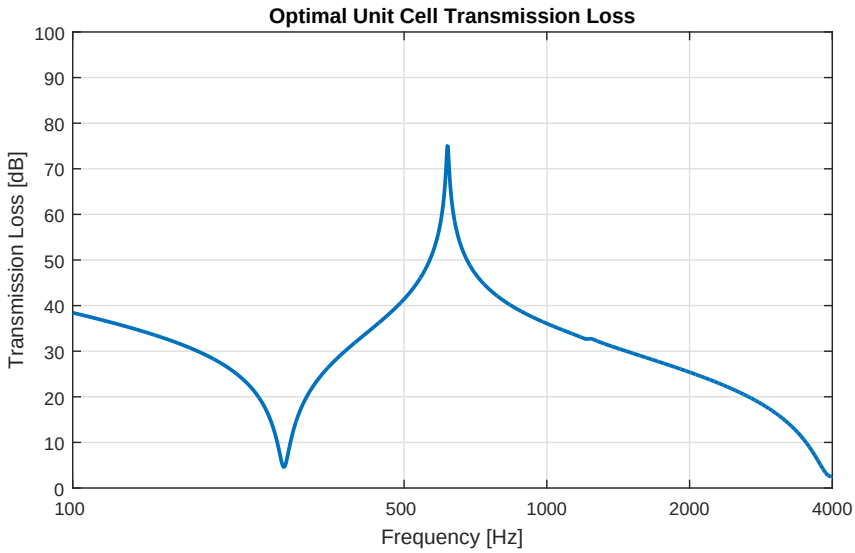

Figure 5.41: TL curve for unit cell optimized for maximum TL at 613 Hz using a continuous GA

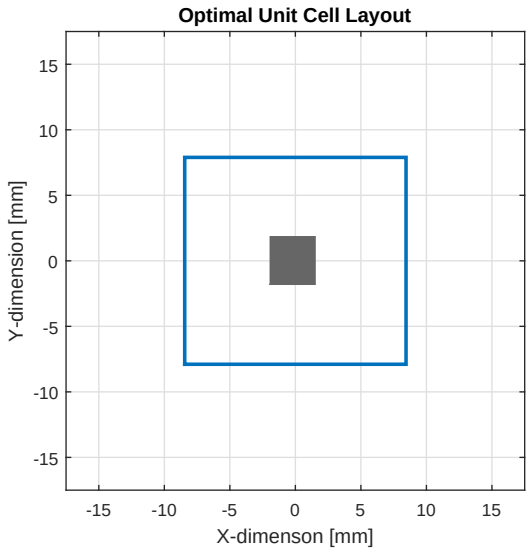

Figure 5.42: Diagram showing unit cell size and mass location of unit cell optimized for maximum TL at 613 Hz using a continuous GA

function given by Equation (4.7) is 45.6 dB above the mass law at 613 Hz. The TL is plotted in Figure 5.43 and the parameter values are given in Table C.8.

Comparing to Figure 5.41, a slight decrease in TL occurs due to the reduction of the total unit cell weight.

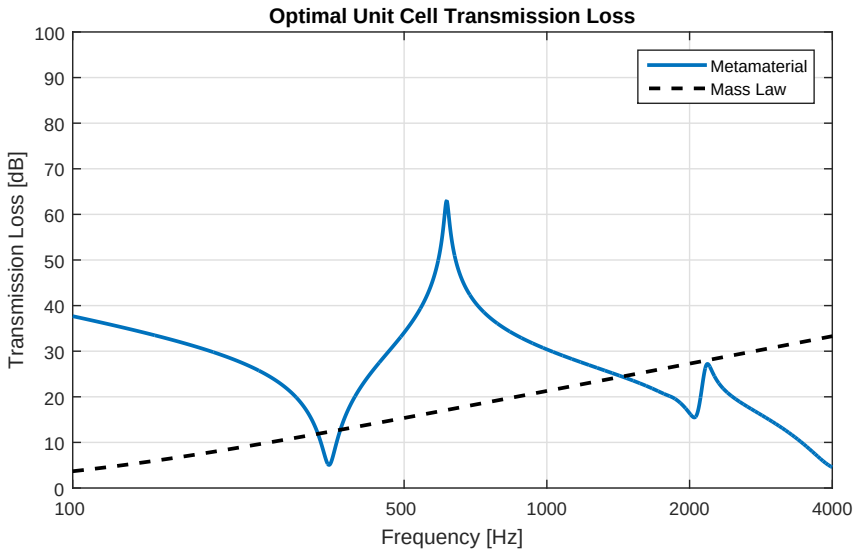

Figure 5.43: TL curve for unit cell optimized for maximum TL above the mass law at 613 Hz using a continuous GA

Using a discrete GA to choose from a selection of materials to maximize TL at 613 Hz results in the TL plotted in Figure 5.44 and design variable values given in Table C.9. The resulting TL at 613 Hz is 76.2 dB. The chosen materials for the membrane and attached mass are polyester and lead, respectively. The width and length of the attached mass are maximized. The size of the unit cell, tension on the membrane, and thickness of the attached mass combine to place the TL peak at 613 Hz.

5.2.4 Multiple Discrete Frequencies

An optimal unit cell configuration to construct a membrane-type acoustic metamaterial noise barrier to attenuate the sound source presented in Section 4.3.4 is designed using a continuous GA operating on the fitness function given by Equation (4.5). The results are plotted in Figure 5.45 and given in Table C.10. The

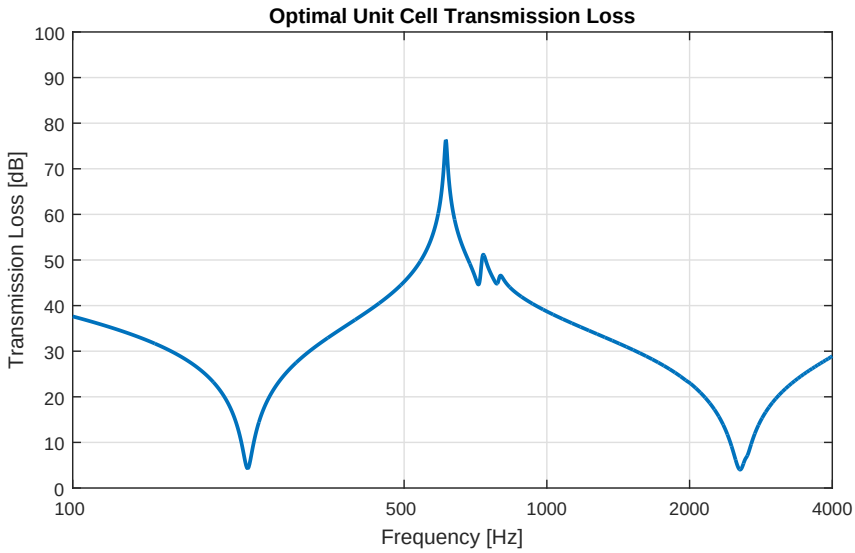

Figure 5.44: TL curve for unit cell optimized for maximum TL at 613 Hz using a discrete GA

maximum fitness function value is 109.8 dB, which corresponds to the weighted sum of TL at 361 Hz, 720 Hz, and 1319 Hz. Their weights are 1, 0.6, and 0.5, respectively.

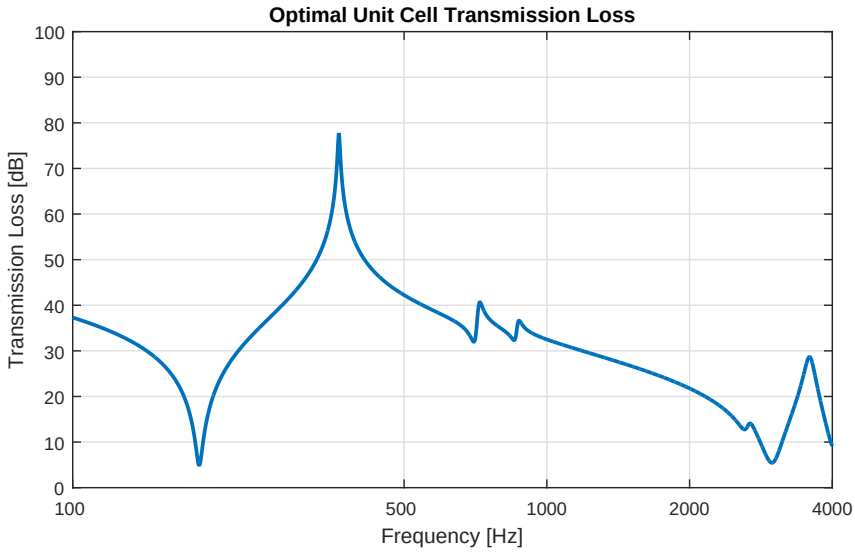

Figure 5.45: TL curve for unit cell optimized for maximum TL for multiple weighted components using a continuous GA

The optimal unit cell size and shape is shown in Figure 5.46. The resulting

configuration has a TL peak near 361 Hz, and a smaller peak near 720 Hz caused by the asymmetric unit cell shape.

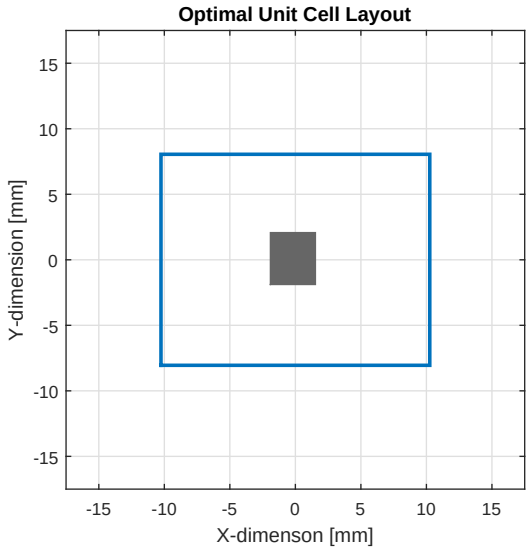

Figure 5.46: Diagram showing unit cell size and mass location of unit cell optimized for maximum TL for multiple weighted components using a continuous GA

Figure 5.47 shows the optimal unit cell transmission loss above the mass law resulting from a continuous GA operating with a fitness function given by Equation (4.8). The optimal parameters are given in Table C.11. Yet again, the GA converges on an optimal solution that minimizes the mass law TL by maximizing the tension and Young's modulus, which forces the first resonance frequency to above 4000 Hz.

A GA using a discrete set of materials to optimize the TL of multiple weighted components returns the values given in Table C.12. The corresponding TL is plotted in Figure 5.48, and has a fitness score of 122 dB. The GA determines that the optimal materials are nylon and platinum for the membrane and attached mass, respectively. The size of the unit cell is minimized, while the size of the attached

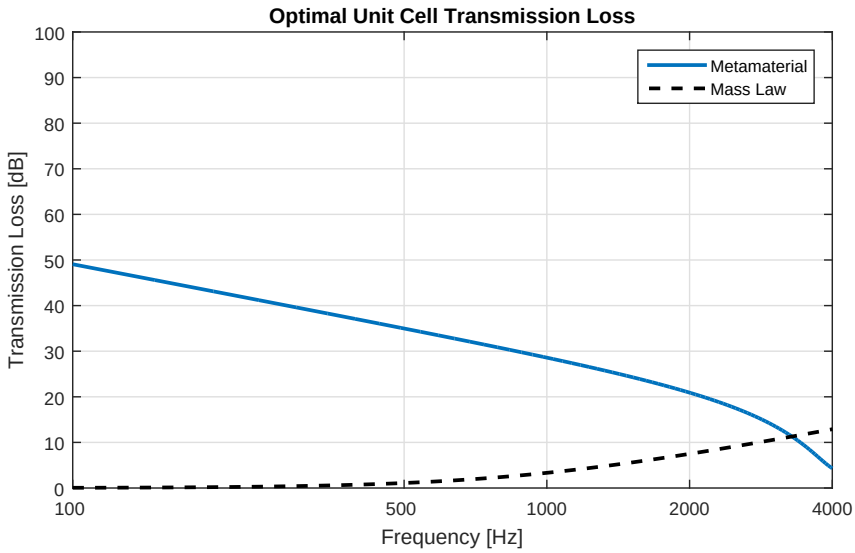

Figure 5.47: TL curve for unit cell optimized for maximum TL above the mass law for multiple weighted components using a continuous GA

mass is maximized. The applied tension is nearly maximized to increase the resonance frequencies.

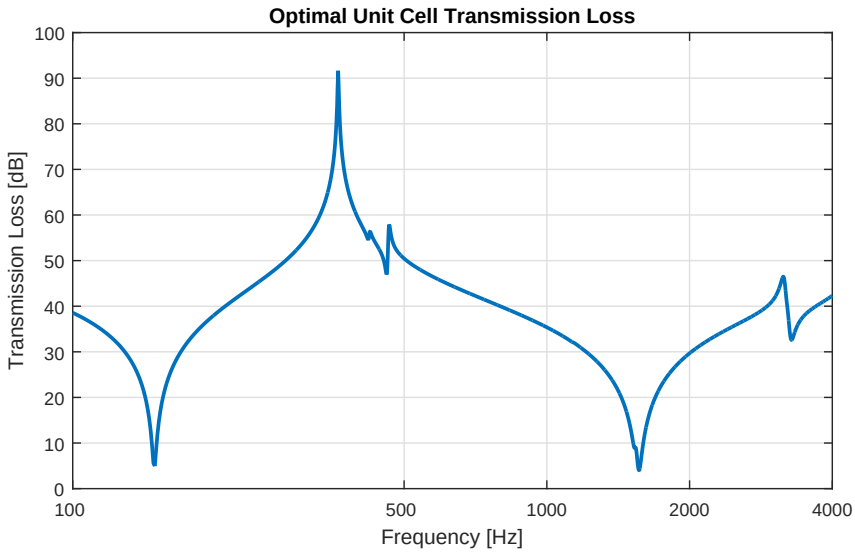

Figure 5.48: TL curve for unit cell optimized for maximum TL for multiple weighted components using a discrete GA

5.3 Concluding Remarks

The above sections illustrate the necessity and ease of applying an optimization scheme using genetic algorithms to membrane-type acoustic metamaterials. In Section 5.1 each design variable is manipulated independently to show the effect on TL, and to provide context to the problem of designing membrane-type acoustic metamaterials to achieve a noise reduction goal. The near-infinite number of possible unit cell configurations makes it practically impossible to design a globally optimal configuration.

GAs provide a tool for the noise control engineer to begin the design of membrane-type acoustic metamaterial noise barriers. Section 5.2 highlights ways that GAs can be used in the design process for a variety of noise reduction goals. By running a GA that allows the design variables to take any value within a specified range, inferences can be made based on the results. Critical design parameters can be identified by noticing which values are maximized or minimized, and which sets of values work co-dependently to achieve a maximum fitness function value. The process can be repeated with a more specific design goal that is reflected in the fitness function. Fitness functions can be altered based on previous results to account for the new information gained, such as when the GA maximizes the overall weight of the unit cell to increase TL. Finally, a discrete GA can be used to determine which out of a set of available materials can be used together to create an optimal unit cell configuration.

Chapter 6

Conclusion and Recommendations for Future Work

6.1 Conclusion

To solve the problem of low frequency noise in environments with strict size and weight limitations, noise control engineers propose membrane-type acoustic metamaterials. Rapid design and optimization, however, cannot occur without efficient and accurate models. This dissertation presents the formulation of computationally efficient dynamic models of membrane-type acoustic metamaterials using the impedance-mobility approach, the verification of their accuracy using a finite element method, and the application of genetic algorithms to optimize their structure.

The impedance-mobility approach is used to model membrane-type acoustic metamaterial unit cells in a waveguide and in a baffle. By expanding the

displacement of unit cell as a summation of normal modes and considering the coupling to the surrounding fluid, the vibratory response is determined. The models are expanded to larger systems of layers of unit cells in a waveguide by coupling two unit cells and a separating acoustic cavity. The response of arrays of unit cells in a baffle is found two ways; by considering the coupled acoustic pressure due to adjacent unit cells, and by neglecting the coupling entirely. Formulas for transmission loss, reflection and absorption coefficients, effective mass density, panel kinetic energy, and cavity potential energy are presented. The flexibility of these models enable expansion to larger systems comprised of metamaterials, or conventional materials. This method is also valid for higher frequencies when more modes are included in the expansion of unit cell displacement and cavity pressure, with the caveat that internal resonances in the attached mass can cause inaccuracy with a large number of modes.

The accuracy of TL calculated using the impedance-mobility approach is verified by comparison to FEM models. In general the models agree very well with each other, and, by extension through previous work, to experimental results. The assumptions of the impedance-mobility models are validated, and generalizations to unit cells of different shapes are made. The results of the analysis in Chapters 3 and 5 indicate that the primary design variables responsible for the TL profile are the applied tension on the membrane and the magnitude of the attached mass. For unit cells of equal area, the shape of the unit cell does not significantly impact the TL. In designing membrane-type acoustic metamaterial noise barriers, the shape of the unit cell can be determined by external factors, such as ease of fabrication. For

regular-polygonal unit cell shapes with centrally-located attached masses, the impedance-mobility model of a square unit cell with an equivalent area can be used to accurately predict the TL response.

The process of design is greatly facilitated by optimization schemes capable of sorting through the myriad possible configurations of unit cells. The GAs presented in Chapter 4 are used in several ways to serve this purpose. First, the design criteria are determined and a fitness function to quantify the degree of success is formulated. Second, the GA is used to identify the key design variables by considering each one as capable of taking any value in a predefined range. This enables the user to see which variables are maximized or minimized, and which variables work in tandem to determine the response of the structure. Third, the fitness function or design variable ranges are adjusted according to the information gained from the output of the first GA. Lastly, the GA is implemented such that it chooses from a finite set of available materials that can be used in fabrication.

The fitness functions and material choices used in this dissertation are intended as guidelines, and are by no means the only possible choices. The process described above is a flexible framework that allows noise control engineers to incorporate their experience into the process. While it is possible to design an *adequate* noise barrier using a trial and error method with the GUI implementation of the impedance-mobility model, a process involving GAs will find an *optimal* solution.

The work in this dissertation has lead to several novel contributions to the field. An impedance mobility approach is used to model the transmission loss of a vibrating structure in a waveguide, and in a baffle. Previous work has only

considered the transmission *into* a cavity from a flexible barrier, not *through* a barrier or through a pair of barriers and cavity [Jin et al. 2009; Kim & Brennan 1999]. The response of a unit cell of a membrane-type acoustic metamaterial in a baffle has not been previously studied. The impedance-mobility model is expanded to consider multiple unit cells layered in series, and arrayed in a baffle. To date no other analytical formulation of an array of unit cells has been presented. Genetic algorithms are used to find the optimal unit cell configurations for various noise control criteria.

6.2 Recommendations for Future Work

Future work should exploit the flexible formulation of the impedance-mobility approach, which is ideal for expansion to larger and more complex structural-acoustic systems. In addition to membrane-type acoustic metamaterials, other noise control devices can be incorporated in layers. Micro-perforated panels (MPPs) are an ideal candidate since they can be characterized in a manner that is similar to the impedance-mobility approach [Bravo et al. 2012]. MPPs can also be tuned to operate at a higher frequency range than that of membrane-type acoustic metamaterials resulting in a broadband noise barrier. Other conventional materials such as mass-loaded vinyl or fiberglass can be combined with membrane-type acoustic metamaterials to create noise barriers that are effective over a wide frequency range.

Genetic algorithms can also be used to optimize noise barriers that consist of

multiple conventional or metamaterial components. Continuous GAs can be used to find optimal parameter values to optimize each substructure, and discrete GAs can be used to pick the best combination of pre-fabricated components.

The impedance-mobility approach can be expanded to model the TL of double layers of arrayed unit cells. The two layers could consist of multiple sets of unit cells and cavities, or two arrays with a common cavity.

Another application of membrane-type acoustic metamaterials is absorption of incident sound. The impedance-mobility models formulated in Chapter 2 are primarily concerned with sound transmission through a structure, but can easily be adapted to consider absorption. Ma et al. [2014] proposed a structure with a unit cell consisting of a membrane carrying an attached mass suspended over a rigid-walled cavity as shown in Figure 6.1. This structure is capable of perfect absorption of an incident wave in a specific frequency band.

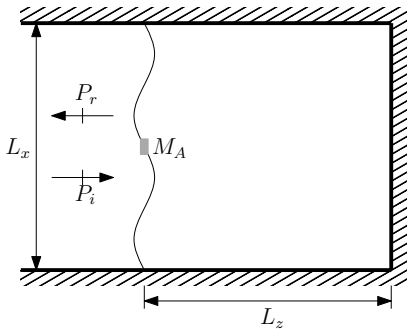

Figure 6.1: Cross-section of a membrane-type acoustic metamaterial absorber

Further experimental verification of the models is also required. Small-scale testing of unit cells in a plane-wave tube can ensure that optimal unit cell configurations perform as intended. Large-scale measurement of membrane-type acoustic metamaterial barriers is also needed.

Bibliography

ANSI (2004). *ANSI S1.11: Specification for Octave, Half-Octave, and Third Octave Band Filter Sets*. Standard S1.11. American National Standards Institute.

ASHRAE (2011). "ASHRAE Handbook: HVAC Applications". Chap. 48 Noise and Vibration Control.

D. Bies & C. Hansen (2009). *Engineering Noise Control: Theory and Practice*. Taylor & Francis.

T. Bravo, C. Maury, & C. Pinhède (2012). "Sound absorption and transmission through flexible micro-perforated panels backed by an air layer and a thin plate". *The Journal of the Acoustical Society of America* 131.5, pp. 3853–3863.

C. T. Chan, J. Li, & K. H. Fung (2006). "On extending the concept of double negativity to acoustic waves". *Journal of Zhejiang University Science A* 7.1, pp. 24–28.

J.-D. Chazot & J.-L. Guyader (2007). "Prediction of transmission loss of double panels with a patch-mobility method". *The Journal of the Acoustical Society of America* 121.1, pp. 267–278.

H. Chen & C. Chan (2007). "Acoustic cloaking in three dimensions using acoustic metamaterials". *Applied Physics Letters* 91.18, p. 183518.

Y. Chen, G. Huang, X. Zhou, G. Hu, & C.-T. Sun (2014a). "Analytical coupled vibroacoustic modeling of membrane-type acoustic metamaterials: Membrane model". *The Journal of the Acoustical Society of America* 136.3, pp. 969–979.

Y. Chen, G. Huang, X. Zhou, G. Hu, & C.-T. Sun (2014b). "Analytical coupled vibroacoustic modeling of membrane-type acoustic metamaterials: Plate model". *The Journal of the Acoustical Society of America* 136.6, pp. 2926–2934.

Y. Cheng, F. Yang, J. Y. Xu, & X. J. Liu (2008). "A multilayer structured acoustic cloak with homogeneous isotropic materials". *Applied Physics Letters* 92.15, p. 151913.

A. Climente, D. Torrent, & J. Sánchez-Dehesa (2010). "Sound focusing by gradient index sonic lenses". *Applied Physics Letters* 97.10, p. 104103.

COMSOL Multiphysics (2012). "COMSOL Multiphysics User Guide (Version 4.3 a)".

R. V. Craster & S. Guenneau (2012). *Acoustic Metamaterials: Negative Refraction, Imaging, Lensing and Cloaking*. Vol. 166. Springer.

S. Das (2009). "Metamaterials arrive in cellphones". *IEEE Spectrum*.

K. A. De Jong & W. M. Spears (1992). "A formal analysis of the role of multi-point crossover in genetic algorithms". *Annals of mathematics and Artificial intelligence* 5.1, pp. 1–26.

K. Deb (1999). "An introduction to genetic algorithms". *Sadhana* 24.4-5, pp. 293–315.

C.-L. Ding & X.-P. Zhao (2011). "Multi-band and broadband acoustic metamaterial with resonant structures". *Journal of Physics D: Applied Physics* 44.21, p. 215402.

M. Dorigo, V. Maniezzo, & A. Colorni (1996). "Ant system: optimization by a colony of cooperating agents". *Systems, Man, and Cybernetics, Part B: Cybernetics, IEEE Transactions on* 26.1, pp. 29–41.

E. Dowell, G. Gorman III, & D. Smith (1977). "Acoustoelasticity: general theory, acoustic natural modes and forced response to sinusoidal excitation, including comparisons with experiment". *Journal of Sound and Vibration* 52.4, pp. 519–542.

E. Elbeltagi, T. Hegazy, & D. Grierson (2005). "Comparison among five evolutionary-based optimization algorithms". *Advanced engineering informatics* 19.1, pp. 43–53.

S. J. Elliott (1999). "Down with noise". *IEEE Spectrum* 36.6, pp. 54–61.

S. J. Elliott & P. A. Nelson (1993). "Active noise control". *Signal Processing Magazine, IEEE* 10.4, pp. 12–35.

F. A. Everest (2001). *The Master Handbook of Acoustics*. Vol. 4. McGraw-Hill New York.

F. J. Fahy & P. Gardonio (2007). *Sound and Structural Vibration: Radiation, Transmission and Response*. Academic Press.

F. Fahy & J. Walker (2004). *Advanced Applications in Acoustics, Noise and Vibration*. CRC Press.

N. Fang, H. Lee, C. Sun, & X. Zhang (2005). "Sub–diffraction-limited optical imaging with a silver superlens". *Science* 308.5721, pp. 534–537.

N. Fang, D. Xi, J. Xu, M. Ambati, W. Srituravanich, C. Sun, & X. Zhang (2006). "Ultrasonic metamaterials with negative modulus". *Nature Materials* 5.6, pp. 452–456.

M. J. Freire, L. Jelinek, R. Marques, & M. Lapine (2010). "On the applications of μr=-1 metamaterial lenses for magnetic resonance imaging". *Journal of Magnetic Resonance* 203.1, pp. 81–90.

P. Gardonio & M. Brennan (2002). "On the origins and development of mobility and impedance methods in structural dynamics". *Journal of Sound and Vibration* 249.3, pp. 557–573.

D. E. Goldberg & K. Deb (1991). "A comparative analysis of selection schemes used in genetic algorithms". *Foundations of Genetic Algorithms.*

S. Guenneau, A. Movchan, G. Pétursson, & S. A. Ramakrishna (2007). "Acoustic metamaterials for sound focusing and confinement". *New Journal of Physics* 9.11, p. 399.

R. L. Haupt (1995). "An introduction to genetic algorithms for electromagnetics". *Antennas and Propagation Magazine, IEEE* 37.2, pp. 7–15.

K. M. Ho, C. K. Cheng, Z. Yang, X. Zhang, & P. Sheng (2003). "Broadband locally resonant sonic shields". *Applied Physics Letters* 83.26, pp. 5566–5568.

J. H. Holland (1975). *Adaptation in Natural and Artificial Systems: An Introductory Analysis with Applications to Biology, Control, and Artificial Intelligence.* U Michigan Press.

S. James (2005). *Defining the Cockpit Noise Hazard, Aircrew Hearing Damage Risk and the Benefits Active Noise Reduction Headsets can Provide*. Tech. rep. DTIC Document.

Z. H. Jiang, J. A. Bossard, X. Wang, & D. H. Werner (2011). "Synthesizing metamaterials with angularly independent effective medium properties based on an anisotropic parameter retrieval technique coupled with a genetic algorithm". *Journal of Applied Physics* 109.1, p. 013515.

G. Jin, Z. Liu, & T. Yang (2009). "Active control of sound transmission into an acoustic cavity surrounded by more than one flexible plate". *Noise Control Engineering Journal* 57.3, pp. 210–220.

J. Kennedy (1997). "The particle swarm: social adaptation of knowledge". *Evolutionary Computation, 1997., IEEE International Conference on*. IEEE, pp. 303–308.

S. M. Kim (1999). "Active control of sound in structural-aocustic systems". PhD Thesis. University of Southampton.

S. M. Kim & M. J. Brennan (1999). "A compact matrix formulation using the impedance and mobility approach for the analysis of structural-acoustic systems". *Journal of Sound and Vibration* 223.1, pp. 97–113.

L. E. Kinsler, A. R. Frey, A. B. Coppens, & J. V. Sanders (2000). *Fundamentals of Acoustics*. 4th ed. Wiley.

O. Kopmaz & S. Telli (2002). "Free vibrations of a rectangular plate carrying a distributed mass". *Journal of Sound and Vibration* 251.1, pp. 39–57.

F. Langfeldt, W. Gleine, & O. von Estorff (2015). "Analytical model for low-frequency transmission loss calculation of membranes loaded with arbitrarily shaped masses". *Journal of Sound and Vibration* 349, pp. 315–329.

S. Lau & S. Tang (2001). "Sound fields in a rectangular enclosure under active sound transmission control". *The Journal of the Acoustical Society of America* 110.2, pp. 925–938.

S. Lau & S. Tang (2006). "Sound attenuation pattern in a rectangular enclosure under potential-energy based active sound transmission control". *INTER-NOISE and NOISE-CON Congress and Conference Proceedings*. Vol. 2006. 5. Institute of Noise Control Engineering, pp. 2582–2591.

J. D. Leatherwood (1987). *Annoyance Response to Simulated Advanced Turboprop Aircraft Interior Noise Containing Tonal Beats*. Tech. rep. 2689. NASA.

A. W. Leissa (1969). *Vibration of Plates*. Tech. rep. DTIC Document.

H. Leventhall (2004). "Low frequency noise and annoyance". *Noise & Health* 6.23, pp. 59–72.

D. Li, L. Zigoneanu, B.-I. Popa, & S. A. Cummer (2012). "Design of an acoustic metamaterial lens using genetic algorithms". *The Journal of the Acoustical Society of America* 132.4, pp. 2823–2833.

J. Li & C. T. Chan (2004). "Double-negative acoustic metamaterial". *Physical Review E* 70.5, p. 055602.

J. Li, Z. Liu, & C. Qiu (2006). "Negative refraction imaging of acoustic waves by a two-dimensional three-component phononic crystal". *Physical Review B* 73.5, p. 054302.

P. Li, S. Yao, X. Zhou, G. Huang, & G. Hu (2014). "Effective medium theory of thin-plate acoustic metamaterials". *The Journal of the Acoustical Society of America* 135.4, pp. 1844–1852.

X.-F. Li, X. Ni, L. Feng, M.-H. Lu, C. He, & Y.-F. Chen (2011). "Tunable unidirectional sound propagation through a sonic-crystal-based acoustic diode". *Physical Review Letters* 106.8, p. 084301.

Z. Liu, X. Zhang, Y. Mao, Y. Y. Zhu, Z. Yang, C. T. Chan, & P. Sheng (2000). "Locally resonant sonic materials". *Science* 289.5485, pp. 1734–1736.

M. Long (2006). *Architectural Acoustics*. Academic Press.

K. Lu, J. H. Wu, D. Guan, N. Gao, & L. Jing (2016). "A lightweight low-frequency sound insulation membrane-type acoustic metamaterial". *AIP Advances* 6.2, p. 025116.

G. Ma, M. Yang, S. Xiao, Z. Yang, & P. Sheng (2014). "Acoustic metasurface with hybrid resonances". *Nature Materials* 13.9, pp. 873–878.

MathWorks (2016). *MathWorks MATLAB Runtime*. URL: `http://www.mathworks.com/products/compiler/mcr/` (visited on 03/18/2016).

L. Maxit, C. Yang, L. Cheng, & J.-L. Guyader (2012). "Modeling of micro-perforated panels in a complex vibro-acoustic environment using patch transfer function approach". *The Journal of the Acoustical Society of America* 131.3, pp. 2118–2130.

H. Meng, J. Wen, H. Zhao, & X. Wen (2012). "Optimization of locally resonant acoustic metamaterials on underwater sound absorption characteristics". *Journal of Sound and Vibration* 331.20, pp. 4406–4416.

P. Merz & B. Freisleben (1997). "A genetic local search approach to the quadratic assignment problem". *Proceedings of the 7th international conference on genetic algorithms*, pp. 1–1.

M. Mitchell (1998). *An Introduction To Genetic Algorithms*. MIT Press.

H. Møller & C. S. Pedersen (2011). "Low-frequency noise from large wind turbines". *The Journal of the Acoustical Society of America* 129.6, pp. 3727–3744.

S. More & P. Davies (2010). "Human responses to the tonalness of aircraft noise". *Noise Control Engineering Journal* 58.4, pp. 420–440.

C. J. Naify, C. M. Chang, G. McKnight, & S. R. Nutt (2010). "Transmission loss and dynamic response of membrane-type locally resonant acoustic metamaterials". *Journal of Applied Physics* 108.11, p. 114905.

C. J. Naify, C. M. Chang, G. McKnight, & S. R. Nutt (2011a). "Transmission loss of membrane-type acoustic metamaterials with coaxial ring masses". *Journal of Applied Physics* 110.12, p. 124903.

C. J. Naify, C. M. Chang, G. McKnight, & S. R. Nutt (2012). "Scaling of membrane-type locally resonant acoustic metamaterial arrays". *Journal of the Acoustical Society of America* 132.4, pp. 2784–2792.

C. J. Naify, C. M. Chang, G. McKnight, F. Scheulen, & S. Nutt (2011b). "Membrane-type metamaterials: Transmission loss of multi-celled arrays". *Journal of Applied Physics* 109.10, p. 104902.

C. J. Naify, C. Huang, M. Sneddon, & S. Nutt (2011c). "Transmission loss of honeycomb sandwich structures with attached gas layers". *Applied Acoustics* 72.2, pp. 71–77.

M. Ouisse, L. Maxit, C. Cacciolati, & J.-L. Guyader (2005). "Patch transfer functions as a tool to couple linear acoustic problems". *Journal of vibration and Acoustics* 127.5, pp. 458–466.

J. B. Pendry, A. J. Holden, W. J. Stewart, & I. Youngs (1996). "Extremely low frequency plasmons in metallic mesostructures". *Physical Review Letters* 76.25, p. 4773.

J. Pendry & J. Li (2008). "An acoustic metafluid: realizing a broadband acoustic cloak". *New Journal of Physics* 10.11, p. 115032.

J. B. Pendry (2000). "Negative refraction makes a perfect lens". *Physical Review Letters* 85.18, p. 3966.

E. E. Ryherd & L. M. Wang (2008). "Implications of human performance and perception under tonal noise conditions on indoor noise criteria". *The Journal of the Acoustical Society of America* 124.1, pp. 218–226.

E. A. G. Shaw & G. J. Thiessen (1962). "Acoustics of circumaural earphones". *The Journal of the Acoustical Society of America* 34.9A.

P. Sheng, J. Mei, Z. Liu, & W. Wen (2007). "Dynamic mass density and acoustic metamaterials". *Physica B: Condensed Matter* 394.2, pp. 256–261.

L. W. T. Silva, V. F. Barros, & S. G. Silva (2014). "Genetic algorithm with maximum-minimum crossover (GA-MMC) applied in optimization of radiation

pattern control of phased-array radars for rocket tracking systems". *Sensors* 14.8, pp. 15113–15141.

D. R. Smith, J. B. Pendry, & M. C. K. Wiltshire (2004). "Metamaterials and negative refractive index". *Science* 305.5685, pp. 788–792.

S. D. Snyder & N. Tanaka (1995). "Calculating total acoustic power output using modal radiation efficiencies". *The Journal of the Acoustical Society of America* 97.3, pp. 1702–1709.

H. Tian, X. Wang, & Y.-h. Zhou (2014). "Theoretical model and analytical approach for a circular membrane–ring structure of locally resonant acoustic metamaterial". *Applied Physics A* 114.3, pp. 985–990.

N. Totaro & J.-L. Guyader (2012). "Efficient positioning of absorbing material in complex systems by using the Patch Transfer Function method". *Journal of Sound and Vibration* 331.13, pp. 3130–3143.

V. G. Veselago (1968). "The electrodynamics of substances with simultaneously negative values of ϵ and μ". *Physics-Uspekhi* 10.4, pp. 509–514.

C. E. Wallace (1972). "Radiation resistance of a rectangular panel". *The Journal of the Acoustical Society of America* 51.3B, pp. 946–952.

R. Wang, B. Yuan, G. Wang, & F. Yi (2007). "Efficient design of directive patch antennas in mobile communications using metamaterials". *International Journal of Infrared and Millimeter Waves* 28.8, pp. 639–649.

E. C. Wester, X. Brémaud, & B. Smith (2009). "Meta-material sound insulation". *Building Acoustics* 16.1, pp. 21–30.

J. F. Wilby (1996). "Aircraft interior noise". *Journal of Sound and Vibration* 190.3, pp. 545–564.

Z. Yang, H. M. Dai, N. H. Chan, G. C. Ma, & P. Sheng (2010). "Acoustic metamaterial panels for sound attenuation in the 50–1000 Hz regime". *Applied Physics Letters* 96.4, p. 041906.

Z. Yang, J. Mei, M. Yang, N. Chan, & P. Sheng (2008). "Membrane-type acoustic metamaterial with negative dynamic mass". *Physical Review Letters* 101.20, p. 204301.

Y. Zhang, J. Wen, Y. Xiao, X. Wen, & J. Wang (2012). "Theoretical investigation of the sound attenuation of membrane-type acoustic metamaterials". *Physics Letters A* 376.17, pp. 1489–1494.

Y. Zhang, J. Wen, H. Zhao, D. Yu, L. Cai, & X. Wen (2013). "Sound insulation property of membrane-type acoustic metamaterials carrying different masses at adjacent cells". *Journal of Applied Physics* 114.6, p. 063515.

H.-G. Zhao, Y.-Z. Liu, J.-H. Wen, D.-L. Yu, G. Wang, & X.-S. Wen (2006). "Sound absorption of locally resonant sonic materials". *Chinese Physics Letters* 23.8, p. 2132.

H.-G. Zhao, Y.-Z. Liu, J.-H. Wen, D.-L. Yu, & X.-S. Wen (2007). "Tri-component phononic crystals for underwater anechoic coatings". *Physics Letters A* 367.3, pp. 224–232.

O. C. Zienkiewicz, R. L. Taylor, O. C. Zienkiewicz, & R. L. Taylor (1977). *The Finite Element Method*. Vol. 3. McGraw-Hill London.

Appendix A

Modes and Modal Radiation Efficiencies

The impedance-mobility formulation described in Chapter 2 uses a mode superposition method to describe the vibratory motion of the unit cell. To assist in understanding this method, this appendix describes the modes of vibration and natural frequencies of a simply supported membrane with and without bending stiffness. The modes and natural frequencies of a rigid-walled cavity are explained to elucidate the impedance-mobility formulation for a double layer of membrane-type acoustic metamaterial unit cells. The modal radiation efficiencies used to calculate the sound power radiated by a unit cell in a rigid baffle are also explained here.

A.1 Vibration Modes and Natural Frequencies of a Simply Supported Membrane

A.1.1 Modeshape Function

The equation of motion for a membrane without external forces is

$$\rho_s \frac{\partial^2 w}{\partial t^2} - T\nabla^2 w = 0, \tag{A.1}$$

where w is the out-of-plane deflection, ρ_s is the surface density, and T is the applied tension. By applying simply supported boundary conditions for a membrane of dimensions $L_x \times L_y$

$$w(0, y) = w(L_x, y) = w(x, 0) = w(x, L_y) = 0,$$

and using separation of variables, it can be shown that the mode functions are sinusoids given by

$$\phi_m(x, y) = 2 \sin\left(\frac{m_1 \pi x}{L_x}\right) \sin\left(\frac{m_2 \pi y}{L_y}\right), \tag{A.2}$$

where the structural modes are $m = (m_1, m_2)$.

A.1.2 Natural Frequencies

The wave numbers are restricted to values of $k_x = m_1\pi/L_x$ and $k_y = m_2\pi/L_y$, which restricts the natural frequencies to

$$\omega_m = \sqrt{\frac{T}{\rho_s}}\sqrt{\left(\frac{m_1\pi}{Lx}\right)^2 + \left(\frac{m_2\pi}{L_y}\right)^2}, \tag{A.3}$$

where $m = 1, 2, ...M$

A.1.3 Membrane Stiffness

Incorporating membrane bending stiffness into Equation (A.1) gives

$$\rho_s\frac{\partial^2 w}{\partial t^2} + D\nabla^4 w - T\nabla^2 w = 0, \tag{A.4}$$

with corresponding natural frequencies

$$\omega_m = \sqrt{\frac{T}{\rho_s}}\sqrt{\left(\frac{m_1\pi}{L_x}\right)^2 + \left(\frac{m_2\pi}{L_y}\right)^2} + \sqrt{\frac{D}{\rho_s}}\left[\left(\frac{m_1\pi}{L_x}\right)^2 + \left(\frac{m_2\pi}{L_y}\right)^2\right], \tag{A.5}$$

where D is the membrane flexural rigidity given by

$$D = \frac{Eh^3}{12(1-\nu^2)}. \tag{A.6}$$

E, h, and ν are the membrane's Young's modulus, thickness, and Poisson's ratio, respectively [Leissa 1969]. The modeshapes of a membrane with bending stiffness are identical to those given by Equation (A.2).

A.2 Acoustic Modes and Natural Frequencies of a Rigid-walled Cavity

For a rectangular cavity of dimensions $L_x \times L_y \times L_z$ with perfectly rigid walls, the spatial component of the sound pressure satisfies the Helmholtz equation

$$\nabla^2\psi + k^2\psi = 0. \tag{A.7}$$

Using separation of variables and applying the rigid walled boundary condition where the normal component of the particle velocity is zero on the boundaries, it can be shown that the acoustic modeshapes follow the form

$$\psi_n(x,y,z) = \sqrt{e_1 e_2 e_3}\cos\left(\frac{n_1\pi x}{L_x}\right)\cos\left(\frac{n_2\pi y}{L_y}\right)\cos\left(\frac{n_3\pi z}{L_z}\right), \tag{A.8}$$

for acoustic mode $n = (n_1, n_2, n_3)$ where $e_i = 1$ for $n_i = 0$ and $e_i = 2$ if $n_i > 0$ for $i = 1, 2,$ or 3. The natural frequencies are then given by

$$\omega_n = c\sqrt{\left(\frac{n_1\pi}{L_x}\right)^2 + \left(\frac{n_2\pi}{L_y}\right)^2 + \left(\frac{n_3\pi}{L_z}\right)^2}. \tag{A.9}$$

A.3 Series Truncation

Expressing membrane vibration amplitudes and cavity pressures in a matrix-vector form using mode superposition requires that summations be truncated at a finite number of modes, M and N for structural and acoustic modes, respectively.

Figure A.1 shows the normal modes within an arbitrary frequency range, ω, for a membrane of dimensions $L_x \times L_y$. The modes included in the summation are those that fall within the specified frequency range, colored in red. For the normal modes of an acoustic cavity, one can imagine A.1 in three dimensions with the included modes being the combination of modal coordinates that fall within one octant of an enclosing sphere.

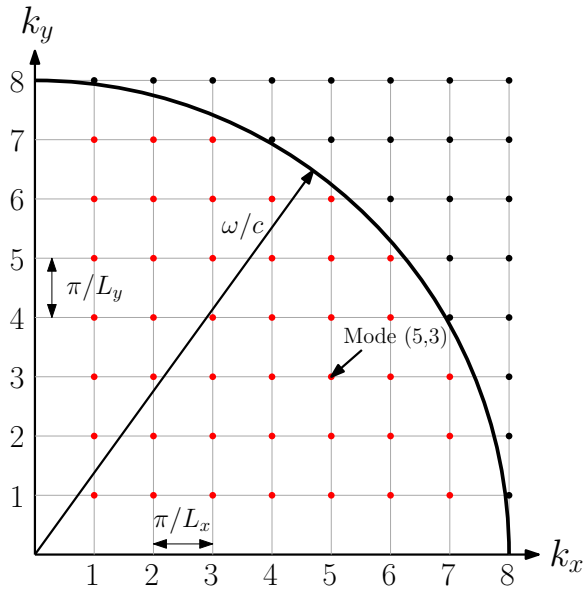

Figure A.1: Normal modes of an $L_x \times L_y$ membrane in k-space

Conventionally, the natural frequencies of the included modes must span a range that is two octaves higher than the highest frequency of interest [Bies & Hansen 2009]. However, in practice for a membrane carrying an attached mass the number of modes must be kept low to avoid internal resonances [Tian et al. 2014; Zhang et al. 2012]. In the research presented in this dissertation, the number of modes was held constant at $M = N = 9$, corresponding to a little under one octave above the highest frequency of interest. The modes and their corresponding

resonance frequencies for the baseline double panel configuration are shown in Figure A.2. Note that the cavity resonance frequencies are well outside of the frequency range of interest from 100 Hz to 4000 Hz with the exception of the fundamental mode.

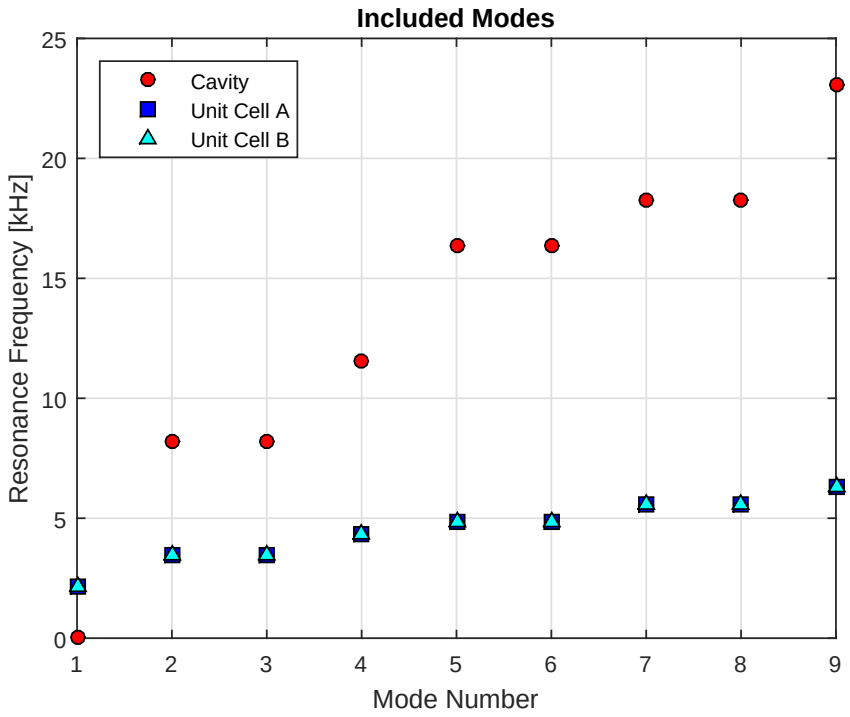

Figure A.2: Resonance frequencies of acoustic and structural modes included in finite summations

A.4 Modal Radiation Efficiences

The modal radiation efficiencies needed to compute the power transfer matrix (Equation (2.19)) are given by Equations (33), (38), and (43) in Snyder & Tanaka [1995], reproduced below with the notation used in this dissertation. The equations are separated into even and odd modes giving four separate equations. For a mode

$\alpha = (m_1, m_2)$

$$\sigma_\alpha = \frac{32k^2 L_x L_y}{m_1^2 m_2^2 \pi^5} \left\{ 1 - \frac{k^2 L_x L_y}{12} \left[\left(1 - \frac{8}{m_1^2 \pi^2} \right) \frac{L_x}{L_y} + \left(1 - \frac{8}{m_2^2 \pi^2} \right) \frac{L_y}{L_x} \right] \right\}, \quad \text{(A.10)}$$

for odd-odd modes;

$$\sigma_\alpha = \frac{8k^4 L_x^3 L_y}{3m_1^2 m_2^2 \pi^5} \left\{ 1 - \frac{k^2 L_x L_y}{20} \left[\left(1 - \frac{24}{m_1^2 \pi^2} \right) \frac{L_x}{L_y} + \left(1 - \frac{8}{m_2^2 \pi^2} \right) \frac{L_y}{L_x} \right] \right\}, \quad \text{(A.11)}$$

for even-odd modes;

$$\sigma_\alpha = \frac{8k^4 L_x L_y^3}{3m_1^2 m_2^2 \pi^5} \left\{ 1 - \frac{k^2 L_x L_y}{20} \left[\left(1 - \frac{8}{m_1^2 \pi^2} \right) \frac{L_x}{L_y} + \left(1 - \frac{24}{m_2^2 \pi^2} \right) \frac{L_y}{L_x} \right] \right\}, \quad \text{(A.12)}$$

for odd-even modes; and

$$\sigma_\alpha = \frac{2k^6 L_x^3 L_y^3}{15m_1^2 m_2^2 \pi^5} \left\{ 1 - \frac{k^2 L_x L_y}{14} \left[\left(1 - \frac{24}{m_1^2 \pi^2} \right) \frac{L_x}{L_y} + \left(1 - \frac{24}{m_2^2 \pi^2} \right) \frac{L_y}{L_x} \right] \right\}, \quad \text{(A.13)}$$

for odd-odd modes.

Figure A.3 shows the radiation efficiencies as a function of frequency.

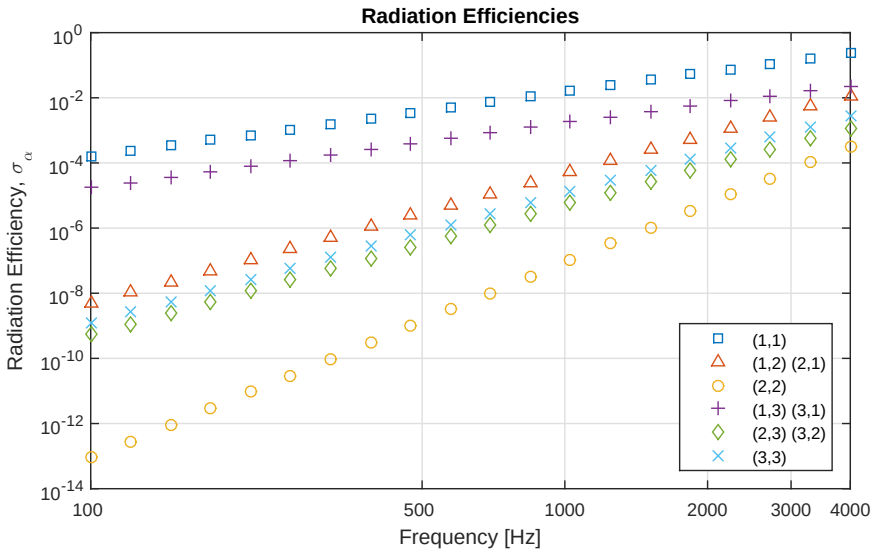

Figure A.3: Radiation efficiencies of included modes vs frequency

Appendix B

Tables

Table B.1: Baseline configuration parameter values

Parameter	Symbol	Value	Units
Unit cell width	L_x	21	mm
Unit cell height	L_y	21	mm
Membrane thickness	t_{mem}	0.0762	mm
Membrane density	ρ_{mem}	1200	kg/m^3
Membrane tension	T	5	MPa
Membrane elastic modulus	E	2.4	GPa
Membrane Poisson's ratio	ν	0.35	-
Mass density	ρ_{mass}	19000	kg/m^3
Mass elastic modulus	E_{mass}	170	GPa
Mass Poisson's ratio	ν_{mass}	0.3	-
Mass thickness	t_{mass}	4.5	mm
Mass width	l_x	3	mm
Mass height	l_y	3	mm
Mass x location	x_0	9	mm
Mass y location	y_0	9	mm

Table B.2: Alternate configuration parameter values

Parameter	Symbol	Value	Units
Unit cell width	L_x	21	mm
Unit cell height	L_y	21	mm
Membrane thickness	t_{mem}	0.0762	mm
Membrane density	ρ_{mem}	1000	kg/m^3
Membrane tension	T	6	MPa
Membrane elastic modulus	E	2.4	GPa
Membrane Poisson's ratio	ν	0.35	-
Mass density	ρ_{mass}	7000	kg/m^3
Mass elastic modulus	E_{mass}	390	GPa
Mass Poisson's ratio	ν_{mass}	0.31	-
Mass thickness	t_{mass}	6	mm
Mass width	l_x	3	mm
Mass height	l_y	3	mm
Mass x location	x_0	6	mm
Mass y location	y_0	9	mm

Table B.3: Design variable ranges

Parameter	Symbol	Units	Minimum	Maximum
Unit cell width	L_x	mm	15	35
Unit cell height	L_y	mm	15	35
Membrane thickness	t_{mem}	mm	0.0125	0.1506
Membrane density	ρ_{mem}	kg/m^3	900	2500
Membrane tension	T	N/m	50	500
Membrane elastic modulus	E	GPa	0.0008	5
Membrane Poisson's ratio	ν	-	0.3	0.5
Mass density	ρ_{mass}	kg/m^3	1000	20000
Mass thickness	t_{mass}	mm	1.5	6
Mass width ratio	$l_{x,r}$	-	0.01	0.25
Mass height ratio	$l_{y,r}$	-	0.01	0.25
Mass x location ratio	$x_{0,r}$	-	0.0625	0.5
Mass y location ratio	$y_{0,r}$	-	0.0625	0.5

Table B.4: Selected membrane material properties

Number	Material	Density $[kg/m^3]$	Young's Modulus [GPa]	Poisson's Ratio [-]
0	Polypropylene	900	1.3	0.45
1	Natural Rubber	980	0.0008	0.48
2	Neoprene	1100	0.01	0.49
3	Nylon	1200	2.4	0.35
4	Polyester	1310	2.3	0.40
5	PVC	1400	2.8	0.40
6	PVDF	1760	1.5	0.35
7	PTFE	2200	0.5	0.46

Table B.5: Selected mass material properties

Number	Material	Density $[kg/m^3]$	Young's Modulus [GPa]	Poisson's Ratio [-]
0	Magnesium	1740	44.7	0.29
1	Aluminum	2700	70	0.35
2	Titanium	4500	116	0.32
3	Neodymium	7000	390	0.31
4	Brass	8500	95	0.35
5	Lead	11,400	13.8	0.44
6	Tungsten	19,300	360	0.34
7	Platinum	21,400	168	0.27

Table B.6: Available mass sizes

Number	l_x [mm]	l_y [mm]	t_{mass} [mm]
0	3	3	1.5
1	3	6	1.5
2	6	3	1.5
3	6	6	1.5
4	3	3	3
5	3	6	3
6	6	3	3
7	6	6	3
8	3	3	4.5
9	3	6	4.5
10	6	3	4.5
11	6	6	4.5
12	3	3	6
13	3	6	6
14	6	3	6
15	6	6	6

Table B.7: Thicknesses available for selected membrane materials

Material Number	Material	Density $[kg/m^3]$	Young's Modulus [GPa]	Poisson's ratio [-]	Thickness [mm]
0	Polypropylene	900	1.3	0.45	0.0127
1					0.0254
2					0.0508
3					0.0762
4	Natural Rubber	980	0.0008	0.48	0.0254
5					0.0508
6					0.0762
7					0.1500
8	Neoprene	1100	0.01	0.49	0.0762
9					0.1270
10					0.1506
11	Nylon	1200	2.4	0.35	0.0254
12					0.0508
13					0.0762
14					0.1506
15	Polyester	1310	2.3	0.4	0.0127
16					0.0191
17					0.0254
18					0.0381
19					0.0508
20					0.0762
21					0.1506
22	PVC	1400	2.8	0.4	0.0191
23					0.0254
24					0.0508
25					0.1506
26	PVDF	1760	1.5	0.35	0.0762
27					0.1506
28	PTFE	2200	0.5	0.46	0.0254
29					0.0508
30					0.0762
31					0.1506

Table B.8: Finite element model details

Unit Cell Shape	Air Domain	Model	Total Number of Elements	Degrees of Freedom	Run Time (df = 10 Hz)
Square	Waveguide	Solid	69,178	211,922	17 hr 5 min
Square	Baffle	Shell	68,939	128,490	3 hr 46 min
2x1 Array Squares	Baffle	Shell	100,331	203,049	7 hr 21 min
2x2 Array Squares	Baffle	Shell	159,240	344,513	13 hr 42 min
Double Square	Waveguide	Shell	81,558	166,407	4 hr 57 min
Square Simple Mass	Waveguide	Solid	68,106	207,590	15 hr 44 min
Square	Waveguide	Shell	49,506	96,093	2 hr 28 min
Circle	Waveguide	Shell	59,776	122,373	3 hr 49 min
Circle Axi-symmetric	Waveguide	Solid	1051	3844	1 min 39 sec
Hexagon	Waveguide	Shell	20,350	70,696	2 hr 7 min
Triangle	Waveguide	Shell	27,195	62,628	1 hr 37 min

Appendix C

Genetic Algorithm Optimal Results Tables

Table C.1: Optimal parameter values for maximum broadband TL using a continuous GA

Parameter	Symbol	Value	Units
Unit cell width	L_x	15.16	mm
Unit cell height	L_y	15.00	mm
Membrane thickness	t_{mem}	0.1495	mm
Membrane density	ρ_{mem}	1127	kg/m^3
Membrane tension	T	393.7	N/m
Membrane elastic modulus	E	4.84	GPa
Membrane Poisson's ratio	ν	0.45	-
Mass density	ρ_{mass}	18055	kg/m^3
Mass thickness	t_{mass}	3.66	mm
Mass width	l_x	3.73	mm
Mass height	l_y	3.60	mm
Mass x location	x_0	5.18	mm
Mass y location	y_0	6.41	mm

Table C.2: Optimal parameter values for maximum broadband TL above the mass law using a continuous GA

Parameter	Symbol	Value	Units
Unit cell width	L_x	15.63	mm
Unit cell height	L_y	16.10	mm
Membrane thickness	t_{mem}	0.0136	mm
Membrane density	ρ_{mem}	1064	kg/m^3
Membrane tension	T	500.0	N/m
Membrane elastic modulus	E	1.14	GPa
Membrane Poisson's ratio	ν	0.39	-
Mass density	ρ_{mass}	2945	kg/m^3
Mass thickness	t_{mass}	2.21	mm
Mass width	l_x	1.67	mm
Mass height	l_y	1.03	mm
Mass x location	x_0	7.81	mm
Mass y location	y_0	7.16	mm

Table C.3: Optimal parameter values for maximum broadband TL using a discrete GA

Parameter	Symbol	Value	Units
Unit cell width	L_x	15.31	mm
Unit cell height	L_y	15.00	mm
Membrane thickness	t_{mem}	0.1506	mm
Membrane density	ρ_{mem}	1400	kg/m^3
Membrane tension	T	491.7	N/m
Membrane elastic modulus	E	2.80	GPa
Membrane Poisson's ratio	ν	0.40	-
Mass density	ρ_{mass}	21400	kg/m^3
Mass thickness	t_{mass}	6.00	mm
Mass width	l_x	6.00	mm
Mass height	l_y	6.00	mm
Mass x location	x_0	5.71	mm
Mass y location	y_0	4.19	mm

Table C.4: Optimal parameter values for maximum TL in the 250 Hz octave band using a continuous GA

Parameter	Symbol	Value	Units
Unit cell width	L_x	19.09	mm
Unit cell height	L_y	20.35	mm
Membrane thickness	t_{mem}	0.1212	mm
Membrane density	ρ_{mem}	1013	kg/m^3
Membrane tension	T	191.7	N/m
Membrane elastic modulus	E	2.80	GPa
Membrane Poisson's ratio	ν	0.35	-
Mass density	ρ_{mass}	17008	kg/m^3
Mass thickness	t_{mass}	5.86	mm
Mass width	l_x	4.70	mm
Mass height	l_y	4.93	mm
Mass x location	x_0	7.71	mm
Mass y location	y_0	8.14	mm

Table C.5: Optimal parameter values for maximum TL above the mass law in the 250 Hz octave band using a continuous GA

Parameter	Symbol	Value	Units
Unit cell width	L_x	15.16	mm
Unit cell height	L_y	15.63	mm
Membrane thickness	t_{mem}	0.1495	mm
Membrane density	ρ_{mem}	1089	kg/m^3
Membrane tension	T	500.0	N/m
Membrane elastic modulus	E	4.88	GPa
Membrane Poisson's ratio	ν	0.41	-
Mass density	ρ_{mass}	5339	kg/m^3
Mass thickness	t_{mass}	1.68	mm
Mass width	l_x	0.31	mm
Mass height	l_y	0.48	mm
Mass x location	x_0	1.26	mm
Mass y location	y_0	1.73	mm

Table C.6: Optimal parameter values for maximum TL in the 250 Hz octave band using a discrete GA

Parameter	Symbol	Value	Units
Unit cell width	L_x	15.16	mm
Unit cell height	L_y	15.47	mm
Membrane thickness	t_{mem}	0.0762	mm
Membrane density	ρ_{mem}	1310	kg/m^3
Membrane tension	T	406.3	N/m
Membrane elastic modulus	E	2.30	GPa
Membrane Poisson's ratio	ν	0.40	-
Mass density	ρ_{mass}	19300	kg/m^3
Mass thickness	t_{mass}	6.00	mm
Mass width	l_x	6.00	mm
Mass height	l_y	6.00	mm
Mass x location	x_0	3.82	mm
Mass y location	y_0	4.38	mm

Table C.7: Optimal parameter values for maximum TL at 613 Hz using a continuous GA

Parameter	Symbol	Value	Units
Unit cell width	L_x	16.89	mm
Unit cell height	L_y	15.79	mm
Membrane thickness	t_{mem}	0.1386	mm
Membrane density	ρ_{mem}	1618	kg/m^3
Membrane tension	T	280.3	N/m
Membrane elastic modulus	E	2.09	GPa
Membrane Poisson's ratio	ν	0.36	-
Mass density	ρ_{mass}	10126	kg/m^3
Mass thickness	t_{mass}	5.29	mm
Mass width	l_x	3.43	mm
Mass height	l_y	3.64	mm
Mass x location	x_0	6.52	mm
Mass y location	y_0	6.10	mm

Table C.8: Optimal parameter values for maximum TL above the mass law at 613 Hz using a continuous GA

Parameter	Symbol	Value	Units
Unit cell width	L_x	28.23	mm
Unit cell height	L_y	16.89	mm
Membrane thickness	t_{mem}	0.1386	mm
Membrane density	ρ_{mem}	988	kg/m^3
Membrane tension	T	354.7	N/m
Membrane elastic modulus	E	4.96	GPa
Membrane Poisson's ratio	ν	0.42	-
Mass density	ρ_{mass}	11173	kg/m^3
Mass thickness	t_{mass}	5.04	mm
Mass width	l_x	3.46	mm
Mass height	l_y	3.39	mm
Mass x location	x_0	11.78	mm
Mass y location	y_0	4.78	mm

Table C.9: Optimal parameter values for maximum TL at 613 Hz using a discrete GA

Parameter	Symbol	Value	Units
Unit cell width	L_x	16.26	mm
Unit cell height	L_y	18.15	mm
Membrane thickness	t_{mem}	0.1506	mm
Membrane density	ρ_{mem}	1310	kg/m^3
Membrane tension	T	260.2	N/m
Membrane elastic modulus	E	2.30	GPa
Membrane Poisson's ratio	ν	0.40	-
Mass density	ρ_{mass}	11400	kg/m^3
Mass thickness	t_{mass}	3.00	mm
Mass width	l_x	6.00	mm
Mass height	l_y	6.00	mm
Mass x location	x_0	4.77	mm
Mass y location	y_0	5.57	mm

Table C.10: Optimal parameter values for maximum TL for multiple weighted components using a continuous GA

Parameter	Symbol	Value	Units
Unit cell width	L_x	19.72	mm
Unit cell height	L_y	15.63	mm
Membrane thickness	t_{mem}	0.1408	mm
Membrane density	ρ_{mem}	1051	kg/m^3
Membrane tension	T	354.7	N/m
Membrane elastic modulus	E	2.13	GPa
Membrane Poisson's ratio	ν	0.41	-
Mass density	ρ_{mass}	19701	kg/m^3
Mass thickness	t_{mass}	5.65	mm
Mass width	l_x	4.43	mm
Mass height	l_y	3.82	mm
Mass x location	x_0	8.98	mm
Mass y location	y_0	5.07	mm

Table C.11: Optimal parameter values for maximum TL above the mass law for multiple weighted components using a continuous GA

Parameter	Symbol	Value	Units
Unit cell width	L_x	15.00	mm
Unit cell height	L_y	15.00	mm
Membrane thickness	t_{mem}	0.1495	mm
Membrane density	ρ_{mem}	925	kg/m^3
Membrane tension	T	485.8	N/m
Membrane elastic modulus	E	5.00	GPa
Membrane Poisson's ratio	ν	0.49	-
Mass density	ρ_{mass}	1598	kg/m^3
Mass thickness	t_{mass}	2.28	mm
Mass width	l_x	0.28	mm
Mass height	l_y	0.78	mm
Mass x location	x_0	5.38	mm
Mass y location	y_0	2.59	mm

Table C.12: Optimal parameter values for maximum TL for multiple weighted components using a discrete GA

Parameter	Symbol	Value	Units
Unit cell width	L_x	17.36	mm
Unit cell height	L_y	15.94	mm
Membrane thickness	t_{mem}	0.1506	mm
Membrane density	ρ_{mem}	1200	kg/m^3
Membrane tension	T	480.7	N/m
Membrane elastic modulus	E	2.40	GPa
Membrane Poisson's ratio	ν	0.35	-
Mass density	ρ_{mass}	21400	kg/m^3
Mass thickness	t_{mass}	6.00	mm
Mass width	l_x	6.00	mm
Mass height	l_y	6.00	mm
Mass x location	x_0	5.87	mm
Mass y location	y_0	5.56	mm

Appendix D

Figures

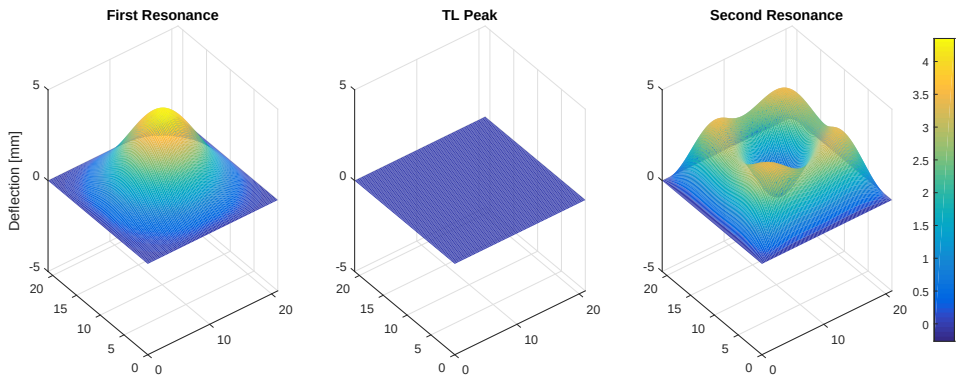

Figure D.1: Displacement profiles for first resonance, TL peak, and second resonance frequencies

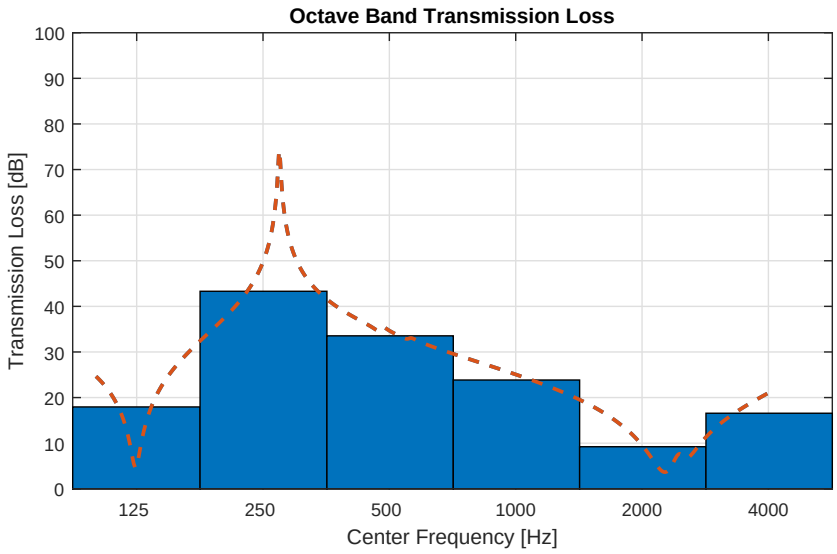

Figure D.2: TL of unit cell optimized for maximum TL in the 250 Hz octave band using a continuous GA

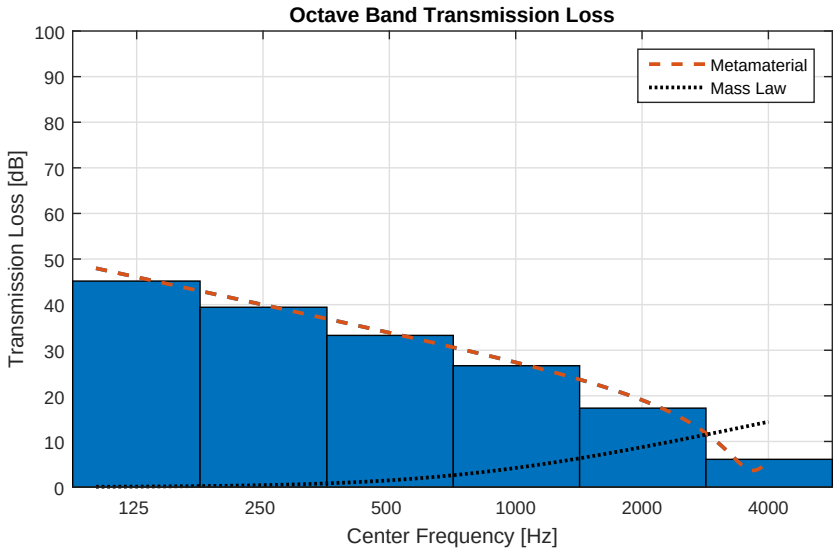

Figure D.3: TL of unit cell optimized for maximum TL above the mass law in the 250 Hz octave band

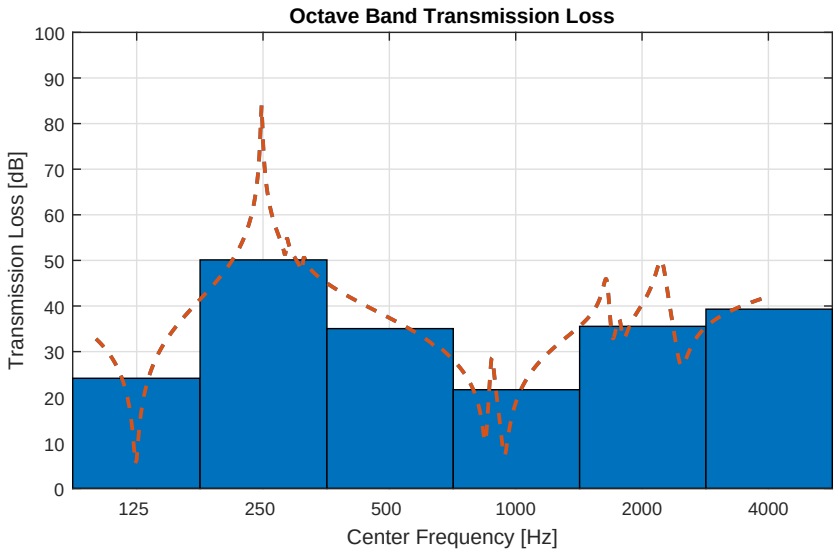

Figure D.4: TL of unit cell optimized for maximum TL in the 250 Hz octave band using a discrete GA

Appendix E

Application of Boundary Conditions

For the simply supported case, in which the displacement of the membrane at the boundaries is fixed at zero and the slope is unconstrained, the integrals derived in Chapter 2 can easily be solved in a closed form. The closed-form solutions are particularly amenable to hard-coding which greatly increases computational efficiency. For that reason, the closed-form solutions to the integrals that form the structural mobility matrix of the unit cell of a membrane-type acoustic metamaterial are presented here.

For a simply supported membrane the area-normalized mode function is written

$$\phi_m(x,y) = 2\sin\left(\frac{m_1\pi x}{L_x}\right)\sin\left(\frac{m_2\pi y}{L_y}\right). \tag{E.1}$$

The terms defined in Chapter 2, Equations 2.6 - 2.10 and 2.26, can be solved explicitly as follows

$$M_m = \rho_s L_x L_y, \tag{E.2}$$

$$Q_{mn} = \frac{-L_x L_y \rho_{mass}}{\pi^2 (m_1^2 - n_1^2)(m_2^2 - n_2^2)} \left\{ \left[(m_1 + n_1) \sin\left(\frac{\pi(m_1 - n_1)x_0}{L_x}\right) \right.\right.$$
$$-(m_1 - n_1) \sin\left(\frac{\pi(m_1 + n_1)x_0}{L_x}\right) - (m_1 + n_1) \sin\left(\frac{\pi(m_1 - n_1)(x_0 + l_x)}{L_x}\right)$$
$$\left.\left. +(m_1 - n_1) \sin\left(\frac{\pi(m_1 + n_1)(x_0 + l_x)}{L_x}\right) \right] \left[(m_2 + n_2) \sin\left(\frac{\pi(m_2 - n_2)y_0}{L_y}\right) \right.\right. \quad \text{(E.3)}$$
$$-(m_2 - n_2) \sin\left(\frac{\pi(m_2 + n_2)y_0}{L_y}\right) - (m_2 + n_2) \sin\left(\frac{\pi(m_2 - n_2)(y_0 + l_y)}{L_y}\right)$$
$$\left.\left. +(m_2 - n_2) \sin\left(\frac{\pi(m_2 + n_2)(y_0 + l_y)}{L_y}\right) \right] \right\},$$

for $m \neq n$;

$$Q_{mm} = \rho_{mass} \left(l_x - \frac{L_x}{2m_1\pi} \left(\sin\left(\frac{2\pi m_1(x_0 + l_x)}{L_x}\right) - \sin\left(\frac{2\pi m_1 x_0}{L_x}\right) \right) \right)$$
$$\left(l_y - \frac{L_y}{2m_2\pi} \left(\sin\left(\frac{2\pi m_2(y_0 + l_y)}{L_y}\right) - \sin\left(\frac{2\pi m_2 y_0}{L_y}\right) \right) \right), \quad \text{(E.4)}$$

for $m = n$;

$$K_m = \frac{T\pi^2}{L_x L_y} \left(m_1^2 L_x^2 + m_2^2 L_y^2 \right), \quad \text{(E.5)}$$

where m_1 and m_2 are modal indices of the m^{th} structural mode,

$$H_m = \frac{2L_x L_y}{m_1 m_2 \pi^2} \left((-1)^{m_1} - 1 \right) \left((-1)^{m_2} - 1 \right), \quad \text{(E.6)}$$

$$D_m = 2\rho_0 c_0 L_x L_y, \quad \text{(E.7)}$$

and

$$E_m = \frac{D\pi^4}{L_x^3 L_y^3}\left(m_1^2 L_y^2 + m_2^2 L_x^2\right)^2. \tag{E.8}$$

The coupling coefficient for a double layer structure given by Equation (2.63) can be evaluated explicitly for structural mode $m = (m_1, m_2)$ and acoustic cavity mode $n = (n_1, n_2, n_3)$ as

$$C_{m,n}^A = \frac{2\sqrt{e_1 e_2 e_3} L_x L_y m_1 m_2 \left(1-(-1)^{m_1+n_1}\right)\left(1-(-1)^{m_2+n_2}\right)}{\pi^2\left(m_1^2-n_1^2\right)\left(m_2^2-n_2^2\right)} \tag{E.9}$$

for unit cell A located at $z_i = 0$, and

$$C_{m,n}^B = \frac{2\sqrt{e_1 e_2 e_3} L_x L_y m_1 m_2 (-1)^{n_3}\left(1-(-1)^{m_1+n_1}\right)\left(1-(-1)^{m_2+n_2}\right)}{\pi^2\left(m_1^2-n_1^2\right)\left(m_2^2-n_2^2\right)} \tag{E.10}$$

for unit cell B located at $z_i = L_z$. The term $\sqrt{e_1 e_2 e_3}$ in the above equations is the acoustic modeshape normalization factor where $e_i = 1$ for $n_i = 0$ and $e_i = 2$ if $n_i > 0$. If $m_1 = n_1$ and/or $m_2 = n_2$, the value of the coupling coefficient is zero.

The generalized modal force due to an incident plane wave from an arbitrary angle is defined as

$$\tilde{g}_{p,m} = 2\int_0^{L_x}\int_0^{L_y} \tilde{p}_{inc}(x,y)\phi_m \mathrm{d}y\mathrm{d}x, \tag{E.11}$$

where the pressure distribution takes the form $\tilde{p}_{inc}(x,y) = \tilde{p}_{inc} e^{-jk_x x - jk_y y}$. The wavenumbers in each direction are $k_x = k\sin(\alpha)\cos(\beta)$ and $k_y = k\sin(\alpha)\sin(\beta)$, where α and β are the angles of incidence with respect to the normal vector of the unit cell.

Applying the simply supported boundary condition to Equation (E.11) results in

$$\tilde{g}_{p,m} = \frac{4\tilde{p}_{inc} m_1 m_2 \pi^2 L_x L_y \left((-1)^{m_1} e^{-jk_x L_x} - 1\right) \left((-1)^{m_2} e^{-jk_y L_y} - 1\right)}{\left(k_x^2 L_x^2 - m_1^2 \pi^2\right) \left(k_y^2 L_y^2 - m_2^2 \pi^2\right)} \tag{E.12}$$

For normally-incident plane waves, $k_x = k_y = 0$, which gives $\tilde{g}_{p,m} = 2\tilde{p}_{inc} H_m$.